

The nature of condensed single molecules

- local electronic and mechanical characteristics -

INAUGURALDISSERTATION

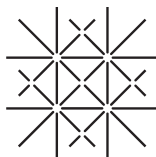
zur

Erlangung der Würde eines Doktors der Philosophie
vorgelegt der
Philosophisch-Naturwissenschaftlichen Fakultät
der Universität Basel

von

Dipl. Phys. Sweetlana Deva Fremy

geboren in Wittmund, Deutschland



UNI
BASEL

Basel, Januar, 2014

Originaldokument gespeichert auf dem Dokumentenserver der Universität Basel
edoc.unibas.ch



Dieses Werk ist unter dem Vertrag 'Creative Commons Namensnennung-Keine kommerzielle Nutzung-Keine Bearbeitung 3.0 Schweiz' (CC BY-NC-ND 3.0 CH) lizenziert. Die vollständige Lizenz kann unter creativecommons.org/licenses/by-nc-nd/3.0/ch/ eingesehen werden.

Genehmigt von der

Philosophisch-Naturwissenschaftlichen Fakultät

auf Antrag von:

Prof. Dr. Ernst Meyer,

Prof. Dr. Martino Poggio

Basel, den 15. Oktober 2013

Prof. Dr. Jörg Schibler
Dekan



Namensnennung-Keine kommerzielle Nutzung-Keine Bearbeitung 3.0 Schweiz
(CC BY-NC-ND 3.0 CH)

Sie dürfen: Teilen — den Inhalt kopieren, verbreiten und zugänglich machen

Unter den folgenden Bedingungen:



Namensnennung — Sie müssen den Namen des Autors/Rechteinhabers in der von ihm festgelegten Weise nennen.



Keine kommerzielle Nutzung — Sie dürfen diesen Inhalt nicht für kommerzielle Zwecke nutzen.



Keine Bearbeitung erlaubt — Sie dürfen diesen Inhalt nicht bearbeiten, abwandeln oder in anderer Weise verändern.

Wobei gilt:

Verzichtserklärung — Jede der vorgenannten Bedingungen kann **aufgehoben** werden, sofern Sie die ausdrückliche Einwilligung des Rechteinhabers dazu erhalten.

Public Domain (gemeinfreie oder nicht-schützbarer Inhalte) — Soweit das Werk, der Inhalt oder irgendein Teil davon zur Public Domain der jeweiligen Rechtsordnung gehört, wird dieser Status von der Lizenz in keiner Weise berührt.

Sonstige Rechte — Die Lizenz hat keinerlei Einfluss auf die folgenden Rechte:

- Die Rechte, die jedermann wegen der Schranken des Urheberrechts oder aufgrund gesetzlicher Erlaubnisse zustehen (in einigen Ländern als grundsätzliche Doktrin des **fair use** bekannt);
- Die **Persönlichkeitsrechte** des Urhebers;
- Rechte anderer Personen, entweder am Lizenzgegenstand selber oder bezüglich seiner Verwendung, zum Beispiel für **Werbung** oder Privatsphärenschutz.

Hinweis — Bei jeder Nutzung oder Verbreitung müssen Sie anderen **alle** Lizenzbedingungen mitteilen, die für diesen Inhalt gelten. Am einfachsten ist es, an entsprechender Stelle einen Link auf diese Seite einzubinden.

„Willst du dich am Ganzen erquicken, so musst du das Ganze
im Kleinsten erblicken.“

JOHANN WOLFGANG VON GÖTTE

Abstract

In order to advance the performance of molecule based electronic devices a detailed and fundamental knowledge about the underlying physical aspects is mandatory. It is well known that the performance of any organic electronic device is influenced by the physics at the interfaces between different molecules or molecule and substrate. Tracing down these phenomena towards the single molecular scale could highly improve the understanding and broaden the insight into the physics involving interfaces with organic compounds.

In this manner, the present thesis is concerned with the nature of condensed single molecules studied by means of tuning fork based scanning tunneling- and atomic force microscopy in ultra-high-vacuum and at low temperature. The appealing local character of scanning probe based investigation tools is very well suited for investigations at the sub-nanometer scale. Particularly, the various spectroscopic operation modes directly enable to extract present interaction forces, to visualize molecular frontier orbitals, or to study local work function - or electrostatic potential variations. In order to apply these techniques towards single molecules on a surface, in a first step different spectroscopy data acquisition modes were compared with respect to the various experimental challenges that need to be regarded during long term high data density measurements.

In a second step, the elasticity of a single molecule on a metal surface was analyzed via three dimensional force spectroscopy data. By observing a vertical elastic lifting process of certain functional side groups by the scanning tip, a controlled manipulation process based on the rotation of single molecules could be established. Similarly, the electronic properties of a single molecule on two different substrates were addressed by scanning tunneling- as well as three dimensional local Kelvin probe bias spectroscopy. By comparing the adsorption on a strongly interacting metal surface with that on an intervening epitaxial NaCl bilayer, due to which the molecule electronic structure is only weakly perturbed, the influences of charge transfer became directly visible. Supported by first principles calculations, it was shown, that even adsorption asymmetries concerning the second substrate layer below the molecule affect the distribution of charge.

Contents

Introduction	iii
I Investigative Tools	1
1 Tuning Fork Based Scanning Probe Microscopy	3
1.1 The Tunneling Current	5
1.1.1 Tunneling Hamilton Formalism	7
1.1.2 Description of the Tunneling Tip	8
1.2 Interaction Forces	10
1.2.1 Force Contributions	11
1.2.2 Dynamic Operation and Spatial Resolution	13
1.2.3 Origin of the Frequency Shift	15
1.2.4 Energy Dissipation in nc-AFM	16
1.3 Operation with a <i>qPlus</i> Tuning Fork Sensor	18
1.3.1 Topography and Feedback Operation	19
1.3.2 Spectroscopy	22
1.3.3 Manipulation	27
2 Multidimensional Spectroscopy Operation	31
2.1 Advantages of 3D Spectroscopy	31
2.2 Data Acquisition Methods	33
2.3 Experimental Challenges	34
2.4 Comparison of Grid- and Layer-Mode	36
2.4.1 Frequency Shift Maps	38
2.4.2 Interaction Force and Potential Energy	39
2.4.3 Performance of Grid- and Layer-Mode	42
2.5 Summary	44
3 Experimental	45
3.1 The UHV System	45
3.2 Characteristics of the Omicron <i>qPlus</i> Sensor	46
3.3 Substrate Preparation	48
3.4 Molecules	50
3.4.1 Utilized Molecules	50
3.4.2 Deposition	52
3.4.3 Sublimation Testing Unit	53
3.4.4 Chemical Stability of a DA Molecule	54

3.5	Summary	61
II	Single Molecule Investigations	63
4	Introduction into Molecules and Surfaces	65
4.1	Molecules in Gas Phase	65
4.2	Surfaces of Inorganic Substrates	69
4.3	Adsorption	73
4.4	Mechanical Properties	76
4.5	Interface Electronic Structure	77
4.5.1	Metal-Organic Interface	77
4.5.2	Thin Insulating Films on Metals	80
5	Mechanical Properties of Single Molecules	83
5.1	Adsorption Geometry	83
5.2	Elastic Deformation	84
5.3	Directed Rotations	88
5.4	Summary	91
6	Electronic Properties of Single Molecules	93
6.1	Sample Morphology	95
6.2	Adsorption Geometry	95
6.3	Electronic Structure	97
6.4	Local bias spectroscopy measurements	99
6.5	Switching the Adsorption Conformation	103
6.6	Summary	107
	Conclusion	109
	References	111
A	Outlook: Towards Optically Induced Charge Transfers	137
B	Dissipation with the old sensor	147
	Acknowledgments	149
	List of Figures	151
	List of Abbreviations and Variables	153
	List of Publications and Presentations	155
	Curriculum Vitae	159

Introduction

‘A computer wanted!’

This could have been a job offer from the 19th century, searching for a math specialist. However, the history of computers as we know them today even goes back to the ancient world. With its origin in the latin word ‘computare’, meaning to compute something, it refers to mechanical or electrical utilities (hardware) for arithmetic operations. Probably, one could regard the Abakus as the first ‘computer’, which goes back to the indo-chinese culture around 1000 BC. Ever since, innumerable other examples from specialized mechanical to fully automatized machines based on punched paper cards, were introduced.

The modern computer science was starting with the development of fully programmable devices. A pioneer concept for this development was given by the ‘turing machine’ introduced by A. Turing 1936. This hypothetical device is capable of formalizing algorithms and computation, and is still up to date to explain the functions of the central processing units in modern computers. The first real prototypes then go back to Conrad Zuse with his Z series. The Z3 presented in 1941 was the first working electromechanical computer with binary- and floating point arithmetic.

In the following decades, the exponentially increasing development of science and technology, and their mutual influence, led to innumerable breakthroughs in technology, and gradually all features seen in modern computers, were added. One of the milestones is given by the transistor effect, presented by W. B. Shockley, J. Bardeen and W. Brattain, who were rewarded with the Nobel Prize in 1956 for their striking invention. Transistors started to replace the amplifier tubes which have been the technological base of computers until then. Allowing the drastic reduction of size without losing operational power then finally quickened the development of personal computers for private usage starting in the 1950th. With the ongoing progress in microcontroller and integrated circuit development in the following decades, the computers’ hardware became smaller and smaller, as well as faster and faster. Nowadays equipped with displays, and many other interfaces, computers continuously developed into a mass product deeply incorporated into our present world.

While the basic concept remained since its early steps, the sizes, capacity

and computational power of computers mainly scale with the amount and sizes of the plugged transistors, which is according to ‘Moore’s law’ [1]. Today, we are almost at the limit of present technologies with transistor sizes down to the 100 nm regime [2]. The continuous size reductions are accompanied by several technological and fundamental challenges, and drastically increasing costs in the required equipment to build them [2]. The search of reasonable alternatives gave birth to modern nanotechnology and the attempts of bottom-up approaches for electronic devices. In this concern, the visionary talk of R. Feynman in 1960 named ‘There is plenty of room at the bottom!’ [3] is still inspiring many scientists around the world.

Molecules are the smallest fully controllable units by which bits of information can be carried, while maintaining a rich variety of functionalities, and thus the fast increasing interdisciplinary research field of molecular nanotechnology developed. The sub-field molecular electronics [4–6] is based on the ultimate goal to use single molecules in electronic devices within a bottom-up approach. While the first evidence about charge transport through organic materials by means of conductance measurements was presented by B. Mann and H. Kuhn in 1971 [7], the concept goes back to the theoretical visionary work from A. Aviram and M. Rattner, who suggested a single molecular rectifier already in 1974 [8]. However, as simple the idea sounds, as complicated it is to realize. In order to pass current through single molecular devices, to measure voltage drops, or to explore them for storage technology, they always need to be in contact with a conducting electrode, which causes one of the main challenges in the field [9, 10], associated with the central question: How does charge move through single molecules?

An experimental break through in the technological accessibility of single molecular units was finally given with the inventions of the scanning tunneling- (STM) [11] and atomic force microscope (AFM) [12] in the 1980ths. Allowing for ultimate spatial resolution in the sub-nanometer range [13–16] single molecules can now be studied with high accuracy and precision, concerning topographical and structural [17, 18], as well as functional properties, like molecular conductance [19, 20], molecular diffusion barriers [21], or vibronic excitation. Furthermore, numerous examples of molecules as functional devices like molecular switches [22, 23], or other molecular machines [24] have been presented.

The present thesis is concerned with mechanical and electronic properties of single molecules on surfaces by means of STM and AFM utilizing a tuning fork [25] sensor at low temperature and organizes as follows: Part 1 deals with investigative tools. Starting with a brief review about tuning fork based topographic and spectroscopic operation modes in Chap. 1, the first part of the thesis aims at methodological work on multidimensional spectroscopy methods, which is subject to Chap. 2. Ruling out possible measurement artifacts, two different data acquisition techniques are compared for all available spectroscopy modes. Finally, the equipment and sample preparation methods

will be presented in Chap. 3. A main focus lies on the handling of molecules, which can be accompanied by various experimental challenges.

Part two then is subject to on-surface investigations. First, several theoretical concepts in Chap. 4 will be summarized, while pointing out the mutual influence of molecules and surfaces with respect to the characteristic local adsorption geometry. Focusing on the well established and thoroughly investigated porphyrins and phthalocyanines [26], Chap. 5 will be subject to atomic scale elastic properties of single porphyrin molecules. A controllable directed rotational manipulation process could be established, which is supposed to be fully driven by the present interaction forces. Finally, in Chap 6 the influence of the adsorption interactions on the electronic properties of a single copper phthalocyanine will be investigated by comparing the adsorption on two different substrates, a strongly interacting metal surface (Cu(111)), and on an intervening thin insulating bilayer of NaCl. By looking at the local adsorption geometries and molecular resonances mapped by scanning tunneling spectroscopy it was confirmed, that the electron transfer on the metal strongly modifies the local density of states above the molecule, besides lowering its symmetry. Furthermore, Kelvin probe local bias spectroscopy measurements proved that the symmetry is even further decreased due to inequivalent adsorption sites in the subsurface layer of the Cu(111) substrate.

Part I

Investigative Tools

Chapter 1

Tuning Fork Based Scanning Probe Microscopy

The remarkable inventions of the scanning tunneling- (STM) [11] and atomic force microscope (AFM) [12] by Binnig, Rohrer, Quate and Gerber in 1982 and 1986 respectively, facilitated the ultimate entry into the tiny nanoworld. Since then, both techniques evolved into invaluable tools for surface science investigations [15,16]. They allow for atomic-scale topographic characterizations [13,14], as well as for the probing of various physical properties like the sample electronic structure [27,28], potential energy landscape [29,30], or local work function variations [31,32]. Finally, they also made the visionary idea of controlling matter on the atomic scale by means of manipulation become true [33,34]¹. Nowadays, applications range from inorganic surfaces to biological sample systems, and most probably nobody would have expected that for instance an AFM will even be sent to Mars in order to be part in revealing its geologic history and biological potential [37].

The common basis of scanning probe methods relies in the scanning principle, in which a physical probe (atomically sharp tip) is brought into the close proximity of a surface and mechanically moved across it by means of an incremental scan, driven by piezoelectric actuators, as shown in Fig. 1.1. This makes them essentially different from other microscopes as it necessitates to consider interactions within a near field approximation. Hence, the resolution is not limited by optical diffraction effects (Abbe's law) but scales with the probe's size which in turn is the reason for the availability of spatial resolution at the atomic scale.

The operation of an STM relies in the detection of a quantum mechanical tunneling current between a tip and conductive sample, used also for dis-

¹Both methods are also able to probe magnetic properties by means of spin-polarized STM (SP-STM) [35], magnetic force microscopy (MFM) [16] or magnetic exchange force microscopy (MexFM) [36]. However, these sub branches will be disregarded for the following discussion as no magnetic properties have been subject to this thesis.

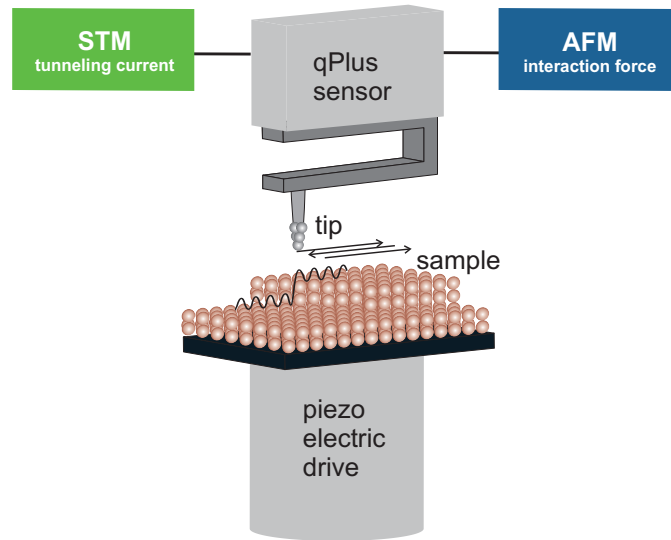


Figure 1.1: Scheme of a *qPlus* tuning fork sensor scanning across a sample surface. One of the two tuning fork prongs is fixed while the other one serves as the force sensor with a tip mounted at its free end. It can either be operated by STM, AFM or simultaneous STM/AFM modes by employing different feedback circuits as introduced in Sec. 1.3.1.

tance control. On the other hand, the key parameter in AFM is given by the tip-sample interaction force, or in dynamic operation modes by the force gradient. Thus, complementary information is available compared to STM, particularly also insulating surfaces can be accessed. All measurements presented in the framework of the thesis have been recorded with a quartz based tuning fork in the so called *qPlus* configuration suggested by Giessibl [see Sec. 1.3] [25,38]. A schematic drawing is shown in Fig. 1.1. With this sensor type, the simultaneous operation of scanning probe microscopes with STM and AFM became possible in a straightforward manner [39]. Characteristically, one of the two tuning fork prongs is fixed to a substrate, while the scanning tip is mounted on the other one, which then acts as force sensor and STM tip at the same time. In order to probe a surface various operation modes are available [see Secs. 1.3.1, 1.3.2, and 1.3.3]. However, before going into detail about these, the physical background of the quantum mechanical tunneling current and the tip-sample interaction forces will be briefly reviewed in the next two sections.

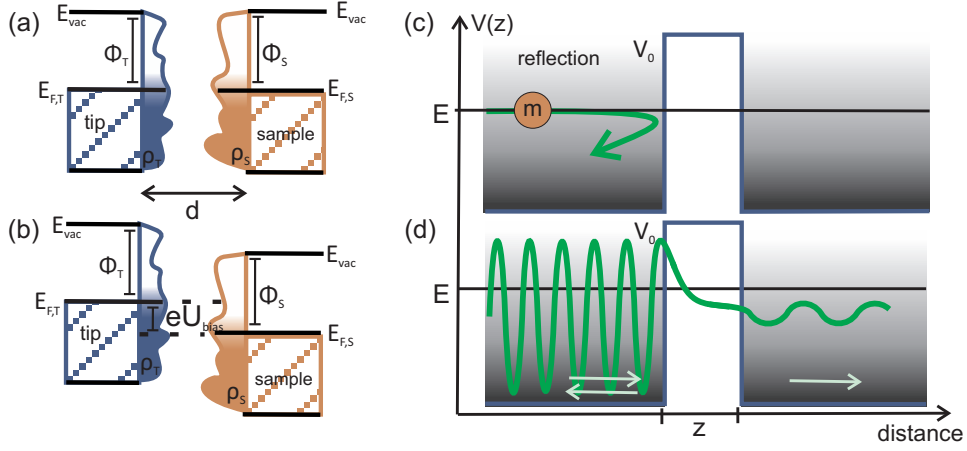


Figure 1.2: The tunneling current. **(a,b)** Schematic energy diagrams illustrating the flow direction of the tunneling current I_t between tip and sample in case of aligned Fermi levels (a), and a positive applied bias voltage U_{bias} . E_{vac} defines the vacuum level, Φ_T and Φ_S the work functions, ρ_T and ρ_S the densities of states, and $E_{F,T}$ and $E_{F,S}$ the Fermi energies of tip (T) and sample (S). **(c, d)** The one dimensional tunneling effect. From the classical point of view (c) a particle with energy $E < V_0$ will be totally reflected by the barrier. In contrast, in quantum mechanics (d) particles are described by wave functions Ψ with a certain finite probability of tunneling through the barrier.

1.1 The Tunneling Current

When an atomically sharp metallic tip and a sample are brought into close proximity to each other ($\approx 10 \text{ \AA}$), their wave functions Ψ_T and Ψ_S begin to overlap. As a result, the quantum mechanical tunneling effect leads to a certain probability for electrons to overcome the tip-sample-barrier, as it is shown in Fig. 1.2 (a). By applying a bias voltage U_{bias} of typically 0 V to 3 V, the respective Fermi levels $E_{F,T}$ and $E_{F,S}$ shift against each other [see Fig. 1.2 (b)], defining a preferred tunneling direction which depends on the polarity. Hence, a net tunneling current I_t starts to flow which exponentially depends on the tip-sample-distance z . If the tip bias with respect to the sample is positive electrons tunnel from occupied tip states into unoccupied sample states. On the other hand, for negative biases they tunnel from occupied sample states into unoccupied tip states. At this point, it should be mentioned, that in the experimental setup used the bias voltage is always applied to the tip.

The most elementary theory of the tunneling current assumes the tip-sample separation as one dimensional piece-wise constant barrier of the height V_0 [41], like depicted in Fig. 1.2 (c) and (d). From the classical point of view particles of the mass m and energy E can only traverse the barrier, if $E > V_0$. Otherwise, they will be reflected as the particle shown in (c). However, in

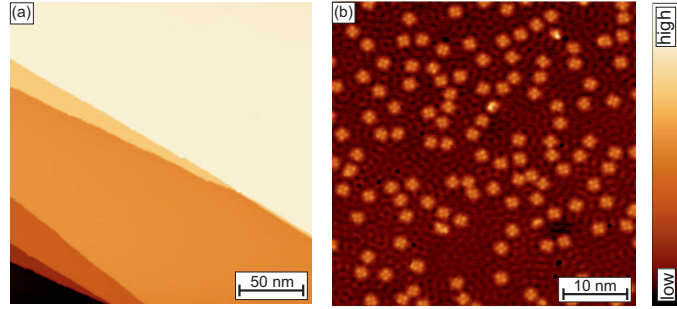


Figure 1.3: STM images dominated by (a) the sample topography, and (b) electronic effects. In (a) the step devolution on the Cu(111) surface is shown. In contrast, the wave patterns visible in (b) can be attributed to the Shockley type surface state on Cu(111) [see Sec. 3.3]. The protrusions refer to certain orbitals of single Cu-phtalocyanine [40] molecules [Chap. 6]. **Parameters:** (a): $U_{\text{bias}} = -500$ mV, $I_t = 35$ pA, (b): $U_{\text{bias}} = -20$ mV, $I_t = 30$ pA.

quantum mechanics, which is based on the wave particle dualism, they are described by their wave functions Ψ which have to satisfy the Schrödinger equation. Experimentally, this leads to a finite probability of finding particles with $E < V_0$ beyond the barrier, which have **tunneled** through it [Fig. 1.2 (d)].

The expression of the tunneling current relies on the transmission coefficient T which determines the tunneling probability. It is defined by the ratio of the transmitted j_t and incident j_i current densities via [41]:

$$T = \frac{j_t}{j_i} = \frac{1}{1 + (k^2 + \kappa^2)^2 / (2k\kappa \sinh(\kappa z))^2} \stackrel{\kappa z \gg 1}{\approx} \frac{16k^2 \kappa^2}{(k^2 + \kappa^2)^2} e^{-2\kappa z}, \quad (1.1)$$

where $k^2 = 2m/\hbar^2 E$, and $\kappa = \sqrt{2m(V_0 - E)}/\hbar$. The approximation of $\kappa z \gg 1$ refers to a strongly attenuating barrier. The one dimensional approach clearly illustrates the tunneling current's sensitivity on the barrier width (independent of its exact shape), and its strongly exponential dependence on the tip-sample separation. This in turn ensures that mainly the front most tip atom is involved into the imaging process of STM, being reason for the high obtainable resolution.

Eq. 1.1 serves for a description of topographic effects only, like for instance in Fig. 1.3 (a). On the other hand, if the image is as well influenced by electronic effects, like the wave patterns in Fig. 1.3 (b) [see also Sec. 3.3], a three-dimensional treatment is needed for an explanation. An example is given by the approach presented by Bardeen in 1961 [42], which is subject to the next section.

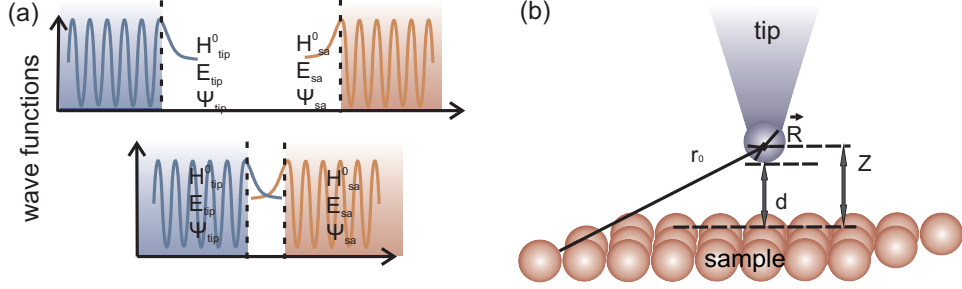


Figure 1.4: (a) Scheme of the tunneling process in accordance to Bardeen. For large separations, tip and sample can be described by their free potentials. Only for small z a weak coupling occurs due to the perturbation of the tip. (b) Tip model of the Tersoff-Hamann model.

1.1.1 Tunneling Hamilton Formalism

By employing first order time dependent perturbation theory (Fermi's Golden Rule) in accordance to Bardeen [42], the tunneling current can be expressed within a 3D geometry. In contrast to his original theory in which he regarded the tip-sample system as two unperturbed only weak interacting sub-systems, the following derivation is based on a scriptum of Blügel [43], and accounts for a perturbation already in the first place. The Schrödinger equations of the initially separated tip- and sample systems [see Fig. 1.4 (a)] are given by

$$\left(-\frac{\hbar^2}{2m}\Delta + V_T\right)\Psi_\nu^T = E_\nu^S\Psi_\nu^T, \quad (1.2)$$

$$\left(-\frac{\hbar^2}{2m}\Delta + V_S\right)\Psi_\mu^S = E_\mu^S\Psi_\mu^S, \quad (1.3)$$

where V_S and V_T are the potentials and Ψ_μ^S and Ψ_ν^T the initially unperturbed wave functions of tip and sample, respectively. Upon the approach of tip and sample with an applied bias voltage, the potentials start to modify due to the perturbation of the tip, as shown in Fig. 1.4 (b). By applying a time dependence $V_T(t) = e^{\frac{\eta t}{\hbar}}V_T$ and setting $\eta > 0$ for the tip potential one obtains:

$$i\hbar\frac{\partial}{\partial t}\Psi_\mu = \left(-\frac{\hbar^2}{2m}\Delta + V_S + e^{\frac{\eta t}{\hbar}}V_T\right)\Psi_\mu. \quad (1.4)$$

Initially ($t \rightarrow -\infty$), all electrons occupy sample eigenstates $\Psi_\mu^S(\vec{r})$ while later the tip perturbation leads to the additional occupation of tip states $\Psi_\nu^T(\vec{r})$. By inserting the Ansatz:

$$\Psi(\vec{r}, t) = a_\mu(t)\Psi_\mu^S(\vec{r})e^{-\frac{i}{\hbar}E_\mu^S t} + \sum_\nu c_\nu(t)\Psi_\nu^T(\vec{r})e^{-\frac{i}{\hbar}E_\nu^T t}, \quad (1.5)$$

into Eq. 1.4 and iteratively solving the obtained system of equations in the time dependent perturbation approach with first order approximation yields in an expression for the transition rate of electrons which passed from Ψ_μ^S into Ψ_ν^T :

$$\omega_{\mu\nu}(t) = \frac{d}{dt} |c_\nu(t)|^2 = \frac{2\eta}{(E_\mu^S - E_\nu^T)^2 + \eta^2} e^{\frac{2\eta t}{\hbar}} \frac{1}{\hbar} |\langle \Psi_\nu^T | V_T | \Psi_\mu^S \rangle|^2. \quad (1.6)$$

Employing the delta distribution in the limit of $\eta \rightarrow 0$ finally leads to:

$$\omega_{\mu\nu} = \frac{2\pi}{\hbar} \delta(E_\nu^T - E_\mu^S) |M_{\mu\nu}|^2, \quad \text{with} \quad (1.7)$$

$$M_{\mu\nu} = \langle \Psi_\nu^T | V_T | \Psi_\mu^S \rangle. \quad (1.8)$$

The delta function $\delta(E_\nu^T - E_\mu^S)$ ensures energy conservation (only elastic tunneling), and the tunneling matrix element $M_{\mu\nu}$ is Fermi's Golden Rule for the perturbation V_T . It can be rewritten as a surface integral:

$$M_{\mu\nu} = -\frac{\hbar^2}{2m} \int_A d\vec{S} \cdot \left(\Psi_\nu^{T*} \vec{\nabla} \Psi_\mu^S - \Psi_\mu^S \vec{\nabla} \Psi_\nu^{T*} \right), \quad (1.9)$$

which only depends on the wave functions of tip and sample at any chosen interface A separating tip and sample within the vacuum barrier region. Finally, the tunneling current as it is proportional to $e\omega_{\mu\nu}$ can be derived by regarding all possible transitions from occupied sample states to unoccupied tip states and vice versa, resulting in:

$$I = \frac{4\pi e^2}{\hbar} U_{bias} \rho^T(E_F^T) \rho^S(E_F^S) |M|^2. \quad (1.10)$$

ρ_S and ρ_T denote the density of states (DOS) of tip and sample and E_F the Fermi energy. In this manner, only a model for the tip structure is required to deduce the tunneling current, which however is not trivial at all, as its exact shape in experiment is usually unknown.

For mathematical reasons, most models start from strong simplifications like assuming a pure elastic one-electron tunneling process, e. g. the Tersoff-Hamann model, which will be described in the next section. In that way, interactions leading to the origination of phonons, plasmons or other losses [Inelastic Tunneling, see Sec. 1.3.3] are not considered at all [15]. More realistic models, accounting for high temperatures, large bias voltages or more complex sample systems like adsorbed organic molecules, quickly become mathematically highly demanding [15, 44–47]. Up to now, no complete theory capable of a description of all phenomena is available [43].

1.1.2 Description of the Tunneling Tip

Tersoff and Hamann [48, 49] have been the first to apply the transfer Hamiltonian approach to STM. They used the most basic model by assuming the

tip as a sphere of radius R and assumed its wave function as a s-orbital isotropically propagating in all directions [see Fig. 1.4]. In addition, it is required that tip and sample stay in vacuum and are composed of the same material exhibiting identical work functions. Another simplification, which was not regarded within the original approach, replaces the tip by a single atom. But, it leads to the same result [43].

According to Bardeen the wave functions of tip and sample both need to satisfy the vacuum Schrödinger equation at the interface A

$$[\Delta - \kappa^2] \Psi = 0, \quad (1.11)$$

whereas $\kappa^2 = \frac{2m\Phi}{\hbar^2}$ is the minimum inverse decay length of the wave functions and Φ the effective local potential barrier height, proportional to the effective local work function. The rather complicated solution for the tip wave function is given by the spherical modified Bessel function of second type:

$$\Psi_\nu^T(\vec{r} - \vec{R}) \propto \frac{e^{-\kappa|\vec{r}-\vec{R}|}}{\kappa|\vec{r}-\vec{R}|}, \quad |\vec{r} - \vec{R}| \neq 0. \quad (1.12)$$

To calculate the tunneling current Eq. 1.12 is inserted into Eq. 1.9. Using the Green function of the Schrödinger equation ($\kappa k_0(\kappa|\vec{r} - \vec{r}'|)$) yields in:

$$M_{\mu\nu}(\vec{R}) \propto \frac{2\pi\hbar^2}{\kappa m} \Psi_\mu^S(\vec{R}), \quad (1.13)$$

and if regarding only small bias voltages and a structureless DOS of the tip ($\rho^T = const.$) finally leads to

$$I(\vec{R}, U_{\text{bias}}) \propto \frac{16\pi^3\hbar^3 e}{\kappa^2 m^2} U_{\text{bias}} \rho^T \rho_{loc}^S(\vec{R}, E_F^S). \quad (1.14)$$

Thus, Eq. 1.14 comprises the influence of the electronic sample structure, and the strongly exponential distance dependence, which becomes visible if regarding that the sample wave function $\Psi^S(\vec{R}) \approx e^{-\kappa z}$ is exponentially decreasing into vacuum. Despite its strong simplifications the Tersoff-Hamann model works well for many cases and is justifiable if keeping in mind that the front most tip atom gives the strongest contribution to the tunneling current. In this manner, the majority of STM images are to a first approach interpreted on the basis of this model.

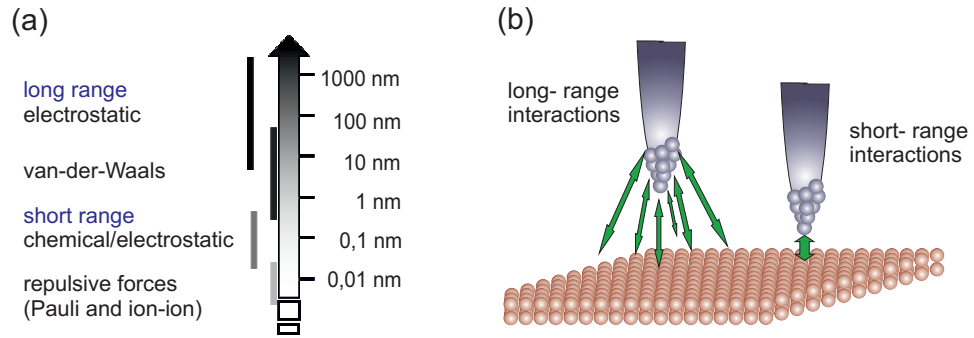


Figure 1.5: Force contributions and the influence of the AFM tip. **(a)** Dominating force contributions at different tip-sample separations. **(b)** For long-range forces the whole mesoscopic tip has to be taken into account while for short-range interaction only the front-most atoms play a role.

1.2 Interaction Forces

The close proximity of tip and sample can not only lead to a tunneling current, but furthermore causes several different interaction forces, which are often neglected for the interpretation of pure STM images. Their sum, the total interaction force, is subject to AFM and detected by means of a force sensor, which is most often constructed by a flexible cantilever beam on which the scanning tip is mounted. In case of a *qPlus* [25, 38] tuning fork for instance, as shown in Fig. 1.1, it is the free prong that acts as cantilever. Generally, atomic force microscopes come up with numerous possible operation modes customized for different application fields [16, 39, 50, 51]. The main distinction concerns, whether the force sensor is operated in a static manner, or dynamically, meaning that it is always deliberately vibrated above the surface close to or at resonance. At small tip-sample-separations z the interaction forces cause a slight bending of the force sensor which is exploited within the static modes [16]. On the other hand, changes in the oscillation properties, like the amplitude, frequency or phase, are subject to dynamic modes. The following introduction will be restricted to non-contact AFM (nc-AFM) in the dynamic frequency modulated mode (FM) [52]. Commonly used in ultra-high-vacuum (UHV) for high resolution investigations of nanostructures, this technique was also used throughout the whole thesis.

All forces that contribute in AFM are of electromagnetic origin. For different tip-sample distances, different interactions dominate, which is depicted in Fig. 1.5 (a)^{II}. Generally, they can be separated into long range (lr) [electrostatic long range $F_{el,lr}$, and van der Waals (vdW) F_{vdW}] and short range (sr) [electrostatic short range $F_{el,sr}$, chemical F_{chem} , Pauli- and ion-ion repulsion F_{rep}] forces. For a description of the long-range interactions (F_{lr}) with ranges

^{II}Capillary forces are neglected because they are not present in an UHV environment.

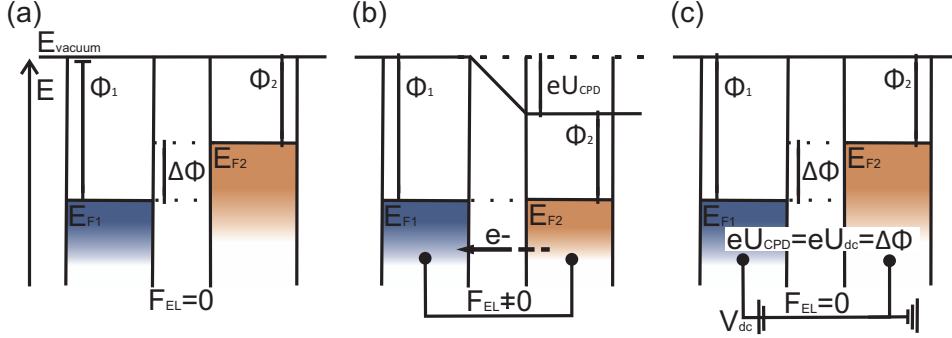


Figure 1.6: Origin of the CPD. (a) Two separated materials (tip and sample) with work functions Φ_1 and Φ_2 and Fermi energies E_{F1} and E_{F2} . (b) Establishing of an electrical connection causes a CPD, and hence an electrical force F_{el} . (c) Compensation of the field by applying $U_{\text{bias}} = U_{\text{dc}} = -U_{\text{CPD}}$.

of several tenth of nm the whole mesoscopic tip needs to be taken into account while short-range forces (F_{sr}) exhibit stronger distance dependencies with decay lengths of a few \AA . Hence, only the front most tip atoms play a role [see Fig. 1.5 (b)]. The total interaction force F_{TS} is given by

$$F_{\text{TS}} = F_{\text{lr}} + F_{\text{sr}} = F_{\text{el,lr}} + F_{\text{vdW}} + F_{\text{el,sr}} + F_{\text{rep}}, \quad (1.15)$$

and each contribution will be further described in the following section.

1.2.1 Force Contributions

Electrostatic Interactions

Differences in the work function of the electrically connected tip and sample cause a contact potential difference (CPD). Its origin is illustrated in Fig. 1.6 by using the example of two initially separated metallic materials with work functions Φ_1 and Φ_2 and Fermi energies E_{F1} and E_{F2} (a). Establishing an electrical connection (b) provokes that electrons flow from material 2 to 1 until $E_{F1} = E_{F2}$, while the local vacuum level is lowered by $eU_{\text{CPD}} = (\Phi_1 - \Phi_2) = \Delta\Phi$. Hence, an electric field $F_{\text{el,lr}}$ builds up, which gives rise to a **long range electrostatic force**, similar to a charged capacitor. By applying an appropriate bias voltage $U_{\text{bias}} = -U_{\text{CPD}}$ the electric field, and corresponding force, become compensated (c). This is subject to a sub field of AFM, Kelvin Probe Force Microscopy (KPFM), or local bias spectroscopy [see Sec. 1.3.2].

If an insulating tip and sample are to be regarded instead, long-range electrostatic forces can arise due to localized charges, or the polarizability of tip and sample [16]. On the other hand, if the tip is insulating, while the sample is conductive (or vice versa), electrostatic forces can be caused by image charges provoked by localized surface charges [53]. All these electrostatic

long range interaction forces are subject to the Coulomb law. Mathematically, the tip-sample geometry can be described as plate capacitor with the capacitance $C = C(z)$, which depends on the tip-sample distance z , and on the tip structure. If the latter is assumed as a truncated cone which ends in a half sphere with radius R [54], the electrostatic force is given by

$$F_{el} = \frac{1}{2} \frac{\partial C}{\partial z} (U_{\text{bias}} - U_{\text{CPD}})^2 = -\pi\epsilon_0 \frac{R^2}{z^2} (U_{\text{bias}} - U_{\text{CPD}})^2, \quad (1.16)$$

where U_{bias} refers to the applied bias voltage between tip and sample, and U_{CPD} to the contact potential difference, needed to compensate the electric field across the sample surface.

If the tip-sample distance becomes smaller than the surface lattice spacing, variations of the CPD down to the atomic level can be detected [31,32,55–58]. This is referred to as local contact potential difference (LCPD), and hence attributed towards changes in the local work function, which will be subject to Sec. 4.2. Its origin was controversially discussed [see [59] and the references therein]. Altogether, the physical origin of LCPD variations are subject to **short range electrostatic forces** $F_{\text{el,sr}}$, which can arise for instance from local surface dipoles, inhomogeneous charge (re-) distributions, or polarization effects [60, 61], but also from chemical interactions [57]. Within the multiscale approach presented by A. Sadeghi et al. [62–64], LCPD variations are treated by looking at the electrostatic long range force $F_{\text{el,lr}}$ between the mesoscopic tip and the sample, which acts on the tip apex. Atomic scale variations can then be directly connected to dipole moments induced in the tip apex via localized charge variations across the surface. It should be noted that both, the CPD and LCPD strongly depend on the geometrical and chemical composition of the tip apex, and for quantitative analysis an adequate calibration is necessary [59].

Van der Waals Interactions

Long range van der Waals (vdW) interactions are always present in AFM and thus the most dominant force contribution. They originate from fluctuations of dipole-dipole interactions. Mostly, they can be related to dispersion forces which arise if statistical charge fluctuations within the atomic shells temporarily lead to electric dipole moments within an atom. This in turn can induce a dipole moment in a second atom close by. Consequently, the two start to attract each other.

The vdW-force between two atoms can be described by a $F \propto z^{-7}$ law for small tip-sample separations, whereas it reduces to $F \propto z^{-8}$ for distances beyond $z \approx 5$ nm [16, 65]. The relation for the extended macroscopic tip-sample geometry can be derived by integration over the interactions between all contributing atoms. For this purpose, Hamaker suggested the assumption

of pairwise additive and non retarded forces [66]^{III} and regarded the tip as sphere with radius R which resulted in

$$F_{vdW} = -\frac{HR}{6z^2}. \quad (1.17)$$

H denotes the so called Hamaker constant (10^{-19} J), and z the tip-sample distance. The strength of vdW-interactions scales with the tip radius R . The smaller it is, the smaller their impact.

Chemical Forces and Repulsion

For tip-sample distances $z \leq 1$ nm the electronic orbitals of tip and sample significantly start to overlap, and chemical interactions become important. By slowly decreasing z first directed covalent bonds begin to form between the front most tip atoms and surface leading to **attractive chemical forces**, because the bond formation reduces the total energy. For stronger orbital overlaps through a further decreased z the Pauli principle leads to **Pauli repulsion** and the missing electron shielding of the charged ion cores to **ion-ion-repulsion**.

Mathematically F_{sr} can be described by the empirical **Lennard-Jones (LJ) potential** [67]

$$V_{LJ}(z) = E_0 \left(\left(\frac{z_0}{z} \right)^{12} - \left(2 \frac{z_0}{z} \right)^6 \right), \quad (1.18)$$

where E_0 is the binding energy and z_0 the equilibrium distance. The term $\approx z^{-6}$ is related to attractive interactions; the one $\approx z^{-12}$ to repulsive ones. An equivalent alternative model potential is given by the **Morse potential** [68], which was originally meant to describe the potential energy for a two atomic molecule:

$$V_M(z) = D_0(e^{-2a(z-z_0)} - 2e^{-a(z-z_0)}), \quad (1.19)$$

where z_0 is the equilibrium distance (lowest potential energy), a a characteristic constant and D_0 the energy minimum for $z = z_0$.

1.2.2 Dynamic Operation and Spatial Resolution

The trajectory of the oscillating movement of a dynamically operated force sensor can be described by

$$z(t) = A_{\text{osc}} \sin(\omega t + \phi) = A_{\text{osc}} \sin(2\pi f_0 t + \phi), \quad (1.20)$$

whereas A_{osc} is the oscillation amplitude, ϕ the phase between actual amplitude and excitation signal, and $\omega = 2\pi f_0$ refers to the oscillation frequency,

^{III}Actually, influences of third atoms within the continuum can not be excluded. Applying the Lifshitz theory circumvents this problem but is mathematically much more elaborate. However, both approaches result in the same distance dependence.

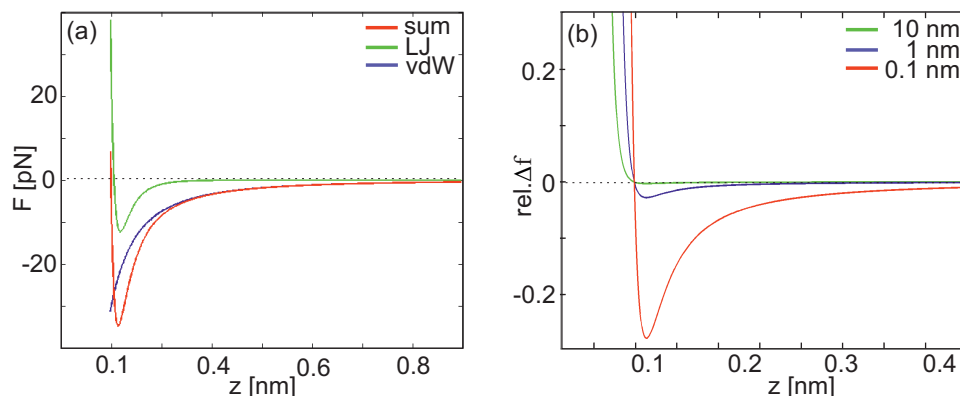


Figure 1.7: Interaction forces in AFM and the influence of the oscillation amplitude **(a)** Plots of the short- and long-range forces described by the LJ- and vdW-force laws and their sum describing the total interaction force in AFM. **(b)** The total interaction force for different oscillation amplitudes, according to Eq. 1.25.

which in the FM operation mode [52] is always carried out at the resonance frequency f_0 . While a detailed introduction is given in Sec. 1.3.1, here we only need to know, that two of the dynamic properties, A_{osc} , and ϕ , are externally controlled. In this manner, the interaction forces are detected via the shift Δf of the resonance frequency f_0 in the interaction free case, and f , the resonance frequency of the force sensor being close to the surface, which is already affected by F_{ts} :

$$\Delta f = f - f_0 = \frac{1}{2\pi} \left(\sqrt{\frac{k}{m}} - \sqrt{\frac{k + \langle k_{\text{ts}} \rangle}{m}} \right). \quad (1.21)$$

k refers to the spring constant of the force sensor, m to its mass, and $\langle k_{\text{ts}} \rangle$ to a spring constant attributed towards F_{ts} . The origin of the frequency shift Δf will be discussed in the following section.

Atomic resolution in AFM arises if F_{ts} varies at the atomic scale and thus is dominated by short-ranged force contributions. Frequently, it can be explained by bond formations through attractive chemical forces that are formed and ruptured upon the force sensor oscillation, like for instance for the prototype Si(111)-(7x7) surface [14, 69]. On the other hand, for insulating surfaces like ionic crystals short-range electrostatic interactions lead to atomic contrast which arise by the alternating charges of neighboring atoms which interact with a tip of a certain polarization (or a tip with a certain charge at its apex) [70]. However, obtaining high resolution is generally more difficult compared to STM which is due to the general impact of the long-range contributions and a non-monotonic force-distance relation [see Sec. 1.3.1].

The interplay of short- and long-range forces is illustrated in Fig. 1.7 (a) by assuming that the total interaction force is solely comprised by the sum

of long-range vdW interactions (blue) and short-range forces (green). The smaller the impact of vdW forces, the more the total interaction force equals the Lennard-Jones potential and hence, is dominated by the short-range force contributions responsible for high resolution. As already mentioned, practically the impact of vdW interactions can be reduced by working with atomically sharp tips (small R).

Another important aspect concerns the choice of oscillation amplitude needs to be taken into account. Because the tip is oscillated perpendicular to the surface, at different $z(t)$ of its trajectory different force contributions dominate, and short-range interactions only play a role at the lower turning point, which is a rather small fraction of the oscillation period. The smaller the amplitude the higher the measurement sensitivity towards short-range forces. This is illustrated in Fig. 1.7 (b), where the total interaction forces is plotted for three different amplitudes by using Eq. 1.25 which will be derived in the next section.

1.2.3 Origin of the Frequency Shift

In order to rule out the influence of the total interaction force F_{ts} on the measured frequency shift, a closer look towards the description of the motion of the force sensor becomes necessary. Within the theory of elasticity it can be described by a damped harmonic oscillator [71]:

$$m\ddot{z} = -kz + F_{ts}(z), \quad (1.22)$$

where m is the effective mass, and $z = z_0 + A_{osc}\sin(\omega t)$ harmonic trajectory of the vertical tip position. The fact that A_{osc} is always kept constant allows the assumption that the internal friction of the force sensor is fully compensated by the energy introduced by the excitation.

In case of **small amplitudes** (small compared to the characteristic decay length of the respective force, $A_{osc} < 100$ pm) the tip-sample interaction disturbs the cantilever motion over the whole oscillation cycle, and Eq. 1.22 can be solved by a linear expansion. The result gives a simple connection between Δf and the force gradient $\frac{\partial F}{\partial z}$:

$$\frac{\Delta f}{f} = -\frac{1}{2k} \frac{\partial F}{\partial z}. \quad (1.23)$$

For **larger amplitudes** ($A_{osc} > 100$ pm), the harmonic potential of the cantilever is only disturbed when the tip moves through the lower turning point of the oscillation. Substituting $z = z_0 + A_{osc}\sin(\omega t)$ into Eq. 1.22, multiplying by $\sin(\omega t)$ and integrating over one oscillation cycle $T = \frac{2\pi}{\omega}$ results in a relation between Δf and the force:

$$\pi A_{osc} \left(\frac{k}{\omega} - \omega m \right) = \int_0^{\frac{2\pi}{\omega}} \sin(\omega t) F_{ts}(z_0 + A_{osc}\sin(\omega t)) dt. \quad (1.24)$$

A simplification is gained by applying the approximation of $\Delta f \ll f_0$ and by rewriting Eq. 1.24 for n oscillation cycles:

$$Ak \frac{\Delta f}{f_0} = \frac{1}{2\pi n} \int_0^{2\pi n} \cos(\theta) F_{\text{ts}}(z(t)) d\theta, \quad (1.25)$$

where $\theta = 2\omega t$ refers to the phase. This result was first derived by Giessibl, but in a mathematically more difficult way based on a perturbation approach [72].

By modeling F_{ts} with linear combinations of the different force contributions and inserting it into Eq. 1.25 leads to analytic expressions for $\Delta f(z, A)$ [73]. On this basis, the so called normalized $\Delta f \propto A_{\text{osc}}^{-\frac{3}{2}}$ was introduced, being helpful for a comparison of AFM measurements recorded with different tips and/or A_{osc} . Its role is similar to that of the tunneling impedance in STM on metals [39]. Nevertheless, the main utilization of Eq. 1.25 is given by its application in the reverse way which is subject to Dynamic Force Spectroscopy [see Sec. 1.3.2].

1.2.4 Energy Dissipation in nc-AFM

At small tip-sample separations non-conservative dissipative forces might contribute as well. To keep the oscillation amplitude constant in this case an increased excitation amplitude A_{exc} is needed which serves as a measure for the dissipated energy E_{diss} [74]:

$$\Delta E_{\text{diss}} = \pi k \frac{A_{\text{osc}}^2}{Q} \left(\frac{A_{\text{exc}}}{A_{\text{exc},0}} - 1 \right). \quad (1.26)$$

Here, Q is the quality factor of the force sensor, and $E_{\text{CL},0} = \pi k \frac{A_{\text{osc}}^2}{Q}$ the energy stored in the cantilever motion in the interaction free case.

Contrast in the A_{exc} channel can be particularly expected for low symmetry and/or low coordination tip-sample configurations, and even occurs at the atomic scale [14, 75]. While a good overview about different underlying mechanisms of dissipation is given in [76, 77], here only two main mechanisms are distinguished, velocity- and hysteresis dependent damping. It should be mentioned that the non ideal behavior of the instrument or inadequate choice of feedback parameters especially at high scan speeds can also lead to an increased A_{exc} which are subsumed under the phenomena of **apparent damping** [78].

In case of **velocity dependent damping** the cantilever's equation of motion is extended by a term containing a dissipation/friction force proportional to the tip velocity. Mainly two origins have been proposed: the *Joule*- and the *Brownian* dissipation. The first one is mediated by long-range electrical fields [79], while the latter relies on fluctuations of atomic positions coupled by short-range forces.

On the other hand, non velocity dependent, but **hysteresis dependent damping** is related to tip-sample interaction energies that are bistable in a finite range of displacements. That way, force jumps occur at different positions in the for- and backward motion of the tip. If induced by *adhesion forces* they show up in a stronger tensile force needed for the contact breaking of a „jump-to-contact“ than for its formation [80,81]. On the other hand, *atomic instabilities* cause damping by local rearrangements of one or a few low coordinated tip or sample atoms, before multi atom adhesive contacts are formed at further decreased z [82,83]. Anyhow, it might be difficult to distinguish these for instance from thermal activations. Note furthermore, that the distinction of velocity- and hysteresis dependent damping mechanism starts to smear out at finite temperatures.

1.3 Operation with a *qPlus* Tuning Fork Sensor

Probably never would J. Shore, the inventor of the tuning fork, have been able to foresee that surface science physicists would start to use them in order to image atoms [14] or single chemical bonds within molecules [18]. Being a musician in the eighteenth century, he invented a tool for the purpose of tuning his lute, and just for fun, and due to the similar shape, he named it pitch fork at first. Physically, a tuning fork is an acoustic resonator with the shape of a two prong fork. The main characteristic concerns the fact that vibration of a tuning fork leads to a resonance at a specific constant very pure tone (pitch), which depends on the lengths of the prongs. In the ground oscillation mode, both oscillate in a mirrored fashion, so that the center of mass stays at rest and all forces become compensated inside the material by which the prongs are connected. Still today, metal tuning forks with $f = 440$ Hz define the standard pitch by which music instruments are tuned and almost every music conductor owns one.

Even more popular, however, might be the tiny quartz made tuning forks widely incorporated into electric devices like watches. Working as time keepers, they were invented in 1927 by W. Morrison and J. W. Horton. Thanks to the piezo electrical effect of quartz, by which mechanical stress can be transformed into electrical charge separation and vice versa, they can be driven fully electrically by applying small oscillation voltages to the metal electrodes contacted to the tuning fork surfaces.

When it comes to SPM methods, the first utilization of a tuning fork based sensor goes back to Günther et al. [84], who applied it in a scanning near field microscope. However, the type of tuning fork sensor relevant for the present thesis, is given by the *qPlus* sensor, which was developed by Giessibl [25, 38]. Here, one prong is fixed towards a substrate, which was depicted in Fig. 1.1, in principle resulting in a piezoresistive cantilever with tip [85].

While the most commonly used force sensors are given by micromachined silicon cantilevers, *qPlus* tuning forks [25, 38] gain successively increasing popularity, which is due to several reasons. A major advantage is given by the fact that the sensor actuation needed for dynamic operation, as well as the signal read out can be accomplished in a pure electric manner, while only two electrical contacts are needed. This makes the integration into SPM, particularly for low temperature environments, quite simple [39, 86]. Also, the high frequency stability with temperature and time is an important issue. Furthermore, they possess a comparably high stiffness of 1800 N m^{-1} ^{IV}. Because the measurement stability for dynamic AFM operation scales with the stiffness and oscillation amplitude of the sensor [39], *qPlus* tuning forks

^{IV}The stiffness of conventional Si based cantilevers accounts to $k_{\text{si}} \approx 10 \text{ N m}^{-1}$ to 50 N m^{-1} . A second alternative probing sensor, also on quartz basis, introduced by Specs Zurich GmbH, is the Kolibri sensor [87, 88], where even stiffnesses of $k_{\text{kolibri}} \approx 540 \text{ kN m}^{-1}$ are reached.

enable the operation at amplitudes down below the 1 nm scale. This highly increases the measurement sensitivity towards short-range interaction forces, for which A_{osc} should be ideally tuned to the same magnitude as the decay length of the short-range forces $\kappa_{sr} \leq 1$ nm, which was discussed in Sec. 1.2.1. For conventional Si based cantilevers, small oscillation amplitude operation can only be carried out by using multimodal modes, featuring the actuation of higher harmonics [89–95], which is technically more elaborate.

The possibility of ultra small amplitude operation is also the reason, why by means of a *qPlus* force sensor the obtainable spatial resolution could be pushed forward to imaging single chemical bonds within molecules [18]. Here, the contrast mainly arises due to short-range Pauli interaction forces [96]. These only dominate the measured frequency shift, if operating with nanometer scale oscillation amplitudes, while approaching the tip as close as possible before a multi-atom contact is formed [96].

Concerning the simultaneous STM and AFM operation, which can actually be tuned by any force sensor, a main advantage of tuning forks concerns, the fact, that principally tips of any material can be glued to the free prong. In contrast to conventional Si based cantilevers, this allows for purely conductive tips. Furthermore, the use of small amplitudes is advantageous for the current detection, because the vertical oscillation of the force sensor causes an oscillation of the distance dependent tunneling current as well [see Sec. 1.3.1].

1.3.1 Topography and Feedback Operation

By scanning the tuning fork laterally above the sample surface, topographic images are recorded, and in case of conductive samples, both I_t and Δf can be measured at the same time. For this purpose, three different options are available, which are illustrated in Fig. 1.8: the constant current- (a), constant frequency shift- (b), and constant height (c) mode. In contrast to conventional STM the measured tunneling current for an oscillating tip, which is important upon simultaneous operation, is given by [39]

$$\langle I_t(z, A_{\text{osc}}) \rangle \approx \frac{I(z, 0)}{\sqrt{4\pi\kappa_t A_{\text{osc}}}}. \quad (1.27)$$

If necessary, the absolute tunneling current can then be extracted a posteriori by applying the algorithms described in [97]. The experimental setup of the feedback operation for a tuning fork based SPM are depicted in Fig. 1.9, and will be described in the following sections.

Constant Current Mode

The elements necessary for feedback operation via a constant current I_t in Fig. 1.9 are highlighted in green. The actual current is converted into a

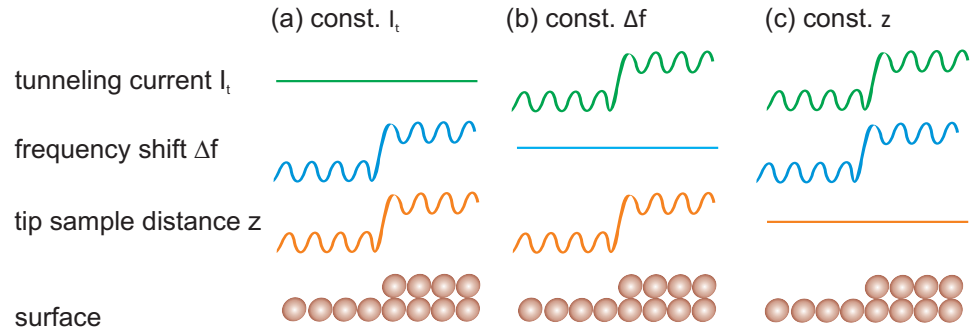


Figure 1.8: Scheme of the three simultaneous topographic operation modes available with a tuning fork. **(a)** The constant current mode which is related to STM feedback operation, **(b)** the constant frequency shift mode, related to AFM, and **(c)** the constant height mode, also available in single STM and AFM measurements.

voltage, preamplified, and then forwarded to a feedback circuit which is designed to maintain a constant I_t by regulating the tip-sample distance with respect to its exponential distance dependence. The output signal is passed through a high-voltage amplifier and returned to the z - electrode of the piezo electric drive which adjusts the tip-sample distance accordingly.

The resulting contour maps $z(x, y)$, also denoted as „topography signal“, are usually not only determined by the surface arrangement, but rather reflect a constant current map where also specific local sample and tip properties contribute. Within the Tersoff-Hamann model [see Sec. 1.1.2] constant current maps can be interpreted as maps of constant local density of states (LDOS) at the Fermi level.

Constant Frequency Shift Mode

The parts needed for constant Δf feedback operation are displayed in blue (right side). At each scanning point the actual A_{osc} , f and Φ are measured. In order to keep the force sensor oscillation always at resonance with constant amplitude, a phase locked loop (PLL) is utilized (self excitation mechanism). Therein, the signal being proportional to the actual amplitude is phase shifted by $\pi/2$ to ensure resonance. Furthermore, the amplitude feedback circuit provides the enhancement factor V needed to keep the amplitude constant. Both are amplified, and returned to the free prong, whereas Δf serves for distance control. It is regulated to a certain set-point by adjusting the tip-sample distance. Also in AFM a bias voltage can be applied between tip and sample e. g. in order to compensate CPD differences or electrostatic forces due to localized charges.

At a first glance the distance regulation units in STM and AFM seem to be similar. But, in AFM there are more technical obstacles to overcome because contrary to the rapid exponential decrease of I_t with distance the

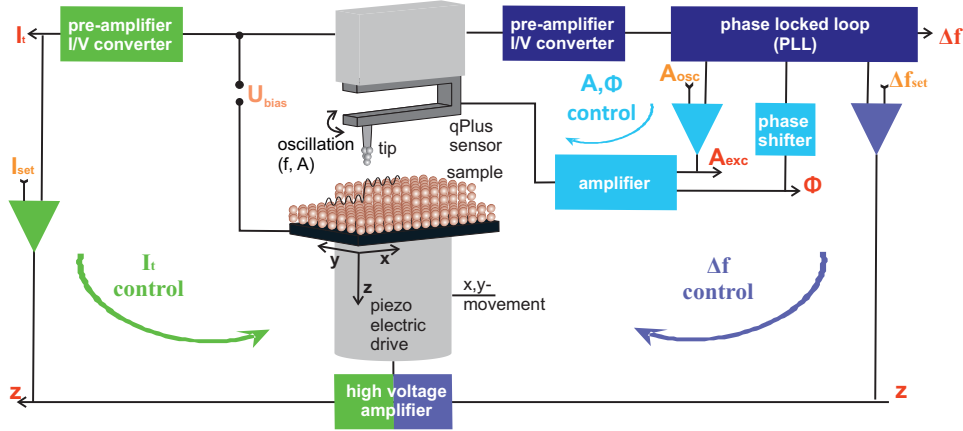


Figure 1.9: Scheme of a *qPlus* tuning fork sensor scanning over a sample surface and the corresponding feedback circuits utilized for the different operation modes. Left side: STM feedback operation. Right side: FM-AFM operation. Simultaneous recording of both signals possible.

$F(z)$ relation is non-monotonic. It is attractive for larger distances and becomes repulsive for smaller ones. This makes stable feedback operation more difficult, and necessitates to restrict the range of probed z - values to a monotonic detail of the entire curve^V.

Similar to the constant current mode the topography maps $\Delta f(x, y) = \text{const.}$ do not directly reflect the surface topography, but rather a snapshot of the complex interplay between the different contributing interaction forces. The actual ratio of the different forces is influenced by the actual tip apex conditions as well as by the magnitude of the oscillation amplitude [93, 98, 99] [see also Sec. 1.2.2]. With Eq. 1.25 constant frequency shift maps can be interpreted as maps of constant total interaction force.

Constant Height Mode

By using the constant height mode both distance regulating feedback circuits are switched off completely, whereas amplitude control remains active. The variations in I_t and Δf are recorded as a function of the probe position at a certain constant height above the surface. The absence of a feedback loop can facilitate much faster scan speeds compared to the *Constant Current* or *Constant Frequency Shift* mode, so that image distortions due to piezoelectric creep or thermal and electronic drift become reduced. Furthermore, the influence to most low frequency disturbances is decreased. However, tip

^V Additionally, (i) AFM features an enhanced probability of so called „jump-to-contacts“ of the tip due to the flexible cantilever which is attracted by interaction forces (e. g. van-der-Waals). Finally, (ii) high resolution imaging can be perturbed by the unavoidable non site- specific long- range force contributions which are always present [see Sec. 1.2.1].

crashes are very likely and in order to avoid them, the surface should be thoroughly investigated with the *Constant Current* mode before.

Comparison of the Different Operation Modes

The advantages and disadvantages of the different operation modes are described in [100]. Presupposing that ultra-high resolution is desired, the disadvantage of the constant Δf - mode lies in the non trivial force-distance relation. For intramolecular resolution down to single chemical bonds within a molecule, the repulsive interaction force regime needs to be employed, which leads to several experimental problems regarding stable feedback operation [100]. In this manner, the constant I_t mode can be advantageous. This is due to the tunneling current's monotonic distance dependence for all separations.

However, since constant current operation probes a convolution of topography and the sample LDOS, the simultaneously recorded Δf might be altered by non-topography related LDOS changes^{VI}. Therefore, simultaneously recorded Δf maps never correspond to constant height maps, and therefore should be interpreted with care and cross-checked with constant height- or spectroscopic measurements of the same surface area.

In conclusion, the *Constant Height Mode* is preferable in terms of data interpretation. However, for the imaging of three dimensional objects like C_{60} [96] images with the *Constant Current Mode* can lead to an increased lateral area in which atomic contrast within the molecule can be observed. [see. Fig. 1 in [100]].

1.3.2 Spectroscopy

No matter which operation mode used, topographic images always reflect a convolution of topography with electronic sample properties and/or the total interaction force, as it was described in the last section. Accordingly, extraction of quantitative information about the respective properties can be rather challenging. On the other hand, a direct and unambiguous investigation of the electronic surface structure, or its potential energy landscape, can be obtained in a straightforward manner by spectroscopic operation.

Within a spectroscopic measurement the tunneling current and/or frequency shift are recorded either as a function of the tip-sample distance^{VII}, or the applied bias voltage^{VIII}. Therefore, the tip is first stopped at a certain lateral

^{VI}The same would occur within the constant Δf mode where a topography map is connected to a map of constant F_{ts} .

^{VII}Measured relative tip-sample distance due to the cantilever displacement minus an *a posteriori* determined constant.

^{VIII}For completeness, it has to be noted that also a mode recording $z(U_{\text{bias}})$ is available, which however was not relevant for this thesis.

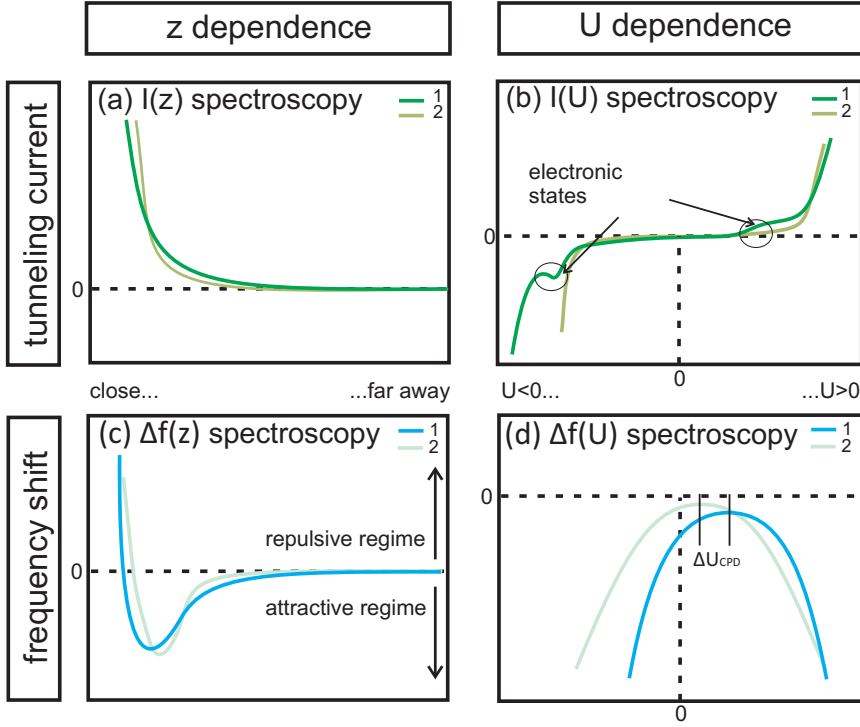


Figure 1.10: Spectroscopy operation modes by tuning fork based AFM/STM: (a) local barrier height- ($I(z)$) (b) scanning tunneling- ($I(U)$), (c) dynamic force- ($\Delta f(z)$), and (d) local bias- spectroscopy ($\Delta f(U)$).

position above the surface and stabilized. Subsequently, the distance regulation feedback circuit is switched off for recording the spectra, while the amplitude feedback remains active. The four available modes $I(z)$, $\Delta f(z)$, $I(U)$, and $\Delta f(U)$ are illustrated in Fig. 1.10, and will be separately introduced in the following.

Local Barrier Height Spectroscopy

$I_t(z)$ spectroscopy is also referred to as Local Barrier Height Spectroscopy. Typical curves are depicted in Fig. 1.10 (a). They clearly reflect the exponential dependence of I_t . Within the one dimensional treatment in Sec. 1.1 the tunneling current in accordance to Eq. 1.1 is given by

$$I_t \propto e^{-\kappa z}, \quad \text{whereas } \kappa \propto \phi. \quad (1.28)$$

In this manner, it is a measure for the apparent barrier height ϕ , which in turn is related to the effective local tip-sample work function Φ , and which can be extracted by logarithmic fitting [101]. Actually, the accurateness of the method suffers from this simple approach, because the actual tip-sample geometry is much more complicated [44, 102, 103], and the AFM provides

a more reliable and exact method given by Kelvin Probe Force Microscopy (KPFM) or local bias spectroscopy [31, 104, 105]. On the other hand, $I_t(z)$ recorded at different positions above the surface can be used to investigate the local conductance and LDOS as a function of the tip-sample distance z [96].

Scanning Tunneling Spectroscopy

In Scanning Tunneling Spectroscopy (STS) [15, 16, 27, 43] the tunneling current I_t is recorded as a function of the bias voltage U_{bias} . The two spectra in Fig. 1.10 (b) show that $|I_t|$ exponentially scales with $|U_{\text{bias}}|$. But how to interpret such data?

Founded on the Tersoff-Hamann model [Sec. 1.1.2] Feenstra et al. [106] related the differential conduction (dI/dU) to the sample LDOS. He regarded the case of varying U_{bias} at constant z and then integrated across the energy interval $[0; eV]$, yielding in:

$$\frac{dI}{dU} \propto \rho^S(\vec{R}, E_F^S + eU_{\text{bias}}). \quad (1.29)$$

A closer look at the dark green curve in Fig. 1.10 (b) now reveals two small shoulders, which already indicate changes in the sample LDOS within the $I(U)$ spectrum. A remarkable application of this LDOS dependence in STS is the ability to visualize molecular resonances [see also Sec. 4.5.2].

Technically, for obtaining the differential conductance, $I(U)$ has to be numerically differentiated. Thereby, the signal-to-noise ratio can be increased by averaging over few curves recorded at the same place (x,y,z), or in pure STM, where the tuning fork is not oscillated the Lock-In technique might be applied [22, 107–109]. Often, the $dI/dU(U)$ - signal is also normalized with I_t/U_{bias} for a better comparability of experimental data.

Especially for larger bias voltages, the simple model reaches its limit fast since the tunneling barrier itself is voltage dependent [15]. An extended interpretation is e. g. given by the semiclassical approximation named after G. Wentzel, H. A. Kramers and L. Brillouin (WKB) [110]. Therein, the introduction of a transmission coefficient provides that instead of $\rho_S(r_T^z)$ the DOS at the surface $\rho_S(0)$ can be considered while at the same time accounting for the voltage dependence.

Up to now, only elastic tunneling processes have been regarded. However, the tunneling current can also contain an inelastic fraction of electrons, which can be investigated by calculating the second derivative d^2I/dU^2 of the $I(U)$ spectra [111, 112]. A typical inelastic tunneling (IET) process is illustrated in Fig. 1.11, and is also often referred to as inelastic scattering of electrons at the vibrational modes of the surface/adsorbate. The schematic energy diagram in Fig. 1.11 (b) shows how electrons with energy $\frac{\hbar\omega}{e}$ can excite vibrational states upon injection into the adsorbate, before they flow into the

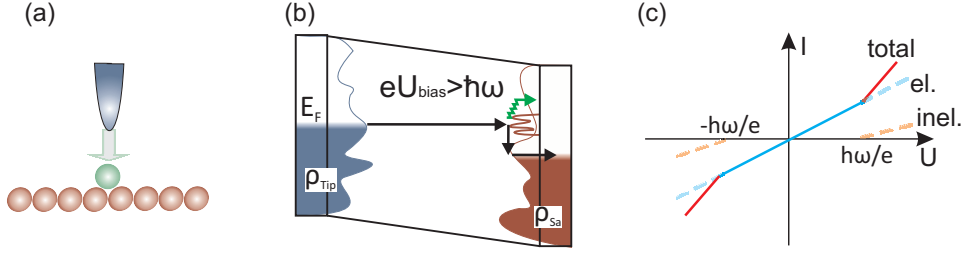


Figure 1.11: Inelastic tunneling (IET). (a) Scheme of an inelastic tunneling process. (b) Energy diagram, including vibrational states of the adsorbate. (c) A typical $I(U)$ curve. Starting from $V \geq \frac{\hbar\omega}{e}$ an additional channel for inelastic processes opens, that leads to steps in the corresponding $\frac{dI}{dU}$ curves.

substrate. A typical associated $I(U)$ spectrum can be found in Fig. 1.11 (c). Vibrational states of (molecular) adsorbates show up as steps in the corresponding dI/dU - maps.

Dynamic Force Spectroscopy

In Dynamic Force Spectroscopy (DFS) the frequency shift is recorded as a function of the tip-sample distance which allows to study interaction forces at specific atomic sites [113, 114] and moreover awards the AFM the possibility of determining the chemical identity of surface atoms [94, 114, 115]. However, in order to extract the interaction forces from measured $\Delta f(z)$ - curves Eq. 1.25 needs to be inverted as already mentioned in the last section. Actually, this is not straightforward and a full analytical inversion algorithm is not known. But, there are many different approaches utilizing either numerical procedures or calculating analytically but only after applying certain approximations first (e. g. shrinking the range for A_{osc}) [116–120]. Nowadays, the most widely used approach is the numerical one presented by Sader and Jarvis [120] which is valid for all amplitudes and exhibits an error of less than 5%.

Their derivation starts with a Laplace transformation of the interaction force F which enables an exact inversion of Eq. 1.25:

$$F(z) = \mathcal{L} \left\{ \frac{kA_{\text{osc}}}{T(\lambda A_{\text{osc}})} \mathcal{L}^{-1} \left[\frac{\Delta f(z)}{f_0} \right] \right\}. \quad (1.30)$$

$T(x) = I_1 \exp(-x)$ denotes the modified Bessel function of first order. By approximating $T(x)$ by

$$T(x) \approx \frac{x}{2} \left(1 + \frac{1}{8}\sqrt{x} + \sqrt{\frac{\pi}{2}}x^{\frac{3}{2}} \right) \quad (1.31)$$

the interaction force can be calculated as a function of the measured fre-

quency shift:

$$F_{\text{ts}}(z) = 2k \int_z^\infty \left[\left(1 + \frac{A_{\text{osc}}^{\frac{1}{2}}}{8\sqrt{\pi(t-z)}} \right) \Omega(t) - \frac{A_{\text{osc}}^{\frac{3}{2}}}{\sqrt{2(t-z)}} \frac{d\Omega(t)}{dt} \right] dt, \quad (1.32)$$

with $\Omega(z) = \frac{\Delta\omega(z)}{\omega_0}$. Accordingly, the potential energy $U_{\text{ts}}(z)$ is then found to be

$$U_{\text{ts}}(z) = 2k \int_z^\infty \Omega(t) \left((t-z) + \frac{A_{\text{osc}}^{\frac{1}{2}}}{4} \sqrt{\frac{t-z}{\pi}} + \frac{A_{\text{osc}}^{\frac{3}{2}}}{\sqrt{2(t-z)}} \right) dt. \quad (1.33)$$

To apply these equations and extract the interaction forces for a measured $\Delta f(z)$ - curve, all tip-sample distances starting from close to the surface up to distances where the tip is not affected by interactions any more (≈ 10 nm) need to be recorded.

By assuming only small or respectively large amplitudes Eq. 1.32 can be simplified:

$$F_{\text{ts,small}}(z) = 2k \int_z^\infty \Omega(t) dt, \quad (1.34)$$

$$F_{\text{ts,large}}(z) = 2k \int_z^\infty \frac{d\Omega(t)}{dt} \frac{1}{\sqrt{t-z}} dt. \quad (1.35)$$

These equations directly correspond to those previously presented by Albrecht et al. [52] for the small amplitude case ($A_{\text{osc}} < 100$ pm) and to those from Dürig [116] for larger ones ($A_{\text{osc}} > 100$ pm).

Two typical DFS curves at different sites are shown in Fig. 1.10 (c). For a detailed investigation of the short-range forces which is often desired, a vdW force subtraction can be accomplished [116]. Nevertheless, a main difficulty is given by the fact, that usually neither the exact tip shape and - composition nor the exact tip-sample separation are known. Thus, models need to be assumed, which strongly influence the obtained results.

Bias Spectroscopy

The last spectroscopic operation mode concerns the recording of Δf as a function of the applied bias voltage U_{bias} , and hence, is sensitive towards the electrostatic forces, as was already mentioned in Sec. 1.2.1. Two options are available: KPFM in which the applied bias voltage is varied in order to fulfill $U_{\text{bias}} = U_{\text{CPD}}$ dynamically at each scanning point by means of additional feed back operation [16, 121], or local bias spectroscopy, where Δf is statically probed at a certain position (x,y,z). While the static spectroscopy method does not offer the same speed than KPFM, advantages concern simple data acquisition as well as a more straightforward data interpretation.

The following discussion is limited to bias spectroscopy, as all measurements of this thesis concerned with electrostatic interactions were recorded with this method. Typical $\Delta f(U)$ curves are depicted in Fig. 1.10 (d). They feature a parabolic shape which is distance dependent: with decreasing tip-sample distance the parabolas shift laterally and vertically, and furthermore become steeper, which is due to the onset of short-range electrostatic forces. The angular points of the parabolas with maximal Δf correspond to U_{CPD} or U_{LCPD} , respectively, and thus provide access towards (local) work function variations [for the concept of the local work function see Sec. 4.2] via:

$$qU_{CPD} = -eU_{CPD} = \Phi_t - \Phi_s, \quad (1.36)$$

$$qU_{LCPD} = -eU_{LCPD} = \Phi_{t,local} - \Phi_{s,local}, \quad (1.37)$$

where Φ_t and Φ_s [$\Phi_{t,local}$ and $\Phi_{s,local}$] are the [local] work functions of tip and sample. In order to be able to extract absolute values, the tip-work function needs to be calibrated prior to the measurement. Otherwise, only work function differences across the sample surface are accessible ($\Delta U_{(L)CPD}$).

For a concrete case, it is essential, whether the tip or sample is grounded. If, like for the measurements presented in this thesis, the tip is biased (see Fig. 1.6), one has to substitute $q=+e$ in Eq. 1.37. The sensitivity that can be achieved within a bias spectroscopy measurement goes down to the characterization of single atoms and molecules [23, 31, 122], and recently, even changes within single molecules could be monitored [32, 105].

1.3.3 Manipulation

The first experimental evidence of atomic manipulation was presented by Eigler and Schweizer at IBM in 1990. They individually manipulated Xe atoms laterally [see Fig. 1.12 (a)] on the Ni(110) surface by using a STM at low temperature [123]. One year later, again at IBM, also vertical manipulation [124] and the reversible transfer of single atoms between the STM tip and a metal surface [125] were demonstrated [Fig. 1.12 (b)]. Up to now, numerous STM based studies were presented [33, 126–129], also for molecules [130, 131]. Also, several suggestions for technologically interesting devices have been made [125, 132–134]. However, since STM probes the LDOS information about forces involved into manipulation were rare [135], and quantitative analysis was eluded until the presentation of AFM based manipulation [34]. Similar to STM, lateral (2003) [136] and vertical (2005) [137] techniques are available, and both have been established for molecules as well [138–140]. Particularly, manipulation techniques were also presented for room temperature AFM, based on the interchange of atoms [99, 141]. One of the milestones in AFM manipulation concerns the possibility of quantitative force determination during manipulation [21, 94] as it was already suggested in 1991 by Stroscio and Eigler. By using a *qPlus* force sensor, Ternes et al. [21] measured the distance dependent force causing a lateral motion of an adsorbate,

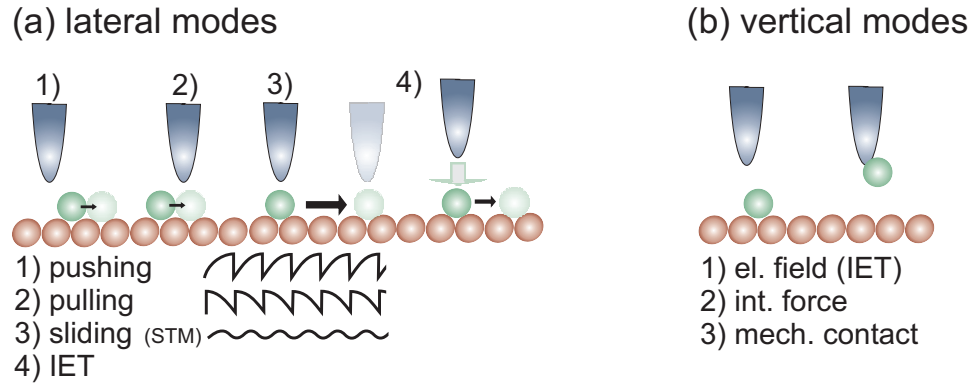


Figure 1.12: Scheme of different manipulation techniques in STM and AFM. (a) Lateral manipulation by pushing (1), pulling (2), and sliding (3, only STM). Below the schematic line profiles corresponding to the different manipulation modes are shown. (b) Vertical manipulation, and possible techniques to induce the movement.

being comprised by a lateral and vertical component. With decreasing tip-sample distance the lateral force exerted by the tip remains constant while only the vertical component increases.

Which manipulation technique is particularly efficient in a certain case strongly depends on the utilized sample. For low index crystalline metal surfaces with their low diffusion barriers lateral modes become possible in a straightforward manner. In contrast, due to the stronger directed covalent bonds, on semiconductors mostly inelastic tunneling (IET) processes were performed [142]. Finally, for insulating surfaces difficulties arise due the rather small adsorption energies, so that only little experimental evidence is available [34]. An exception is given for thin insulating films on a metal surface [see Sec. 3.3], where several IET based processes have been reported, thanks to the increased life times of adsorbate states [28, 134, 143–145] [see also Sec. 4.5.2].

Lateral manipulation

To induce a lateral manipulation, the tip is scanned across the adsorbate on the surface. Starting from a certain tip-sample threshold distance, the tip-sample interaction upon scanning becomes large enough to induce a lateral movement of the adsorbate along symmetric adsorption site directions. Three different modes are available (1) pushing (repulsive interaction), (2) pulling (attractive interaction), and (3) sliding [146] [see Fig. 1.12 (a)]. For the third one, the adsorbate follows the tip during the entire lateral movement. Its utilization is mainly restricted to STM operation, whereas in AFM it is only efficient at ultra-small amplitudes ($\approx 1 \text{ \AA}$). Thus is due to the oscillation of the tip which in case of larger amplitudes passes through the long range interaction regime in each oscillation cycle [34]. Alternatively, lateral

movements can also be induced by IET. For instance, the injection of electrons into the centre of a molecule leads to lateral movement into random directions, while directed movement is achieved for injection of electrons into off-center areas [147].

Vertical manipulation

Vertical manipulation involves the reversible transfer from the adsorbate between tip and sample [see Fig. 1.12 (b)]. It can be realized by electric fields, inelastic tunneling processes, the tip-adsorbate interaction force, or via a mechanical contact between tip and adsorbate. An understanding can be gained by looking at the double-potential-well model: The potential for the tip above an adsorbate at a certain tip-sample distance exhibits two minima configurations, corresponding to two stable positions of the adsorbate either at the tip apex or on the surface, which are separated by a barrier. By applying for instance an electrical field the potential becomes modified such that the barrier between the two wells is reduced leading to an easy transfer between the tip adsorption site and that on the sample.

Chapter 2

Multidimensional Spectroscopy Operation

In fact, spectroscopic investigations are not limited to 1D measurements at certain single specific sites as introduced in Sec. 1.3.2, but may also be utilized to probe complete surface details along predefined lines or even areas above the surface. The result are then two- (2D) or three-dimensional (3D) data sets, whereas the present discussion will focus on 3D datasets, as they present the most dense possibility of data collection. The recorded data might be arranged into a 3D data cuboid, exemplarily depicted in Fig. 2.1 (c) for the case of DFS. However, in accordance to the four spectroscopic operation modes introduced before, such a cuboid can contain $I_t(x, y, z)$, $\Delta f(x, y, z)$, $I_t(x, y, U)$, or $\Delta f(x, y, U)$ data. This can be studied along any two-dimensional cut or for each single curve. While the recording of 3D spectroscopy data is technically rather challenging, as will be outlined in the Sec. 2.3, the obtained data enables thoroughgoing investigations in real space. In this manner, plenty of valuable physical information can be deduced, which will be subject of the next section.

2.1 Advantages of 3D Spectroscopy

In contrast to single curves, a 3D data set probes a whole surface area, so that the information available by the four spectroscopic operation modes can be mapped with lateral and vertical sub nanometer resolution. This enables deep insights into the sample system, exceeding that obtained from the evaluation of single curves by far.

In case of 3D dynamic force spectroscopy (DFS) dataset of $\Delta f(x, y, z)$ [21, 29, 148–151] for instance, in a first step, 3D cuboids of the corresponding interaction forces $F_{ts}(x, y, z)$ [Eq. 1.32] and of the potential energy $U_{ts}(x, y, z)$ [Eq. 1.33] can be extracted. Thus, the whole surface potential energy landscape becomes probed, which provides important information about crystal

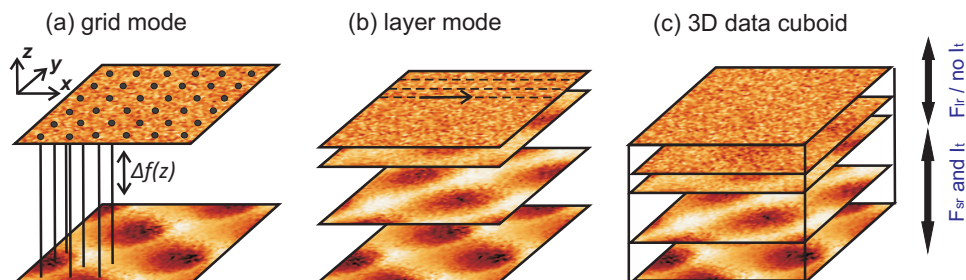


Figure 2.1: 3D data acquisition modes by using the example of 3D DFS: (a) grid-mode, (b) layer-mode, and (c) the resulting 3D data cuboid, containing all the rearranged data points.

growth, surface catalysis or also diffusion [30, 148]. Additionally, by differentiating constant height potential energy maps $U(x, y, z = \text{const.})$ in lateral directions, also the lateral force components become accessible [21, 152, 153]^I. So, in case of 3D data it will be generally distinguished between the vertical ($F_{\text{ver}}(x, y, z)$) and lateral force ($F_{\text{lat}}(x, y, z)$). Altogether, the force spectroscopy method awards the AFM with the possibility to chemically recognize surface atoms [94, 114, 155], and finally, by means of a tuning fork sensor, atomic scale characterizations of single molecules [18, 156], or their elastic properties can be probed [96, 157].

Similarly, by recording 3D $I_t(x, y, z)$ data, the distance dependence of the tunneling current across the surface can be studied. This enables thoroughgoing investigations about the local conductance and LDOS near the Fermi level [96]. For instance, by studying constant height maps of the tunneling current above C_{60} adsorbed on $\text{Cu}(111)$ the influence of the metal sample on the electronic structure of the molecule, mediated by charge transfer [see Sec. 4.5] could be revealed [100]. As will be discussed in Sec. 3.2, particularly for tuning forks in the old setup, and if $\Delta f(x, y, z)$ and $I_t(x, y, z)$ are to be recorded simultaneously, applied bias voltages in the μV regime are mandatory in order to avoid cross talk between the two channels. However, the comparison of both data then enables for simultaneous determination of the chemical structure together with the spatial electron density near the Fermi level, which might give complementary physical information about the system under investigation.

On the other hand, when it comes to the recording of $I(x, y, U)$, the LDOS of the sample is probed as a function of the bias voltage, giving deep insights about the electronic surface structure, also with sub nanometer resolution. This is of particular interest for molecular studies, as the frontier molecular orbitals can be directly visualized, e. g. if the latter are deposited on thin in-

^IThe calculation of lateral force components should be usually afflicted by a certain error caused by the fact that the cantilever oscillation occurs perpendicular to the surface. As an alternative it can be also deduced by exciting the torsional modes of a cantilever [154]

sulating films on a metal surface [28,144,145]. Here, it is sufficient to record a 1D spectrum to figure out the molecular resonances, before recording constant height images at these particular bias voltages, instead of acquiring a full 3D data set. In contrast to STS which is sensitive towards the electronic structure near the Fermi level, by means of $\Delta f(x, y, U)$ maps, the total electron density becomes probed. Such data sets recorded above single molecules can be used to reveal local electrostatic potential variations, which for instance can be related towards the inner distribution of charge within a molecule [32,105].

2.2 Data Acquisition Methods

Principally, two different acquisition methods are used, which work for all four spectroscopic techniques. They are depicted in Fig. 2.1 by using the example of a $\Delta f(x, y, z)$ data set. In the **grid-mode** [Fig. 2.1 (a)] [21, 29, 105], first a 2D (x, y) -grid is predefined above the surface. Subsequently, a 1D spectroscopic curve $I_t(z)$ [$I_t(U)$] and/or $\Delta f(z)$ [$\Delta f(U)$] is recorded at each grid point. In contrast, when using the **layer-mode** [Fig. 2.1 (b)] [30,158], a series of constant-height images^{II} is recorded above the surface, decreasing/increasing z after each image. Regardless of the method chosen, the results are three dimensional **data cuboids** containing the tunneling current and/or frequency shift as a function of the tip-sample separation or applied bias voltage [see Fig. 2.1 (c)].

For the recording of Δf and/or I_t as a function of the tip-sample distance z , the acquisition time, which scales with the density of the recorded data, can be considerably reduced. For $I_t(x, y, z)$ the recording can be stopped as soon as the tunneling regime is left. For $\Delta f(x, y, z)$ on the other hand, all distances up to experimentally ≈ 10 nm are necessary in order to be able to extract the interaction forces and potential energy. Here, the site specific data recording can be stopped at a tip-sample separation z where no atomic contrast/tunneling current is detected anymore. The remaining distance range containing the site independent long-range interaction regime z_{lr} is then recorded within one single curve $\Delta f(z_{lr})/I_t(z_{lr})$ which is afterwards connected at each (x,y) - position of the site dependent data cuboid(s)^{III}.

In contrast, for the recording of $I_t(x, y, U)$ and $\Delta f(x, y, U)$ the acquisition time can only be tuned by choosing an appropriate bias interval. However, as already mentioned in case of STS this can be achieved by determining the bias voltages of interest within 1D spectra, while for the recording of $\Delta f(x, y, U)$ -data cuboids the voltage interval can be considerably shrunk by only regarding voltages close to the U_{LCPD} , which can as well be estimated

^{II}There are also cases, where a weak distance feedback is maintained [30]

^{III}For technical reasons, like the question of matching the two curves after the measurement, a small overlap in z between short and long range data is always desired.

from a 1D spectrum. Note, that for its determination the voltage interval ideally should be symmetrically distributed around U_{LCPD} which is important for the extraction of the angular point right after the measurement, which is obtained via a polynomial fit, and given by the maximum of the parabola. Note, that if the bias dependence is to be recorded, an additional weak distance dependence needs to be taken into account. For STS spectra the constant height set point needs to be chosen such that it corresponds to the tunneling regime. If only small bias voltage intervals are of interest, one can approach much closer, as if several volts need to be probed, because otherwise tip-crashes become rather likely due to the strong electric fields. On the other hand for the case of probing $\Delta f(x, y, U)$ the distance dependence is even more crucial. The closer the tip, the higher the sensitivity towards the short-range electrostatic forces, and thus, the sensitivity towards small charge variations and local dipole moments. To visualize the electrostatic properties and - potential variations, LCPD maps can be extracted from such data sets. Therefore, the angular point of the recorded parabola is extracted at each grid point and plotted over the whole grid.

2.3 Experimental Challenges

It is easy to imagine that the time needed to record a 3D spectroscopic data set drastically scales with the data density. The higher the desired resolution, the more data points are needed. In this manner, despite the possibilities used to shrink the measurement time, like discussed, data acquisition of up to 30 h were reported [30, 105]. On such time scales the measurements become constrained by several experimental difficulties which need to be thoroughly regarded in order to be able to successfully accomplish a measurement [159, 160].

Drift/creep and Piezo Nonlinearities

First of all, in a long term measurement thermal and electronic drift, as well as piezo creep and nonlinearities become limiting factors even if working at low temperature where most of the 3D spectroscopic data presented so far have been collected. Depending on the acquisition technique used, different methods have been proposed to overcome these, which will be explained by using the example of the collection of 3D $\Delta f(x, y, z)$ data.

In the layer-mode, drift and/or creep influences show up as lateral shifts of the contrast between the different layers. A commonly used post-processing method was advocated by Albers et al [30, 161, 162]. They acquired a 3D DFS data set on the basal plane of graphite by successively collecting images with slow feedback working at 5 K, so that thermal drift was strongly reduced. Before proceeding with the extraction of the interaction force and potential energy, lateral shifts of the observed atomic corrugation between different

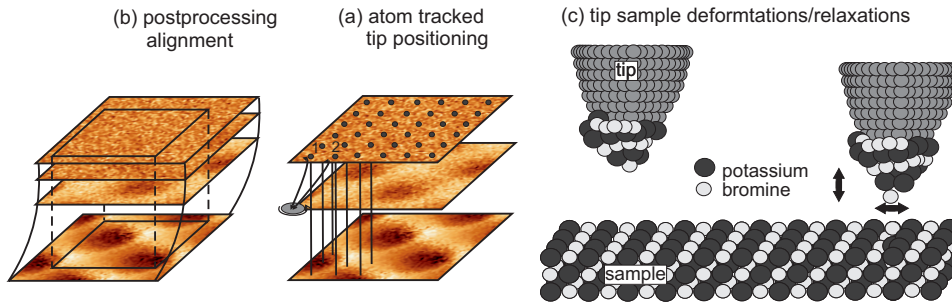


Figure 2.2: Reduction of drift and creep (a) in the grid-mode by atom tracking, and (b) in the layer-mode by applying a post processing alignment procedure. (c) Illustration of the tip-sample deformations/relaxations. Schematic drawing of an AFM model tip covered with an asymmetric cluster of sample material. At small tip-sample separations the tip apex can relax in z -direction as well as sideways.

layers were removed by first aligning characteristic features in successive layers. Subsequently, only that part which overlaps for all layers was kept for further data analysis [Fig. 2.2 (a)].

For data recorded using the grid-mode a different approach was employed by Kawai et al. [163], which relies on the atom-tracking-technique [see Fig. 2.2 (b)] [164–166]. They recorded a virtual drift free 3D DFS data set above NaCl(001) at room temperature. Before each single curve, (x, y, z) drifts were corrected by atom tracked tip positioning above a reference atom close to the predefined grid.

The Tip Apex

Contrast in STM and AFM is strongly dependent on the tip apex structure and chemical composition. There are more and less stable configuration, but actually, a particular configuration should not change at all (tip change) during an entire spectroscopy measurement. Thorough theoretical data analysis often requests to assume a tip model, so that supporting calculations about short range forces or of the LDOS become tip structure dependent as well. While metal tip apices can never be fully controlled, recent work pointed out that the possibility to obtain well defined tip apices by functionalizing them with small molecules or atoms [18, 28, 105]. Hereby, the choice of the molecule or atom triggers the tip's sensitivity to certain sample properties: for instance, carbon monoxide (CO) results in enhanced spatial resolution particularly for high resolution imaging [18], while xenon (Xe) increases the sensitivity towards the LDOS.

Tip Asymmetries and Elastic Tip-Sample Deformations

Especially at very small tip-sample separations the interaction forces can lead to overall relaxations of strongly interacting tip and/or surface atoms,

which in turn cause overall elastic deformations. The relaxations are only in special situations dominated by one single pair, e. g. in case of protruding dangling bonds at the tip apex and on semiconductor surfaces [115,152]. In case of soft samples like ionic crystals, which are presumably terminated by an asymmetric cluster of sample material [Fig. 2.2 (c)], and hence very soft, deformations most likely take place at the apex. [155,163].

In general, in the presence of asymmetric tip apices or tip-sample deformations/relaxations the overall shape of the observed atomic contrast is distorted. It depends on the magnitude of the asymmetry and on the strength of the interaction forces leading to the deformations, meaning that it increases with decreasing tip-sample separation. Two phenomena are distinguishable. First, the shape of the maxima/minima extracted from $z = \text{const}$ or $\Delta f = \text{const}$ slices close to the sample is distorted such that originally round and symmetric maxima and minima become oval close to the sample surface. In addition, the (x, y) -positions of the maxima or minima at different layers can be shifted laterally against each other [114,138,148,155,163,167], whereas the cluster asymmetry leads to a preferred deformation direction [Fig. 2.2 (c)]. This has a similar appearance as for the case of repeated image recording at the same place in the presence of uncompensated drift or creep.

The strongest impact of deformations can be expected for $\Delta f(x, y, z)$ because the probed z -regime usually contains repulsive interactions at closest recorded distance, while for $I_t(x, y, U)$ and $\Delta f(x, y, U)$ the distance regime usually stays in the attractive interaction regime. Furthermore, again the tip structure plays a dominant role. Principally, deformation influences are possible in these data sets as well.

2.4 Comparison of Grid- and Layer-Mode

It appears, that for data sets acquired in the layer-mode a difficulty in the interpretation of observed lateral pattern shifts might arise. Taking into account the above described possible appearances of drift/creep and deformation/relaxation influences, one finds that indeed both phenomena can give rise to lateral displacements of the observed patterns in subsequent layers. Thus, the assignment within a particular data set might be difficult.

Particularly, the post processing drift/creep alignment procedure used for data sets recorded with the layer-mode is based on the alignment of lateral pattern shifts. In this manner, it might be quite likely that shifts which are to be attributed to deformations are accidentally corrected as well. This in turn might afflict the data interpretation. In contrast, within the grid-mode, the data sets are already recorded in a drift free manner which is due to the utilization of the atom tracking function. Therefore, lateral pattern shifts can be distinctively assigned to deformations/relaxations.

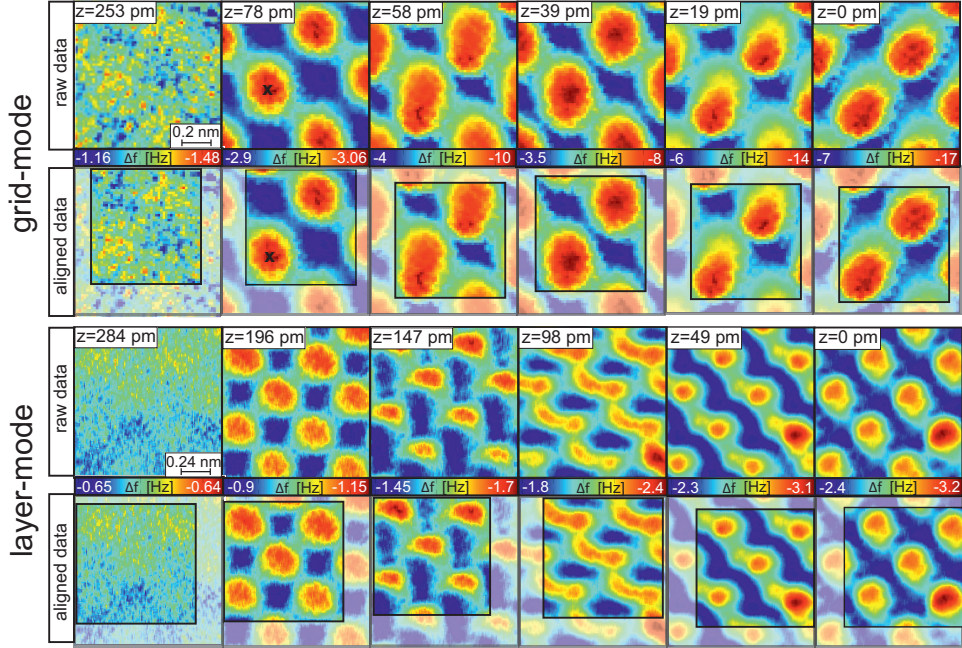


Figure 2.3: Constant height-maps $\Delta f(z = \text{const})$ of the grid- and layer-mode data, computed at different z . For each data set, both the raw- and aligned- data cuboids are shown. $z = 0$ corresponds to the closest recorded tip-sample separation. With decreasing z , the patterns shift laterally, and become furthermore distorted for certain layers. The crosses in the images at $z = 78$ nm mark the (x, y) -position at which the 1D curves in Fig. 2.6 were extracted. **Grid-mode parameters:** $T = 77$ K, $f_0 = 26.4$ kHz, $Q = 13481$, $A_{\text{osc}} = 500$ pm, $k = 1800$ N m $^{-1}$. **Layer-mode parameters:** $T = 4.8$ K, $f_0 = 24.8$ kHz, $Q = 9936$, $A_{\text{osc}} = 1.15$ nm, $k = 1800$ N m $^{-1}$.

This observation motivates to study the general impact of deformations on 3D spectroscopic data sets, which was done by using the example of 3D DFS measurements of $\Delta f(x, y, z)$ above the KBr(001) surface. Two data sets have been recorded: the first one was recorded with the grid mode at a microscope temperature of 77 K, resulting in a data cuboid consisting of $61 \times 61 \times 256$ data points covering a $1 \times 1 \times \text{nm}^2$ surface area. For the second one, the layer-mode was utilized at 4.8 K, resulting in $128 \times 128 \times 61$ data points above a $1.2 \times 1.2 \times \text{nm}^2$ area above the surface. For both modes, atom tracked tip positioning was utilized either between each two subsequent $\Delta f(z)$ - curves or $z = \text{const}$ images. This salvages a difference compared to the layer-mode acquisition procedure explained in the previous section. The correct working of the atom tracking based layer-mode method, however, is only ensured if the total drift/creep induced lateral shift during one image (appr. 3.5 minutes) is much smaller than the typical size of two adjacent maxima/minima. After estimating the drift/creep rate by recording a series of images at a tip-sample distance where no significant deformations are

expected, we had to decrease the microscope temperature down to 4.8 K to fulfill the requirement.

In this manner, two virtual drift free 3D data sets are available, which facilitates to deduce the influence of deformations on 3D spectroscopic data for both acquisition methods by evaluating the $\Delta f(x, y, z)$ -, $F_{\text{ver}}(x, y, z)$ -, $U_{\text{ts}}(x, y, z)$, and $F_{\text{lat}}(x, y, z)$ data cuboids. Furthermore, the consequences on the data interpretation by accidentally correcting deformation induced pattern shift with the post processing drift correction method were investigated. For this purpose, the two drift-free data sets were ‘deformation’-corrected with the post processing alignment procedure on purpose. For the resulting slightly smaller deformation corrected data cuboids, the force and potential energy extractions were carried out as well, and the results were compared to those extracted from the original data.

2.4.1 Frequency Shift Maps

Figure 2.3 shows a series of six constant-height maps of $\Delta f(z = \text{const})$ generated from the data cuboids of the grid-mode dataset at several tip-sample separations z . The upper row shows the original data, while in the lower row the data cuboids remaining after post processing alignment are displayed together with the original data in order to make their location within the latter visible. The influences of overall deformations and of generated atomic relaxations during the measurement become clearly visible. With decreasing z the atomic corrugation between adjacent layers shifts against each other. Furthermore, the shape of the contours in several layers is strongly distorted, as for instance in the image recorded at $z = 58$ nm. These observations are in good agreement to the expectations of such distortions for ionic crystals. The data recorded with the layer-mode, shown in Fig. 2.3, feature a similar appearance. Again, the overall deformations manifest as lateral shifts between adjacent layers as well as in strong distortions of the observed patterns. The impact is much stronger than for the grid-mode data, as can be seen for instance in the image recorded at $z = 98$ nm. The lateral pattern shifts within the two data sets are compared in Fig. 2.4 by means of the respective $x(z)$ - and $y(z)$ - trajectories of the tip when approaching towards the sample surface. They reflect the strength and direction of the present deformations and relaxations.

Due to features like the oval shapes of the distorted patterns in several horizontal slices, which introduce some uncertainty, the maxima in different (x, y) - cuts could not be perfectly aligned one below the other. However, for a consistent approach, their centers, which are the locations of most negative frequency shift, were determined, and used for the alignment. Altogether, the strength of deformations concerning the lateral pattern shift as well as the distortions observed for the layer-mode data exceeds that seen in the grid-mode data by far.

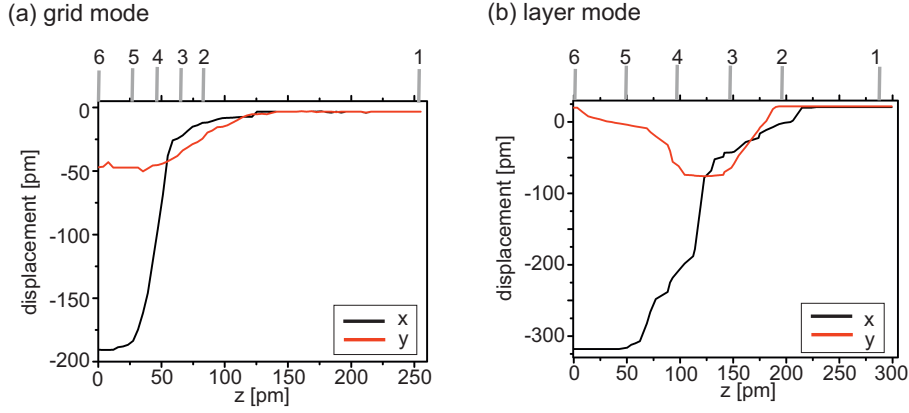


Figure 2.4: Tip trajectory $x(z)$ and $y(z)$ of the tip for approaching the sample surface for (a) the grid-mode, and (b) the layer-mode dataset [Fig. 2.3]. The indications (1)-(6) marked in the respective curves refer to the extracted constant-height maps (a-f) of the datasets shown in Fig. 2.3.

2.4.2 Interaction Force and Potential Energy

For a further investigation of the influence of deformations before and after the post processing alignment, $F_{\text{ver}}(x, y, z)$ -, $U_{\text{ts}}(x, y, z)$ - and $F_{\text{lat}}(x, y, z)$ -maps of both the raw and the aligned dataset need to be quantitatively compared. Starting with the grid-mode data presented in Fig. 2.5 (a-f), the patterns of the vertical interaction force maps F_{ver} in (a) and (d) exemplarily extracted for $z = 43$ nm dramatically differ from each other. In order to clarify these observations, 1D curves extracted at the pattern center of the raw and aligned data are shown in Fig. 2.6 (a). They reveal, that the post processing alignment has increased the magnitude of $F_{\text{ver}}(z)$ at short distances. A similar phenomena was observed in the potential energy maps [Fig. 2.5 (b) and (e)]. Therefore, the patterns in the aligned data set appear less noisy, and hence, at first sight more appealing compared to the raw data. But, by looking at the corresponding 1D curves [Fig. 2.6 (b)], it becomes visible, that the alignment has also led to a larger magnitude of $U_{\text{ts}}(z)$.

Generally, the alignment procedure reduces the lateral shifts of the contrast, so that maxima and also minima positions stay constant for any z . This leads to the larger magnitude of attractive $F_{\text{ver}}(x, y, z)$ at small tip-sample separations within the aligned data cuboid, as exemplarily shown in Fig. 2.6. Consequently, also the contrast of $F_{\text{ver}}(x, y, z)$ as well as that of $U_{\text{ts}}(x, y, z)$ (being the result of integrating in z -direction) becomes stronger. However, the corrugation of the aligned F_{ver} - and U_{ts} -maps are strongly distorted still, which is due to the fact that the alignment procedure suppresses the physically deformation induced distortions of the atomic contrast.

The fact, that the alignment procedure has *artificially* increased the signal-

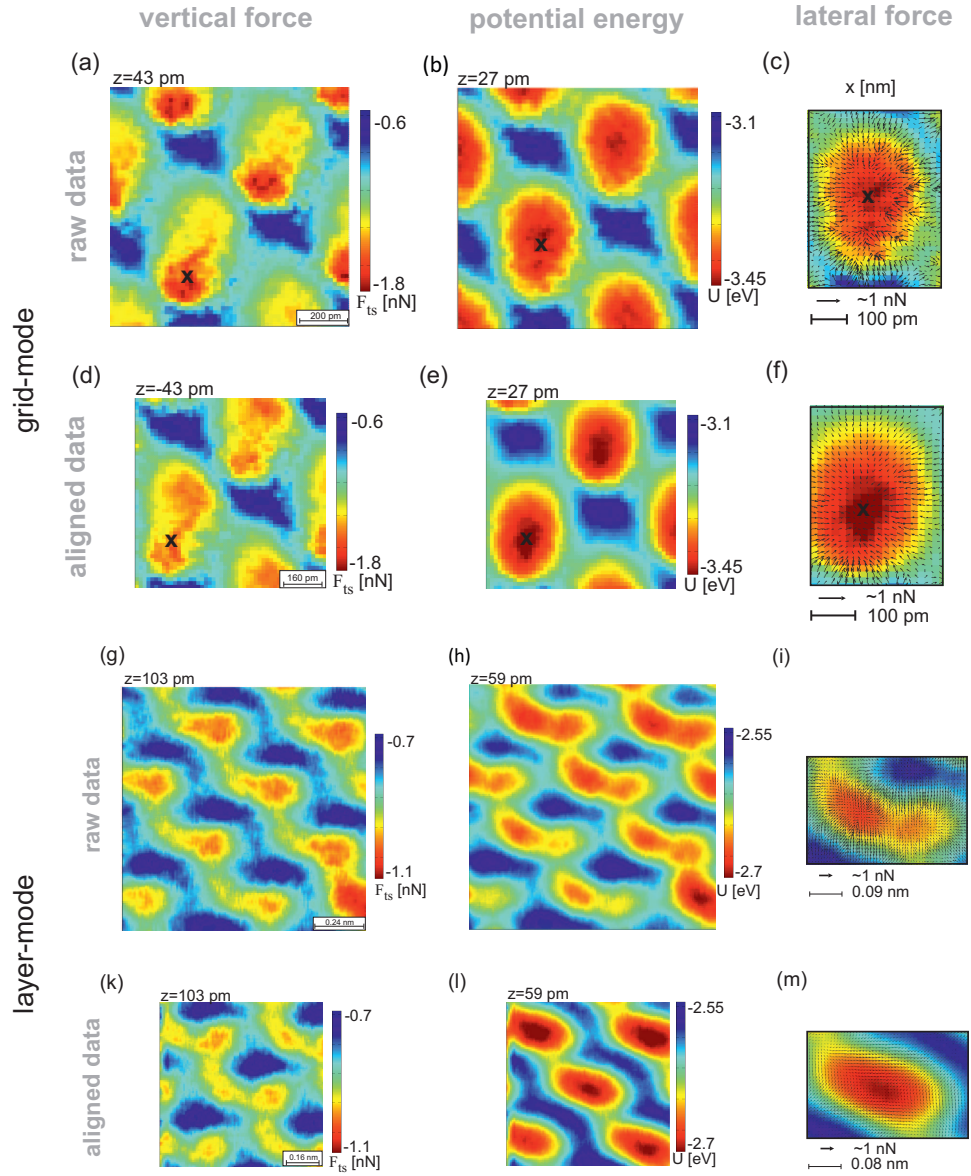


Figure 2.5: Force and potential energy extractions of the grid- (a-f) and layer mode data (g-m) of both the raw and artificially aligned data. Shown are constant height maps of the vertical interaction force $F_{\text{ver}}(x, y, z)$ ((a), (c), (g), (k)), potential energy $U_{\text{ts}}(x, y, z)$ ((b), (e), (h), (l)), and lateral force fields $F_{\text{lat}}(x, y, z)$, superimposed on the corresponding pattern in the $U_{\text{ts}}(x, y, z)$ - maps ((c), (f), (i), (m)). The crosses marked in the images taken from the grid mode data indicate the (x, y) -positions at which the 1D-curves of Fig. 2.6 were extracted.

to-noise ratio of $U_{\text{ts}}(x, y, z)$, also strongly influences the calculated lateral forces, indicated with arrows in Fig. 2.5 (c) and (f). Since the $U_{\text{ts}}(z = \text{const})$ -maps of the aligned data have a higher signal-to-noise ratio, the lateral force

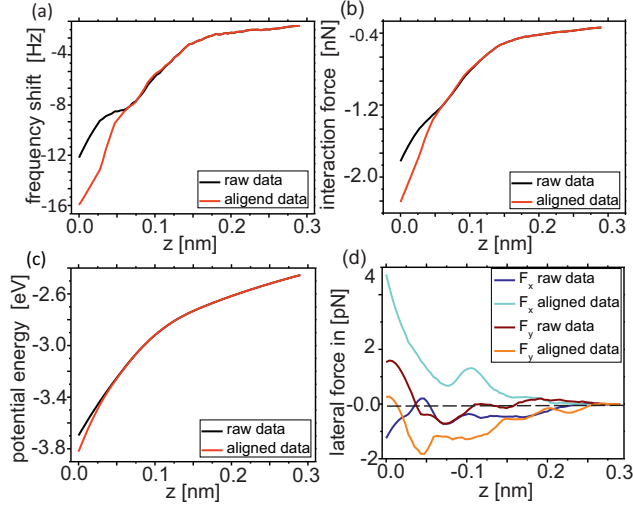


Figure 2.6: 1D curves of the grid mode data set, extracted above the atomic site marked with crosses in Figs. 2.3 and 2.5. (a) $\Delta f(z)$, (b) $F_{\text{ver}}(z)$, (c) $U(z)$, (d) $F_x(z)$ being the lateral force component in x -direction, and $F_y(z)$ the one in y -direction.

map extracted from the aligned data is also less noisy. However, it does not match theoretical considerations from which the lateral force components are expected to vanish at maxima and minima. The raw dataset features tiny lateral force components even above maxima and minima which are likely due to uncertainties in their precise location. After aligning these, components become generally stronger and above the maxima and minima locations very systematically zero, proving that the procedure was unable to fully remove deformation effects. Furthermore, by comparing the lateral force of the raw and aligned data at a certain site, it becomes visible that even the sign of the lateral force component can change after aligning [Fig. 2.6 (d)].

The force and potential energy extractions for the layer-mode data are depicted in Fig. 2.5 (g-m). Analysis of these data leads to qualitatively similar results compared to the grid-mode data. The patterns observed in the interaction force maps [Figs. 2.5 (g) and (k)] strongly differ from each other, while the potential energy and lateral force maps of the aligned data [Fig. 2.5 (h) and (i)] are less noisy compared to those extracted from the raw data [Fig. 2.5 (l) and (m)]. Also, the alignment procedure has increased the absolute values of F_{ver} - and U_{ts} - maps at small z [not shown], and the lateral force maps show the same peculiar behaviour than observed for the grid-mode data.

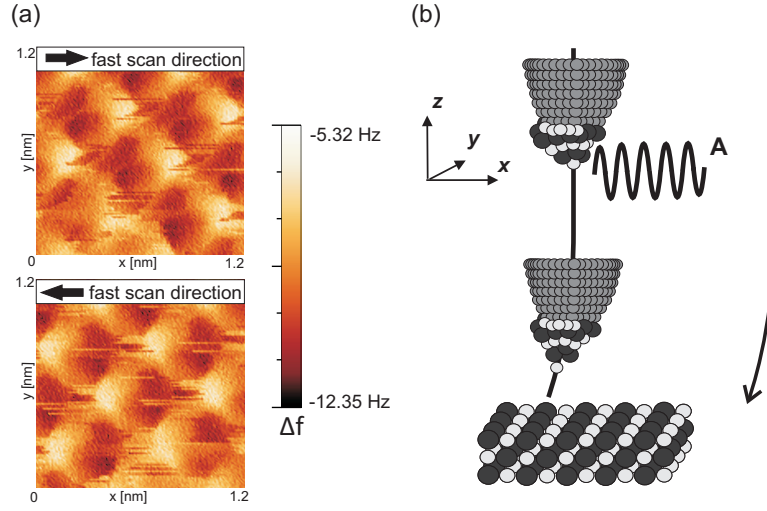


Figure 2.7: Influences of the oscillation amplitude. (a) Forward and backward scans at the closest recorded tip-sample distance from a layer-mode 3D DFS data set recorded with an oscillation amplitude of 500 pm. Left-right asymmetries like those seen in friction force microscopy as well as scanning artifacts are visible. (b) A tip terminated by an asymmetric cluster of sample material is approached towards the surface. Deformations cause relaxations in x -, y - and z - directions. The trajectory is time averaged over the oscillation cycle and hence never known exactly.

2.4.3 Performance of Grid- and Layer-Mode

For a qualitative comparison of the performance of grid- and layer-mode several aspects have to be taken into account:

Tip influences At the closest recorded tip-sample separations recorded for the two data sets, the appearance of the maxima and minima strongly differ from each other although principally the same phenomena were observed. This can be seen for instance by comparing the constant height maps of $\Delta f(x, y, z = 58 \text{ nm})$ for the grid-mode data and $\Delta f(x, y, z = 98 \text{ nm})$ for the layer-mode data. The fact that they were not recorded with the same tip leads to the conclusion that the observed contrast distortions are strongly tip dependent. Furthermore, since the lateral shift of the patterns over the recorded z range accounts to 0.2 nm and 0.3 nm for the grid- and layer data respectively, which corresponds to about $\frac{1}{2}a_{KBr}$, the observed deformation induced shifts not only involve the front most tip atom [167], but also further atoms of a small cluster at the apex [155].

Energy dissipation While no site specific contrast in the energy dissipation maps E_{diss} was observed for the layer-mode data set, a weak atomic corrugation at the closest distances is found for the grid-mode data [2.4-

4.2 meV/cycle] (maps not shown). This finding is in good agreement with the fact that E_{ts} is sensitive to tip rearrangements [148,168] which more often take place at higher temperature [113]. However, a more detailed comparison of the dissipation phenomena of the two data set is hindered, because they are too different from each other (acquired with different A_{osc} , at different temperatures, and with different tips).

Oscillation amplitude Whereas a main advantage of tuning fork operation lies in the utilization of small oscillation amplitudes, those employed here are rather large (500 pm for the grid-mode and 1.15 nm for the layer-mode). Particularly, for the layer-mode data set the reason lies in lateral instabilities at small z : These are due to infrequently formed contact junctions that are not ruptured during many oscillations [163] provoked by stronger lateral and hence also adhesive forces. This is illustrated in Fig. 2.7 (a) showing the closest recorded forward- and backward-scan of a layer-mode data set recorded with $A_{osc} = 500$ pm. Stick-slip like pattern distortions and streaks are visible associated with tip changes which are caused by strong lateral deformations and jumps like those observed in contact-mode Friction Force Microscopy [169]. These scanning artifacts can have additional influences on $F_{ver}(x, y, z)$, $U_{ts}(x, y, z)$ and $F_{lat}(x, y, z)$.

The dependence of Δf from F_{ver} according to Eq. 1.25 furthermore implies, that only the time-averaged tip-sample distance is measurable *via* $\Delta f(z)$ at a finite amplitude [154]. Because the measured data are time averaged [see Fig. 2.7 (b)], the instantaneous tip apex position as a function of distance can never be exactly estimated. This prevents the determination of the actual origin of deformations from frequency shift maps. In principle, this finding also generally prevents the exact compensation of interaction-induced deformations by post processing methods.

Force and potential energy extraction The lateral pattern shifts plotted as a function of z as shown in Fig. 2.4 indicate the magnitude of the deformations induced upon approach. For the layer-mode data, where the fast data acquisition direction is parallel to the surface, those shifts evolve on a much slower timescale than for grid-mode data, where the measurement first proceeds in z -direction at a certain point (x, y) . Accordingly, this leads to an inferior time correlation between two neighboring data points in z upon the $F_{ver}(x, y, z)$ and $U_{ts}(x, y, z)$ extractions.

For both acquisition methods, the influence of deformations appears via distortions of the patterns as well as a lateral shift of the pattern location between adjacent constant height slices. Extracted vertical and lateral interaction force and potential energy fields are affected by the deformations as

well. Generally, the actual shape of the distorted contrast is strongly tip dependent, and the magnitude of observed deformations furthermore depends on the oscillation amplitude.

The post processing alignment of lateral pattern shifts due to deformations can produce strong artifacts. Moreover, due to the finite oscillation amplitude leading to a time-averaged Δf - signal the shifts can never be fully compensated. The same holds for the pattern distortions which are not regarded by this method at all. In this manner, if working with the layer-mode, the actual origin of lateral pattern shifts needs to be carefully tested before any alignment is performed. Alternatively, one can perform drift corrections *a priori* by utilizing atom tracked tip positioning, like in the present case. This method turned out to be much more reliable to target the influences of long term drift and/or creep, even if the recording of data layer by layer might be accomplishable faster. Nevertheless, due to the better time correlation in z and due to the fact that the influences of deformations and scanning artifacts for a certain amplitude are smaller within grid-mode operation suggests the the grid-mode might to be preferred, at least for soft samples.

2.5 Summary

In summary, the prospects and challenges of 3D spectroscopy, representing the most dense data collection, were thoroughly discussed for the grid- and layer- data acquisition modes. Influences of long term drift or creep can be successfully ruled out by the utilization of atom tracked tip positioning, so that long term data collection becomes possible even at room temperature [163]. On the other hand, influences due to tip-sample deformations and relaxations cannot be fully circumvented, which originates from the averaging effect mediated by the oscillation amplitude. Altogether, the influence of deformations for a certain oscillation amplitude is stronger for layer-mode data which is due to the lateral movement of the tip. Since furthermore the time correlation in z direction for the latter is lower, the grid-mode might be preferable, particularly for z dependent spectroscopy measurements, which are usually to be probed up to the repulsive force interaction regime, so that deformations might have a dominant role.

Concerning $I_t(x, y, U)$ spectroscopy measurements, deformations become less significant, as usually larger tip-sample separations are sufficient. Finally, for $\Delta f(x, y, U)$ data, where the detection of short-range interaction forces is desired in order to probe local electrostatic properties, again deformations might become present, so that again the grid-mode might be preferable. This means, that at each point of a predefined grid, one parabola $\Delta f(x, y, U)$ is recorded.

Chapter 3

Experimental

The following chapter is dedicated to experimental issues. Besides the equipment and sample preparation procedures used, a whole section will be dedicated towards the handling of molecules. Molecules designed for molecular electronics applications, are often rather complex due to special functionalizations, so that several challenges can arise.

3.1 The UHV System

The UHV system utilized for all experiments, an Omicron^I low temperature (LT) ultra high vacuum (UHV) - AFM/STM, is depicted in Fig. 3.1 (a). The UHV system mainly consists of two chambers, the preparation (P) and analysis (A) chamber, both operating at a base pressure of 10×10^{-10} mbar to 10×10^{-11} mbar.

The P-chamber exhibits several standard tools for surface preparation: an ion bombardment gun operated with Ar⁺ ions, an evaporator with three Knudsen cells for molecule depositions, a quartz crystal micro balance (QMB) to monitor deposition rates, a quadrupole mass spectrometer (QMS), which detects masses up to 300 u, an evaporator with three crucibles for metal deposition, and a load lock used to introduce samples and force sensors. The central manipulator used for transfers between the two chambers is equipped with an electron-beam heating stage, and a cooling facility for either liquid nitrogen, or helium operation, resulting in substrate temperatures of $T_{N_2} \approx 130$ K and $T_{He_2} \approx 80$ K respectively.

One particular draw back of this substrate cooling possibility concerns the fact, that upon the transfer into the microscope the samples need to be manipulated with a wobble stick kept at room temperature. For this reason, the effect of cooling with helium instead of nitrogen practically becomes negligible. Moreover, the cooling temperatures accessible are in most case

^IOmicron Nanotechnology GmbH (www.omicron.de), now belonging to Oxford Instruments (www.oxford-instruments.com).

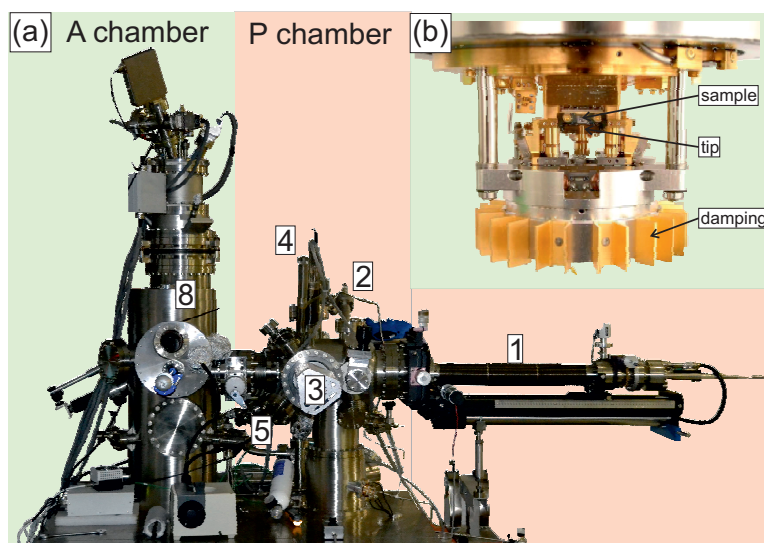


Figure 3.1: (a) Omicron LT-STM/AFM. The microscope is placed in the A-chamber. The P-chamber exhibits several units for sample preparation, marked by numbers, and described in the main text: (1) Manipulator with heater and cooling stage, (2) ion bombardment gun, (3) QMS, (4) QMB, (5) molecule evaporator, (6) (not visible) load lock, (7) (not visible) metal evaporator, (8) cryostat. (b) View into the sample stage of the microscope, provided by Omicron Nanotechnology GmbH.

not sufficient for obtaining single molecules on insulating surfaces just after deposition [see Chap. 6].

The A chamber incorporates a sample stock and the microscope, which is illustrated separately in Fig. 3.1 (b). The sample is mounted overhead, and the probe sensor (either a pure STM tip or a tuning fork sensor) can be moved in all three dimensions. An eddy current damping system provides vibration insulation. Bias voltages are always applied to the tip with respect to the sample. For data acquisition the Nanonis SPM control system^{II} was used, coming with an internal lock-in amplifier, an OC4 PLL (phase locked loop SC4/RC4), and the AT4 unit for atom tracking [164]. Data processing was performed with WSxM [170] and Matlab^{III}.

3.2 Characteristics of the Omicron *qPlus* Sensor

An image of a *qPlus* probe sensor from Omicron is depicted in Fig. 3.1 (a). The set up is in accordance to the propositions by Giessibl [25] with one fixed prong. The tuning forks exhibit a beam length of $L \approx 2.4$ mm, a thickness of $t \approx 214$ μm , and a width of $w \approx 130$ μm . The calculated spring constant

^{II}SPECS Zurich GmbH, www.specs-zurich.com.

^{III}MathWorks, www.mathworks.de.

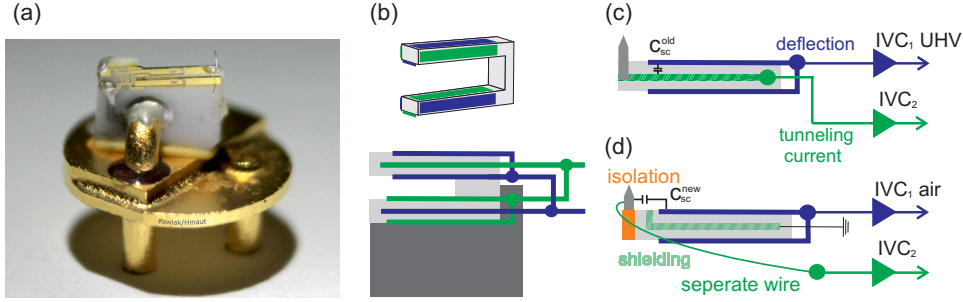


Figure 3.2: The *qPlus* force sensors (a) Omicron *qPlus* force sensor. (b) Schematic of the gold electrodes and the contacting of a tuning fork. (c,d) Signal read out and wiring in the old and Omicron *qPlus* sensors.

accounts to $k = 1800 \text{ N/m}$. Suggestions to experimentally determine the actual spring constant are summarized in [171]. An etched tungsten tip is glued to the free prong. For this reason the resonance frequency is typically in the range of $f_0 = 15 \text{ kHz to } 30 \text{ kHz}$.

The full signal read out and tuning fork excitation is accomplished via two contacts, which is illustrated in Fig. 3.1 (b). For the *qPlus* sensors from Omicron, originally, the two tuning fork electrodes at the surfaces of the free prong were used, whereas one of them was connected to the deflection amplifier while the other was used to detect the tunneling current, like depicted in Fig. 3.2 (c). In this setup, however, the tunneling current travels through the whole fork, which likely leads to an artificial signal within the deflection channel, particularly if high tunneling currents are involved. The origin of this signal is given by capacitive cross coupling mediated by the stray capacitance C_{sc}^{old} between the two channels. One possible origin concerns the speed limits within the current- to- voltage (IVC) converters and was intensively discussed in [172].

The cross coupling became considerably reduced in the new setup, which is depicted in Fig. 3.2 (d). The electrode originally used for the tunneling current detection becomes grounded and hence, serves as shielding between tunneling current- and deflection channel. The tip is furthermore isolated from the prong, and the tunneling current is detected via a separate wire [172], so that one obtains $C_{sc}^{new} \ll C_{sc}^{old}$.

Most measurements of this thesis were recorded by a tuning fork in the old setup. If simultaneously to the deflection recording tunneling currents were detected, care had to be taken upon signal interpretation. In order to avoid cross talk effects the bias voltage was always tuned to a few μV during simultaneous spectroscopic operation. However, this is not possible for bias spectroscopy measurements, where the bias needs to be ramped. Here, the tunneling current was limited to about 100 pA to minimize the influences of cross talk [see also appendix A]. For the measurements acquired with the

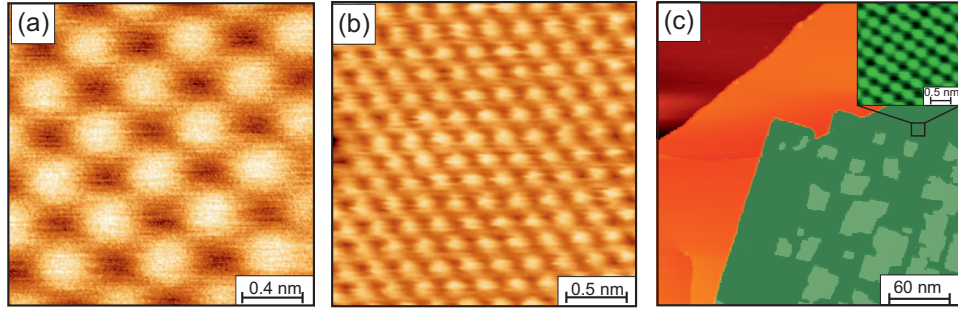


Figure 3.3: Utilized surfaces. (a) KBr(001), (b) Cu(111), and (c) NaCl/Cu(111), whereas NaCl areas are colored in green. **Parameters:** (a): $\Delta f = -2.2$ Hz, $f_0 = 26.4$ kHz, $U_{\text{bias}} \approx 0$ V, $A_{\text{osc}} = 250$ pm, (b): $\Delta f = 34$ Hz, $f_0 = 26.4$ kHz, $U_{\text{bias}} = -110$ V, $A_{\text{osc}} = 200$ pm, (c) $U_{\text{bias}} = 2$ V, $I_t = 50$ pA, inset: $U_{\text{bias}} = -1.8$ V, $I_t = 500$ pA.

new setup, tunneling currents up to the range of $I_t \approx 1$ nA can be detected without any measurable coupling of the two signals, which is a considerable improvement.

Another possible artificial contribution towards the frequency shift signal is not attributed to the tuning fork wiring. It is caused by the so called phantom force, which originates from a sample resistivity [173, 174], and is particularly present on semiconducting surfaces.

In order to prepare the tip apex, the tip was repeatedly softly indented into the Cu(111) surface via z-spectroscopy curves, so that the tunneling current detection saturated. Furthermore, the tip was treated with bias voltage pulses of up to $U_{\text{bias}} \pm 10$ V. Consequently, it is assumed, that the apex is covered by a small cluster of copper atoms.

3.3 Substrate Preparation

KBr(001)

Potassium bromide (KBr), grown in the (001)- direction, is an ionic crystal with a cubic-face-centered (fcc) lattice with two atomic base, and a lattice constant of $a = 6.60$ Å [175]. Bulk KBr crystals were purchased from MaTecK^{IV}, cleaved in air with a razor blade, immediately introduced to the UHV chamber, and heated up to $T \approx 670$ K for several hours in order to remove contaminants like for instance water, and residual charges.

An atomically resolved image is shown in Fig. 3.3 (a). The contrast is frequently explained by the contribution of short-range electrostatic interaction forces. Accordingly, maxima in an nc-AFM image refer to only one species, either K^+ or Br^- . Which of these appears bright depends on the charge and chemical sensitivity of the tip [114].

^{IV}MaTecK GmbH, www.mateck.de

Cu(111)

Within the group of (semi-) noble metals, copper (Cu) (work function for the (111) growth direction: $\Phi_{\text{Cu}} = 4.94 \text{ eV}$ [176]) exhibits the strongest reactivity. It crystallizes in a cubic face-centered lattice with one atomic basis and lattice constant $a = 3.61 \text{ \AA}$ [175]. Crystals in the desired orientation were purchased from MaTeck. Atomically clean surfaces were prepared by several cycles of repeated Ar^+ - ion sputtering ($p \approx 3 \times 10^{-6} \text{ mbar}$, $E = 0.8 \text{ keV}$ to 1.2 keV) and subsequent annealing ($T \approx 770 \text{ K}$).

A constant frequency shift image is shown in Fig. 3.3 (b). Large scale STM images at certain bias voltages recorded at low temperature, frequently feature the appearance of wave patterns on the substrate, which are attributed towards the well known Shockley type surface state [126,177,178] exhibiting a two-dimensional nearly free electron gas behavior.

Ag(111)

Silver (Ag) (work function $\text{Ag}(111)$ $\Phi_{\text{Ag}} = 4.46 \text{ eV}$ [179]) crystallizes in a cubic face-centered lattice with one atomic basis, whereas the lattice constant accounts to $a = 4.09 \text{ \AA}$ [175]. The crystals were purchased from MaTeck as well, and preparation of $\text{Ag}(111)$ was carried out similar to the case of $\text{Cu}(111)$, differing only by the annealing temperature of $T \approx 720 \text{ K}$.

NaCl on Cu(111)

Sodium chloride (NaCl) was deposited on the $\text{Cu}(111)$ surface by thermal evaporation. Heating the crucibles up to 758 K corresponded to a deposition rate of $0.25 \text{ \AA min}^{-1}$ to which the samples were exposed for $t \approx 8 \text{ min}$. If the substrate temperature (T_{sa}) during deposition stays at room temperature (RT) or slightly elevated temperatures the resulting films start to grow with double layer islands, exhibiting a perfect rectangular shape along the substrate $[100]$ - directions and grow in the so called carpet mode, as can be seen in Fig. 3.3 (c)^V. The island diameter increases with the substrate temperature during deposition and can range up to the micrometer range. On top of the double layer islands, smaller rectangular islands are formed of third and eventually also fourth ML [144]. An atomically resolved image of a typical thin NaCl film is depicted in the inset of Fig. 3.3 (c).

^VMonolayer islands can only be formed if deposition is carried out onto cooled substrates.

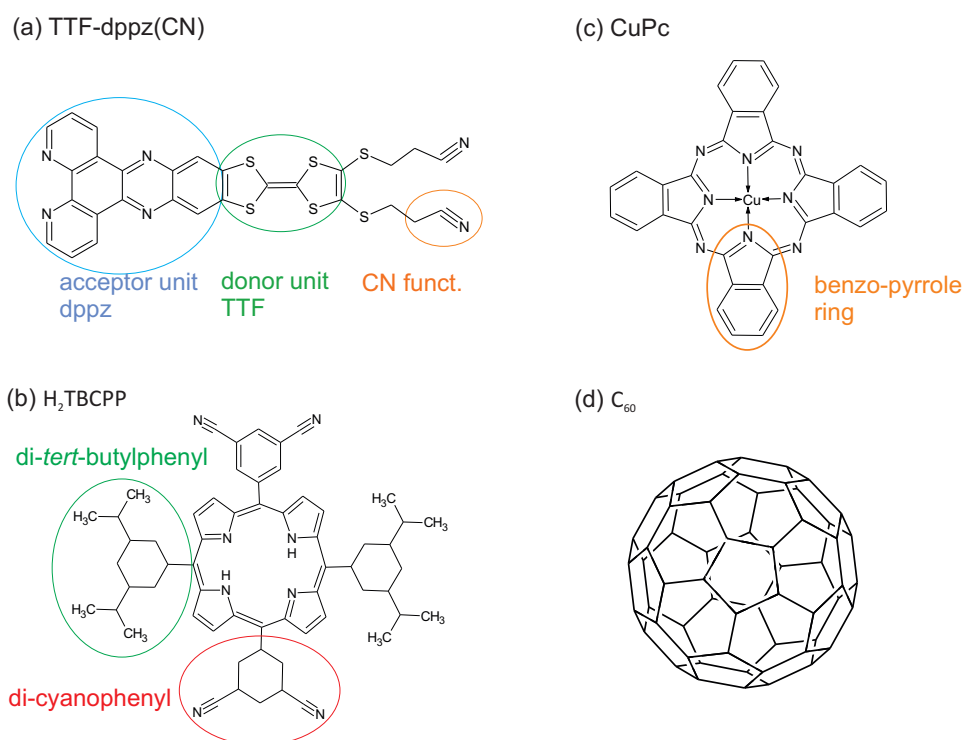


Figure 3.4: Utilized molecules. (a) TTF-dppz, (b) H₂TBPP, (c) CuPc, (d) C₆₀. For details see the main text.

3.4 Molecules

3.4.1 Utilized Molecules

All molecules used in this thesis feature a strong aromatic character [see Sec. 4.1]. Of particular interest to this thesis are the classes of the structurally very similar porphyrins and phthalocyanines (phthalocyanine (Pc)), which belong to the most intensely studied classes of organic compounds [26], particularly within the field of organic based electronics. Both are pyrrole based, and actually, the systematical chemical name of phthalocyanine is given by tetrabenzotetraazaporphyrine. Furthermore appealing is the fact, that the electronic properties are widely tunable by coordination of various metals into the core without modifications of the molecular bodies by additional functional groups, so that the main structure can be sustained.

In the following each structure will be introduced. All have been deposited by means of thermal evaporation from a Knudsen cell, whereas for the TTF-dppz problems occurred [see Sec. 3.4.4]. The used sublimation temperatures and rates are summarized in Tab. 3.1.

Table 3.1: Sublimation temperatures and deposition rates of the utilized molecules.

Molecule	sublimation temp.	deposition rate
TTF-dppz	446 K	0.07 Å min ⁻¹
H ₂ TBCPP	535 K	0.2 Å min ⁻¹
CuPc	583 K	0.29 Å min ⁻¹
C ₆₀	633 K	0.22 Å min ⁻¹

TTF-dppz(CN)

The tetrathiafulvalene fused dipyridophenazine complex (TTF-dppz(CN)) [180], a Donor-Acceptor molecule, is depicted in Fig. 3.4.1 (a). It consists of two subunits, the dipyridophenazine (dppz) core, which acts as an electron acceptor and the tetrathiafulvalene (TTF) core as an electron donor. The molecule is functionalized with cyano phenyl (CN) end groups [see below]. The lowest energy excited state of TTF-dppz(CN) corresponds to an intramolecular charge transfer (CT) from the TTF to the dppz (HOMO-LUMO excitation).

H₂TBCPP

H₂TBCPP is a free-base core porphyrin. Its chemical structure is depicted in Fig. 3.4.1 (b). The base is functionalized with two *meso*-(3,5-dicyanophenyl) [see below] and two *meso*-(3,5-di-*tert*-butylphenyl) groups which are marked by a green and respectively red circle. The name porphyrin originates from the greek word for purple. Many members of the class occur in nature, like for instance „heme“, which is part of hemoglobin, the red pigment in blood cells, but also by chlorophyll, the centerpiece of photosynthesis. On this basis, in combination with the utmost chemical and temperature stability, the enormous effort done to investigate the properties of various porphyrin based compounds on surfaces, as well as the trials to incorporate them into organic based devices becomes understandable. For an overview the reader is referred to [181].

When coming to molecular electronics, also some of the general fundamental questions were targeted by using porphyrin molecules. For instance, the arrangement of molecules on insulating electronically decoupling surfaces, were addressed by nc-AFM. On the ionic crystal KBr(001), the molecules self assemble into molecular wires [182, 183] with the appealing property of self-healing after destruction by the scanning tip [92]. Also the contacting by metal electrodes was shown to be possible [184, 185]. Finally, a porphyrin based molecular switch was presented, based on the rotation of a side group of the molecule [139].

CuPc

CuPc, which due to its intense blue color is also called Monastral blue, was first developed as a pigment in the 1930s [186]. Its chemical structure ($C_{32}H_{18}N_8Cu$) is depicted in Fig. 3.4.1 (c). The central Cu atom is surrounded by four benzo pyrrole rings that are bridged by four N atoms yielding in a D_{4h} - symmetry. It exhibits p-type semiconducting behavior with a band gap of $E_g = 1.7$ eV and an adsorption coefficient $\alpha = 10 \times 10^5$ cm⁻¹ [187]. The π - orbitals of CuPc are widely delocalized, and stick out of the molecular plane. Consequently, strong molecule-surface interactions can be expected particularly on metal substrates.

Remarkable success was gained for the integration of various phthalocyanines (PC) into organic based devices [22, 188], many of them also have been regarded on surfaces [189]. Particularly for CuPc, numerous reports are available [134, 190–201]. Besides these SPM based investigations, however, also their opto-electronic properties were targeted by incorporating them into various organic based devices [19] ranging from organic field effect transistors (OFETS) [202, 203] over organic light emitting diodes (OLEDs) [204, 205] to organic solar cells [206, 207] [for the latter see also appendix A].

C₆₀

C₆₀, the so called buckyball structure is maybe the most famous fullerene representative. Its spherical chemical structure is depicted in Fig. 3.4.1 (d). It is highly sp₂ hybridized, and a very stable compound as will be discussed in Sec. 4.1. Its discovery [208] was even rewarded with the nobel prize in 1996.

CN Functionalization

Carbonitrile (CN) groups are frequently used for functionalization of molecules for on-surface investigations. First of all, it allows for organometallic complexation [209]. The associated strong dipole moment carbonitrile group (CN) groups also strongly enhances the adsorption energies, resulting in a higher stability of the adsorption site on insulating surfaces [183, 184, 210–212], as well as on metals for enhanced charge transfer [213, 214].

3.4.2 Deposition

Mostly, molecules are deposited by **thermal evaporation** from a Knudsen cell in order to condensate them on a specific surface. Those molecule relevant for molecular electronics applications are often rather complex, due to various functionalizations in order to incorporate specific functionalities. Since the sublimation temperatures roughly scale with the size and

weight of the molecular compounds, unwanted fragmentation becomes more likely [215].

This problem can possibly be avoided by applying an alternative deposition method, the **Molecular Spray Technique** [216–218]. It is based on **Electro Spray Ionization** (ESI) [219] known to be the most gentle technique to ionize large fragile molecules from solution. However, the experimental setups and their handlings are in most cases much more complicated as for thermal evaporation [220, 221]. The molecules are sprayed together with solvents and thus either sufficient mass filters are needed, or it has to be carefully proven for each studied system which morphology could be unambiguously attributed to the molecules under investigation.

Generally for an evaporation procedure, also the purity of the powder (ideally $> 99.5\%$) is of utmost importance. Already a very small percentage of contaminants, for instance due to the solvent matrix, can lead to their deposition instead of proper molecules. If not detected, such co-depositions might evoke difficulties in the interpretation of the obtained surface morphologies. In this manner, it is advantageous to purify the powders prior to measurements [see Sec. 3.4.3].

The deposition process might be controlled by either a QMB or QMS. For both cases there are pros and cons. A QMB does not exhibit mass selectivity, and thus only detects that „something“ is evaporated with a certain rate. It can not explore whether mainly impurities or only molecular fragments might be sublimed. This can be circumvented by implementing a QMS. But, depending on the filament current, this method in turn eventually more likely can lead to fragmentation of the molecules upon ionization, which again can tamper the analysis of the deposition process.

3.4.3 Sublimation Testing Unit

Only by its chemical structure it is not obvious whether a molecule can be sublimed or not. For this reason a sublimation testing unit was built-up for the purpose of testing the temperature stability of new (noncommercial) molecules prior to SPM experiments. Its setup, depicted in Fig. 3.5, is similar to the one described in [222].

The molecules are deposited from the bottom of a glass tube which can be vacuumized ($p < 10 \times 10^{-6}$ mbar). Sublimed molecules are captured on a cooling finger [see inset of Fig. 3.5] which exhibits connections for cooling water if desired. The heating is carried out by either utilizing a water- or metal bath (Roses metal: 50% bismuth, 25-28% lead, 22-25% tin, melting point $T_{\text{melt}} = 367\text{K to } 371\text{K}$).

For an analysis of the sublimation process, the sublimated molecules are washed from the cooling finger by using an appropriate solvent, and analyzed with ESI and subsequent mass spectrometry in the Chemical Department (Bruker ESI Esquire). For comparison, the initial molecules and the

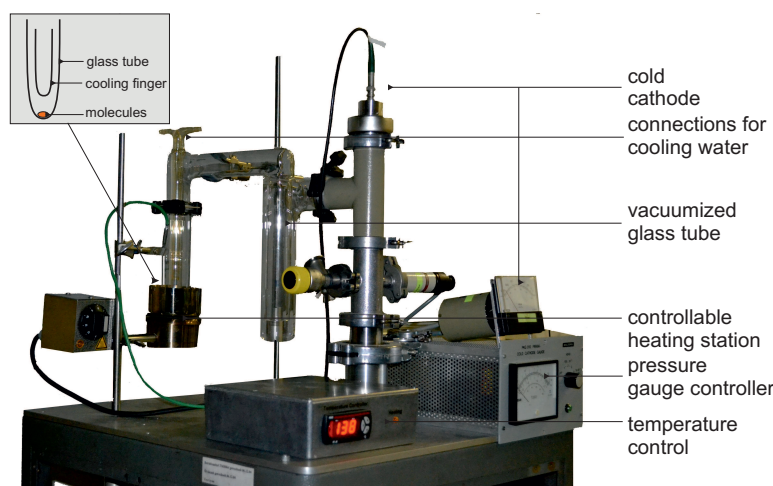


Figure 3.5: The sublimation testing unit. Molecules are sublimed in high-vacuum conditions ($p < 10 \times 10^{-6}$ mbar) and are captured on a cooling finger (inset) for subsequent analysis.

substance remaining at the bottom of the crucible can be analyzed as well. In addition, the sublimation test-unit can be utilized to purify molecules from contaminants by annealing for several hours slightly below the (expected) sublimation temperature.

3.4.4 Chemical Stability of a DA Molecule

Unwanted fragmentation of molecules upon deposition by thermal sublimation can give rise to a complicated puzzle for the experimentalist [223]. In the following this will be illustrated by using the example of depositing TTF-dppz(CN), which was introduced in Sec. 3.4.1.

Mass spectroscopy

The ESI mass spectrum^{VI} of the initial TTF-dppz(CN) molecules is depicted in Fig. 3.6 (a). The maximum peak corresponds to $m_{\text{TTF-dppz(CN)}} = 629$ amu proving that the method does not affect the molecular stability. Several additional peaks at different masses are also present which are for instance attributed to impurities within the powder. The spectra shown in Figs. 3.6 (b) and (c) correspond to the sublimed molecules and those remaining at the bottom of the crucible, respectively. Peaks corresponding to intact TTF-dppz(CN) were never observed. Hence, TTF-dppz(CN) is not sublimable in vacuum, even though it was proven to be temperature stable up to ≈ 453 K in a thermogravimetric analysis (TGA) in N_2 environment (not shown).

^{VI}Spectras acquired in the Chemistry Department of the University of Basel, using a Bruker Esquire 3000plus, www.bruker.com

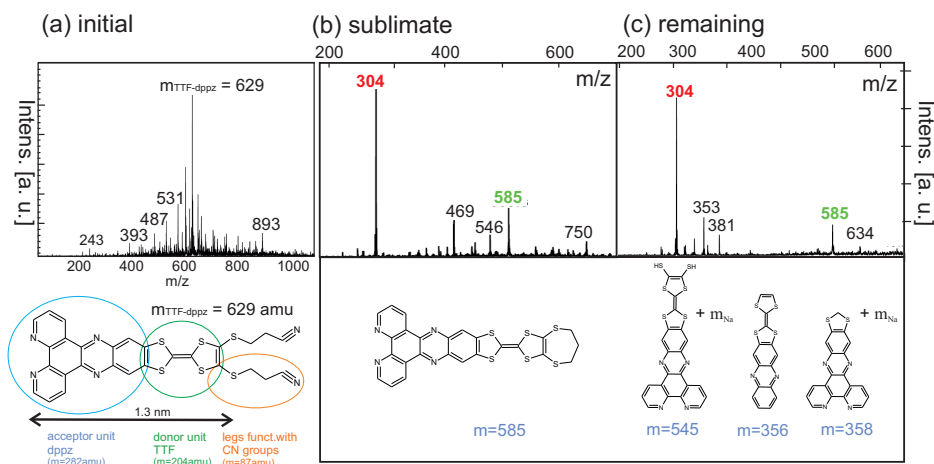


Figure 3.6: ESI-spectra of (a) the initial TTF-dppz(CN) molecule, with a mass of $m_{\text{TTF-dppz(CN)}} = 629$ amu, together with its chemical structure, and of (b) the sublimated substance, and (c) the substance remaining in the crucible. The chemical structures of the sub-units suggested for the various detected mass peaks are shown below the spectra.

The assignment of molecular sub-units to the various detected masses only on the basis of the ESI data can be to some extent arbitrary. It should be mentioned, that for the analysis of the spectra peaks $m < 200$ amu were omitted because they are difficult to distinguish from peaks arising due to solvent molecules or other possible contaminants. The masses detected by ESI and that of subsequently proposed molecular structures can vary from each other due to various reasons. If measuring in the positive mode, like done for this thesis, usually signals resulting from a protonation process ($M+H$), or the reactants of a molecule with sodium ($M+Na$) or potassium ($M+K$) become visible.

Suggestions for the various fragments evolving under sublimation are shown below the two spectra of Fig. 3.6 (b) and (c). They have two peaks in common, at $m = 304$ amu, and $m = 585$ amu. The first one is frequently observed in ESI spectra and can be attributed to contaminations due to the utilized spraying device. The second one, on the other hand, most probably corresponds to a TTF-dppz(CN) sub-unit, where the legs partly splitted off, like depicted below the spectra. This was supported by a comparative QMS analysis. Thereby, TTF-dppz(CN) was stepwise annealed in a crucible in UHV while recording residual spectra at several temperatures. In accordance to the higher probability of unwanted fragmentation discussed in the last section, only masses < 120 amu could be detected. The most distinct peaks at $m = 5$ amu to 53 amu and $m = 86.87$ amu (spectras not shown) can be attributed to molecular legs without/with the sulfur atoms, and already appear if annealing to $T_{\text{anneal}} \approx 323$ K.

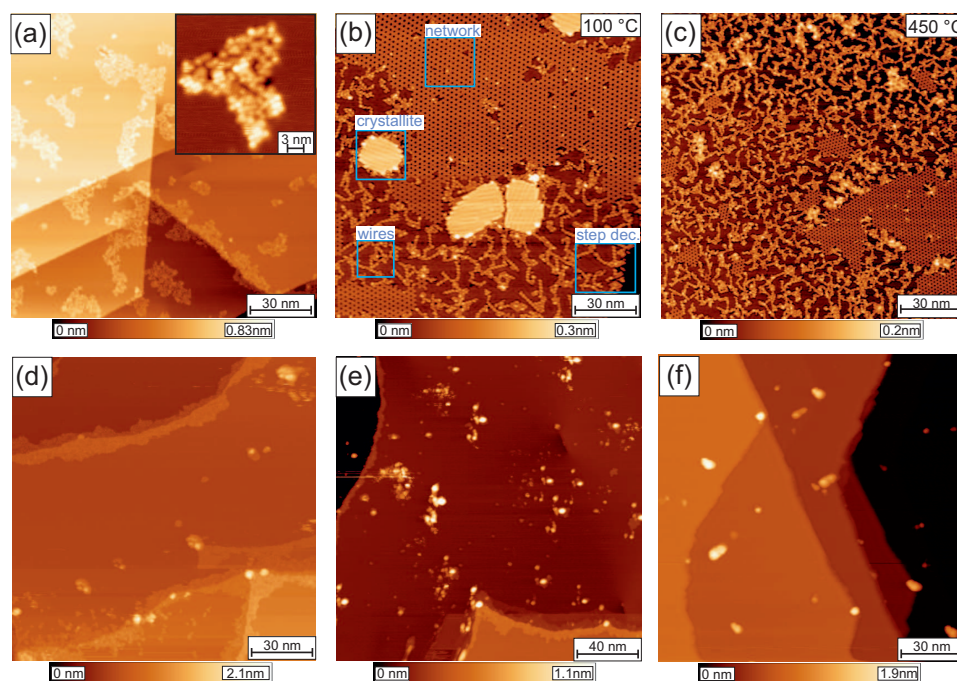


Figure 3.7: Constant current STM images of TTF-dppz(CN) on Cu(111) (a-c) and Ag(111) (d-f) after deposition and post-annealing. On Cu(111) ordered structures, namely, a hexagonal network, molecular wires, a triangular shaped step decoration, and crystallites are found. In contrast, on Ag(111) there are only random clusters. **Parameters:** Cu(111): (a) initially: $U_{\text{bias}} = 10$ mV, $I_t = 35$ pA; (b) post-annealing at 373 K: $U_{\text{bias}} = 280$ mV, $I_t = 40$ pA; (c) post-annealing at 723 K: $U_{\text{bias}} = 700$ mV, $I_t = 40$ pA; Ag(111): (d) initially: $U_{\text{bias}} = 250$ mV, $I_t = 35$ pA; (e) post-annealing at 373 K: $U_{\text{bias}} = 250$ mV, $I_t = 35$ pA; (f) post-annealing at 473 K: $U_{\text{bias}} = 100$ mV, $I_t = 35$ pA.

Accordingly, also the other peaks at higher masses in the ESI spectra ($m = 546$ amu, and $m = 469$ amu) might correspond to similar units. However, finding a sub-unit where the masses perfectly match for any of the other detected peaks remains challenging. Some ‘almost’ fitting examples are incorporated below the spectra as well, but they can not be clearly attributed towards the detected peaks. Since the synthetization starts from phenanthroline [180], also an eventual splitting within the dppz aromatic core might occur. Nevertheless, since the molecule with partly splitted legs is detected in the sublimated and remaining substrate, it might be still possible to obtain this component which maintains its characteristic D-A properties on a surface by means of thermal deposition.

Thermal deposition

The deposition of TTF-dppz(CN) on the Cu(111) surface results in different fragments, that arrange into disordered clusters [see Fig. 3.7 (a)]. To separate them the sample was subsequently annealed to 373 K. The resulting morphology shown in Fig. 3.7 (b), features four different highly ordered structures: a hexagonal network, crystallites, small wires, and a triangular shaped step decoration. Further annealing up to 723 K [Fig. 3.7 (c)] reveals that the crystallites disappear while the other three structures remain. The relative ratio of network and wire structures on the surface remains constant after annealing at 373 K and 723 K which was evaluated by comparing several overview images.

Similar experiments on Ag(111) [see Fig. 3.7 (d-f)] did not result in any ordered structures after post-annealing. In contrast to Cu(111), the molecules already start to desorb from the surface at an annealing temperature of 473 K. Hence, Cu atoms, which at elevated substrate temperatures are available in increased number, could be involved in the built-up of at least one of the assemblies [224].

For a deeper analysis, detailed images of each structure are depicted in Fig. 3.8. A crystallite is shown in Fig. 3.8 (a). The high resolution inset suggests the built-up by a quadratic unit cell with a periodicity of $d_{\text{cryst}} = 0.47 \pm 0.01$ nm, which is indicated by the model superimposed on the right side of the high resolution inset image. Furthermore, a superstructure like pattern on top of the crystallites is visible, indicated by black lines in the model. It might arise due to a mismatch upon the built-up of the crystallites.

The step edge decoration shown in Fig. 3.8 (b) consists of a two monolayer high construction. Particularly, the first layer exhibits a high similarity compared to the crystallites, also concerning the periodicity of the building units estimated to $d_{\text{stepdec}} = 0.49 \pm 0.02$ nm. For the second layer two possibilities were observed both being visible Fig. 3.8 (b): either a straight ordering of molecules, or the arrangement into a triangular shaped structure.

Figure 3.8 (c) shows the molecular wires. The periodicity of the building blocks was estimated from several STM images to $d_{\text{wire}} = 1.15 \pm 0.1$ nm, if assuming each protrusion as one molecule. In average, about 5 molecular units build up a wire. In the same surface areas, always also small clusters (named flakes, increasing number with increasing post-annealing temperature) and wire like structures composed by smaller building units were observed indicating that several molecular sub-units are present in these areas. The highly ordered hexagonal porous network, depicted in Fig. 3.8 (d), with a periodicity of $d_{\text{network}} = 0.83 \pm 0.04$ nm is the most remarkable structure. It contains a substructure visible in the two closest recorded constant height slices of a 3D combined $\Delta f/I_t(x, y, z)$ data set, showing a small detail of the network structure around a pore, which is presented in Fig. 3.8 (e). The 3D

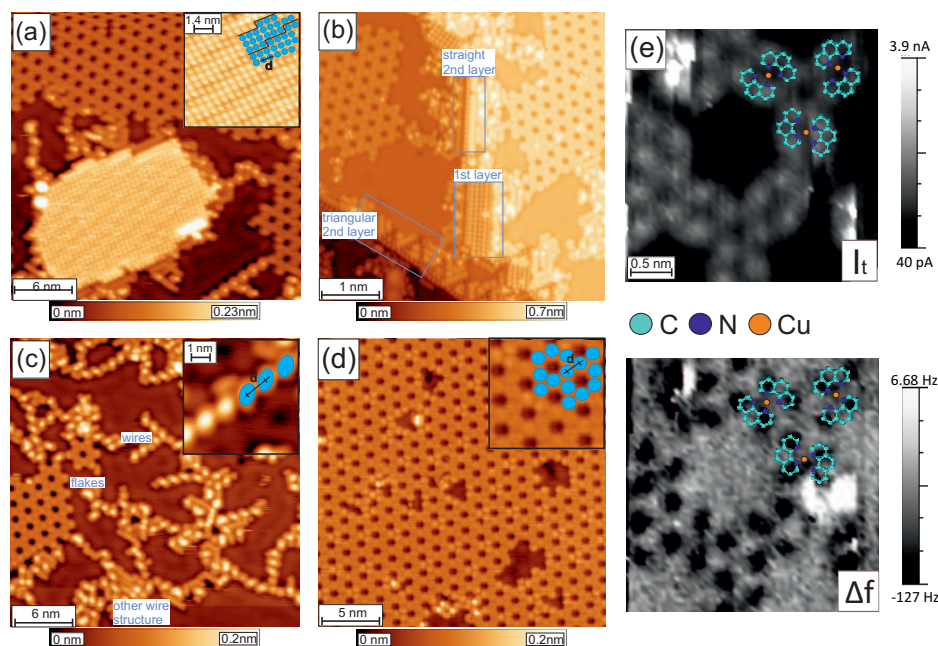


Figure 3.8: Ordered structures on Cu(111) after post-annealing. (a) Crystallites (b) Step decoration. (c) Wires. (d) Hexagonal porous network. (e) Closest recorded constant height slices of a combined 3D DFS data set revealing the network's sub-structure. **Parameters:** (a) $U_{\text{bias}} = -280$ mV, $I_t = 30$ pA; (b) $U_{\text{bias}} = 280$ mV, $I_t = 30$ pA; inset: $U_{\text{bias}} = -280$ mV, $I_t = 30$ pA; (c) $U_{\text{bias}} = -800$ mV, $I_t = 34$ pA; inset: $U_{\text{bias}} = 600$ mV, $I_t = 30$ pA; (d) $U_{\text{bias}} = -200$ mV, $I_t = 30$ pA; (e) combined 3D DFS data set recorded in the grid- mode, closest recorded constant height slices.

spectroscopy data set features areas where tip instabilities occurred (contrast exaggerated). Therefore, it is not used for further analysis of the interaction forces or potential energy landscape. Similar instabilities also repeatedly occurred during imaging.

We assume that the network evolves under Cu atom coordination similar to [224]. The fact that the dppz unit exhibit a well known metal-chelating functionality, which is given by the diimine groups [180, 225, 226] suggests that the molecules building up the network should contain these. All fragments observed in the ESI spectra which contain diimine can be excluded because they are too big to construct the network. Also, the dppz sub unit does not build up the network evidenced by SPM experiments of dppz on Cu(111) shown in Fig. 3.9 before (a) and after (b) post-annealing of the sample at 373 K. Three different periodic arrangements are visible, none of them equals the network structure.

Another possible candidate, phenantroline [see the chemical structure in Fig. 3.8 (e)] fits well in terms of its size and geometry, which is only a weak indication. However, within the ESI mass spectra its mass of $m_{\text{phen}} = 182$ amu

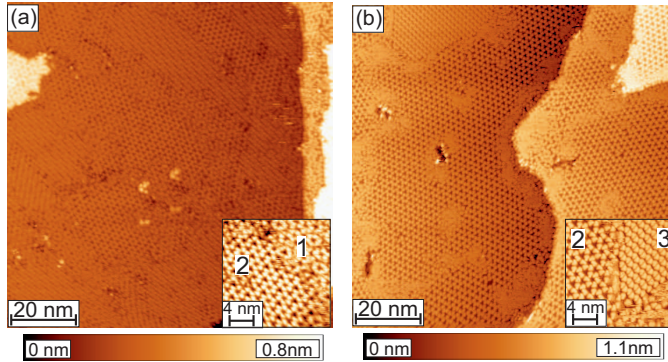


Figure 3.9: Approximately 1ML of dppz on Cu(111) (a) directly after deposition, and (b) after post-annealing at 373 K dppz arranges in (three) hexagonal arrangements, but none of them equals the network structure. Deposition of coverages of less or more than 1ML (not shown) also did not result in the hexagonal network found after post-annealing of TTF-dppz(CN) on Cu(111). **Parameters:** (a) $U_{\text{bias}} = 200 \text{ mV}$, $I_t = 40 \text{ pA}$; inset: $U_{\text{bias}} = 800 \text{ mV}$, $I_t = 30 \text{ pA}$; (b) $U_{\text{bias}} = 1 \text{ V}$, $I_t = 55 \text{ pA}$; inset: $U_{\text{bias}} = 1 \text{ V}$, $I_t = 25 \text{ pA}$.

was always neglected as it is smaller than 200 amu. Concerning the comparative quadrupole mass spectroscopy experiment it was also not detected directly ($m_{\text{max, QMS}} = 118 \text{ amu}$), but at least the sum of two smaller detected peaks was matching $m_{\text{phen}} = 182 \text{ amu}$.

In case that the network would be composed by phenanthroline, the post-annealing of the TTF-dppz(CN) fragments on Cu(111) would give rise to another on-surface fragmentation by involving Cu atoms to which a catalytic effect could be assigned. On this basis, also models for the other ordered structures could be formulated. Nevertheless, the separation of the various fragments on a metal surface was not possible, neither for post-annealing of the samples nor for the deposition onto a cold substrate like for Fig. 3.7 (a) where the substrate temperature was kept at $T \approx 80 \text{ K}$ during the entire deposition.

A different situation was obtained after the deposition of TTF-dppz(CN) onto a cold NaCl/Cu(111) surface like described in Sec. 3.1. As depicted in Fig. 3.10 (a) single molecular structures are attached to steps and kinks between the second and third monolayer of the NaCl islands [227]. A structural similarity with TTF-dppz(CN) becomes apparent by comparing the image with the chemical structure in the high resolution inset. The fact, that furthermore the measured length of $d = 1.2 \text{ nm}$ is in good agreement with the one of TTF-dppz(CN) from the dppz core up to the onset of the flexible legs, suggests, that the deposition on cold NaCl can indeed lead to a fragment separation. Accordingly, the observed molecules correspond to TTF-dppz(CN) with partly missing legs still maintaining their D-A properties.

However, the determination of the exact unit remains rather difficult, since

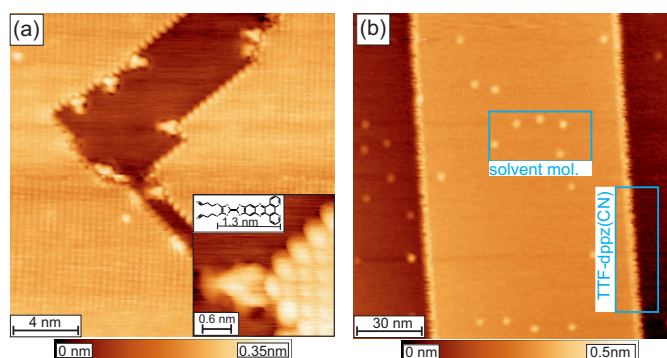


Figure 3.10: (a) Single TTF-dppz(CN) molecules with missing legs at kinks between the second and third monolayer of NaCl. (b) TTF-dppz(CN) on KBr(001) deposited by the molecular spray technique at room temperature. The molecules adsorb at step edges while the dots on the terraces are attributed to solvent molecules. This is the only image recorded with a highly n-doped conductive Si-cantilever made by a home-built AFM operating at room temperature [228]. **Parameters:** (a): $U_{\text{bias}} = 1.5 \text{ V}$, $I_t = 25 \text{ pA}$; inset: $U_{\text{bias}} = 1.2 \text{ V}$, $I_t = 25 \text{ pA}$; (b): $\Delta f = -20 \text{ Hz}$, $A_{\text{osc}} = 2 \text{ nm}$, $f_0 = 166.6 \text{ kHz}$, $k = 30 \text{ N m}^{-1}$, $U_{\text{bias}} = -350 \text{ mV}$.

according to the ESI spectra the splitting might occur at various positions. For a clear assignment, high resolution imaging revealing the chemical bonds inside the molecule would be mandatory each time prior to any other investigation, until a fragment with identical structure compared to those used before, would be found. Furthermore, the sticking of the fragments on the substrates is reduced compared to that for the initial molecules still containing the CN functionalization, which in turn makes the experimental use of single molecules more difficult.

ESI deposition

In order to deposit the initial functionalized TTF-dppz(CN) molecules onto a surface the molecular spray deposition technique^{VII} was employed. The detected mass spectrum shown in Fig. 3.6 (b) already indicates that this method is capable of depositing the intact molecules. For the experiment the molecules are sprayed together with an ethanol-toluene (1:1) solvent. Especially on insulating surfaces the distinction between molecules and the solvent on the surface might thus not be straightforward. To overcome this potential problem, primary to the actual experiments with TTF-dppz(CN) only solvent molecules were sprayed onto the KBr(001) surface resulting in arbitrarily distributed small clusters all over the surface. Step edge decoration was not observed at all.

This changes if TTF-dppz(CN) is included in the solution and sprayed under the same conditions. In addition to the arbitrarily distributed clusters, the

^{VII}Molecular spray, www.molecularspray.co.uk

steps become decorated, shown in Fig. 3.10 (b). Because step edge decoration was only observed if solvent molecules and TTF-dppz(CN) were sprayed together, it should be composed by intact TTF-dppz(CN). Higher resolution images of this step decoration similar to Fig. 3.10 (a) are not available at the moment, since the microscope attached to the chamber where the spray unit is mounted operates at room temperature. Yet, we expect that the molecules attach towards the steps through their CN functional groups similar as in the case of [210].

3.5 Summary

The used equipment was presented, and sample preparation procedures described. By using the example of TTF-dppz(CN) furthermore general challenges in the handling of large and/or complex molecules were targeted. Here, unwanted fragmentation took place upon annealing within the crucibles. Interestingly, the ordered structures were found on Cu(111) with high reproducibility resulting in a time consuming puzzle. In order to avoid such puzzles, the testing of the deposition of new noncommercial molecules prior to SPM experiments is recommendable. However, a reliable deposition of intact TTF-dppz(CN) molecules is possible with the molecular spray technique.

Part II

Single Molecule Investigations

Chapter 4

Mutual Influence of Molecules and Surfaces Upon Adsorption

Innumerable molecules can be considered as interesting for organic based electronic devices coming along with a similar high diversity of chemical structures and associated properties. Hence, it is futile to give a comprehensive picture of the underlying physics, particularly if the molecules are to be regarded adsorbed on a surface. Yet, with a focus on aromatic molecules, metal surfaces and thin insulating films on metals, several important mechanisms with regards towards the upcoming chapters will be issued.

For an understanding about the modifications due to the mutual influence between a molecule and a surface in close proximity towards each other, at first one needs to know about the general characteristics of the initial molecule and surface [Sec. 4.1 and 4.2, respectively]. If the two are then brought together, the resulting interface is defined by the strength and nature of the involved molecule-surface interactions, classified into physisorption and chemisorption [Sec. 4.3]. For every molecule on every surface a characteristic adsorption geometry is expected [Sec. 4.3], which is in turn a characteristic observable of the present interactions. Besides, it governs the mechanical behavior [Sec. 4.4] on the surface and furthermore, also the electronic interface structure [Sec. 4.5].

4.1 Molecules in Gas Phase

The geometry of a molecule and its electronic structure are intimately connected, which becomes clear by taking a closer look towards the complex theory of chemical bonding and molecular orbital theory. While the following discussion will be restricted to a phenomenological description of some important concepts concerning the molecules of relevance in this thesis, a detailed overview can be found in [229, 230]. Similar to the description of short-range interaction forces in Sec. 1.2 a chemical bond results from an

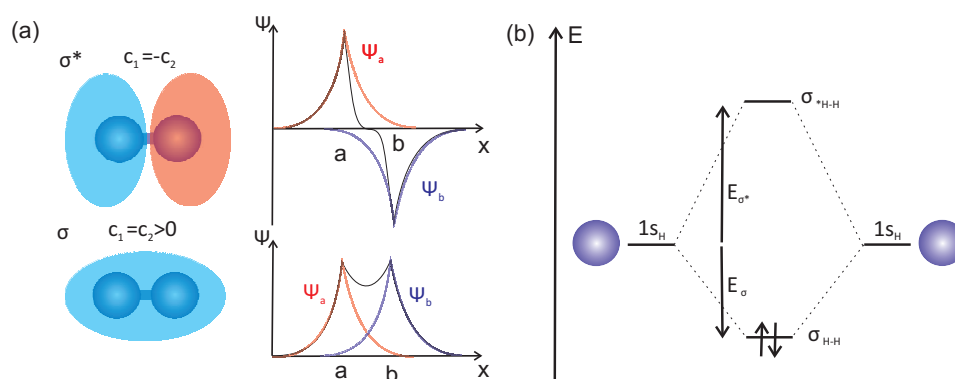


Figure 4.1: The formation and orbital structure of an H_2 molecule (a) Anti binding σ^* and binding σ MO, resulting from the LCAO. (b) Corresponding schematic energy diagram

overlap of the wave functions of at least two atoms at separations in the regime of a few Ångstrom, and can be described by the Morse potential [see Eq. 1.19]. If the overlap of all atoms that participate to the bond, leads to an overall attractive interaction, a molecule will be formed. The new molecular orbitals (MO) can be calculated from linear combinations of the atomic orbitals (LCAO) of the participating atoms. Subsequently, in accordance to the Pauli principle, they are successively populated by maximal two electrons per orbital, and by aspiring for the lowest energy conformation the geometric arrangement is determined.

This should be illustrated by the relatively easy example of the H_2 molecule. By combining two single H atoms with their $1s$ wave functions Ψ_1 and Ψ_2 , the electron distribution is given by $\sigma^2 = (c_1\Psi_1)^2 + (c_2\Psi_2)^2 + 2c_1\Psi_1c_2\Psi_2$, differing from that of two single atoms by the last term. Because the coefficients c_1 and c_2 , defining the relative ratios of the atomic wave functions, whereas $\sum_i c_i = 1$, can be positive or negative, there are two MOs, which are illustrated in Fig. 4.1 (a). Hence, for $c_1 = c_2 > 0$, the electron population between the atom cores increases, and leads to a binding MO σ . On the other hand, for $c_1 = -c_2$ the MO features a nodal plane, corresponding to a reduced population between the cores, which results in an anti binding MO σ^* . Hence, in the schematic energy diagram in Fig. 4.1 (b) the energy levels of σ and σ^* are located below and respectively above those of the single atoms. A closer look furthermore reveals that the energetic lowering for σ is less than the gain for σ^* , which is due to the repulsive energy between two electrons that share the space within one MO.

Hybridization and Conjugation

By regarding bonds between different atoms, the complexity of the situation considerably increases. By regarding organic compounds which are based on

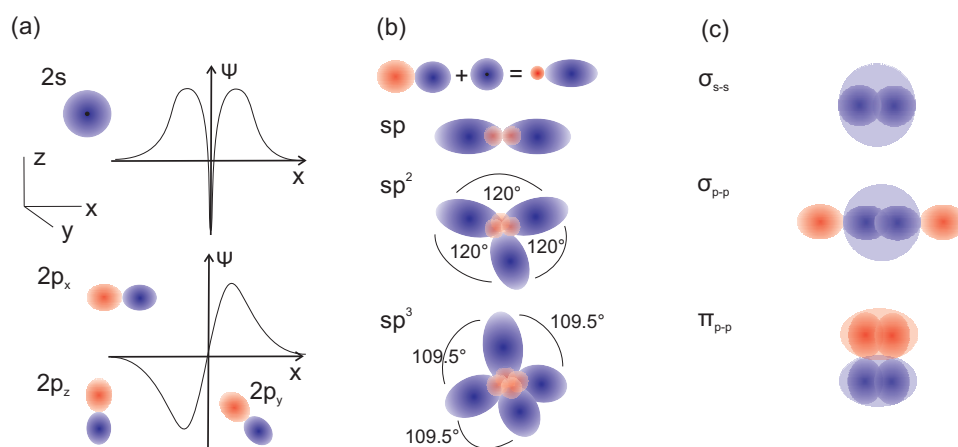


Figure 4.2: Concepts for chemical bonding. **(a)** Scheme of the 2s and the three 2p orbitals. **(b)** Concept of hybridization. **(c)** Distinction of σ - and π - type bonds.

carbon (C), three different orbital types play a role, 1s orbitals [Fig. 4.1 (a)], 2s orbitals [see Fig. 4.2 (a), upper row] and three types of 2p orbitals, 2p_x, 2p_y, and 2p_z [Fig. 4.2 (a), lower row]. However, since the formation of chemical bonds in molecules is mediated by valence electrons, one only needs to consider the p- and 2s orbitals. It should be ruled out, that only orbitals with equal symmetries with respect to all symmetry elements can be combined. Hence, the construction of MOs might become a rather difficult task, particularly concerning the association of the constructed orbitals with certain molecular bonds.

In this context, the concept of hybridization, illustrated in Fig. 4.2 (b), is very helpful. The MOs are mixed in different amount and subsequently re-arranged into a set of geometrically directed **hybrid orbitals**. The overlap between 2p and 2s orbitals leads to a shift of the total electron distribution which determines the shape of the hybrid orbitals. For a diagonal arrangement resulting in a **sp**-hybrid orbitals one s and one p orbital are mixed. Similarly, the mixing of one s and two (three) p orbitals leads to a trigonal (tetrahedral) alignment and **sp²** (**sp³**) hybrid orbitals directed accordingly.

Particularly, sp² hybridized carbon (C) systems feature an important characteristic, that is **conjugation**. To define this property, one needs to distinguish between two different types of bonds which are defined by the way in which the overlap between the different orbitals occurs, as it is illustrated in Fig. 4.2 (c). Bonds that arise via a head-on overlap of the orbitals, so that the electron distribution of the binding MOs is localized between the contributing atoms, they are defined as σ - bonds (e. g. σ_{ss} , or σ_{sp}). On the other hand, the sidewise overlap of two orbitals above and below the molecular plane, so that it becomes a nodal plane, are referred to as π bonds.

Conjugation is now defined by the availability of π bonds, being true for all

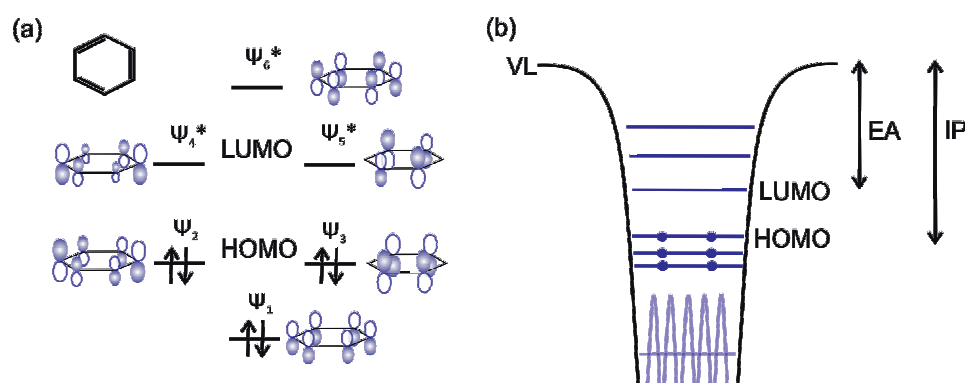


Figure 4.3: Hückel theory and aromaticity. (a) Hückel calculated structure of the π electrons of benzene. The H atoms in the chemical structure are omitted. (b) Scheme of the electronic structure of a π -conjugated molecule with rigid atom cores (usually omitted for reasons of simplicity) and delocalized electrons within the π MOs.

molecules introduced in Sec. 3.4.1. In a carbon system, where the p_x -, and p_y - orbitals of the initial atoms form sp^2 hybrid orbitals, the remaining p_z orbitals can interact via π_{pp} bonds, which will be discussed for example in benzene in the next section. Even though single π - bonds are much weaker than σ bonds, the additional availability in sp^2 hybridized organic carbon (C) based compounds gives rise to a highly increased chemical stability compared to other compounds.

Hückel Theory and Aromaticity

For the determination of the MOs and electronic energy levels of conjugated molecules, the semi-empirical quantum mechanical theory by Hückel gives a straightforward approximation without the need of explicitly solving the Schrödinger equation. The central assumption of this theory is given by a general separation of the π - and σ - bonding stages, whereas the latter are fully neglected. This is justified, because the energy gain in π type MOs is less than for σ bonds. Accordingly, the former are always located at higher energy and so the valence MOs determining the chemical reactivity of a molecule normally feature π - type.

Assuming, that the initial p_z - atomic orbitals are the MOs Ψ_n that interact via π - bonding, the resulting π -MOs Ψ are given by the various linear combinations

$$\Psi = \sum_n c_n \Psi_n. \quad (4.1)$$

Due to the spatial separation of the π - and σ - MOs, the energies of the π -MOs can be approximated by using the quantum mechanical concept of a

particle in a box [41], leading to

$$E = 2E_{\pi} \cos\left(\frac{k\pi}{n+1}\right), \quad (4.2)$$

whereas n stands for the numbers of atoms in the molecule, and k can be any positive integer between 1 and n .

According to the Hückel rule, a conjugated molecule with $(4n+2)$ π - electrons, n being any integer, is defined as an **aromatic compound**. For this class of molecules, the additional energy gain mediated by π type interactions is maximized. This is exemplarily illustrated by using the example of benzene in Fig. 4.3 (a), which is one of the most famous aromatic molecules. Benzene features $4 \times 1 + 2 = 6$ π electrons, and hence six π MOs, that can be derived within the Hückel theory: For the MO with lowest energy Ψ_1 the electron distribution is equal at all six atoms, and hence, the electrons are fully **delocalized**, which is a main characteristic of conjugated systems. Ψ_2 and Ψ_3 (binding) as well as Ψ_4 and Ψ_5 (anti binding) are degenerate and feature one and two nodal planes, while the energetically highest anti bonding orbital Ψ_6 comes with three nodal planes.

A generalized energy scheme for an aromatic molecule is illustrated in Fig. 4.3 (b). The ion cores are fixed at certain positions, while the π - electrons located in the valence (frontier) MOs are fully delocalized. The most important MOs are usually the highest occupied (HOMO) and lowest unoccupied (LUMO) MO, whereas the difference between the vacuum level (VL) and the LUMO is defined as the electron affinity (EA), and that between the VL and HOMO as the ionization potential (IP). When molecules are to be imaged by STM, again the HOMO and LUMO are the most important MOs, because they are closest towards the Fermi level. For typical bias voltages in the range of a few volts, MOs higher than the LUMO can usually not be excited, and for those below the HOMO the tunneling probability is much smaller than for the latter. A further characteristic of aromatic molecules is given by a comparably small HOMO-LUMO gap (≈ 1.5 eV to 3 eV [231]), giving rise to intense adsorption bands in the visible. All molecules presented in Sec. 3.4.1 feature a high degree of aromaticity. Several benzene rings dominate the chemical structures.

4.2 Surfaces of Inorganic Substrates

A surface or interface is defined as the border between two media, e. g. bulk and vacuum. Due to the different spacial and hence also energetic environment of the atoms in the surface layer, the atomic arrangement and electronic structure of bulk and surface vary from each other. In some cases, the modified energetic conditions even lead to surface reconstructions, which will be fully neglected in the following as they did not play a role for the

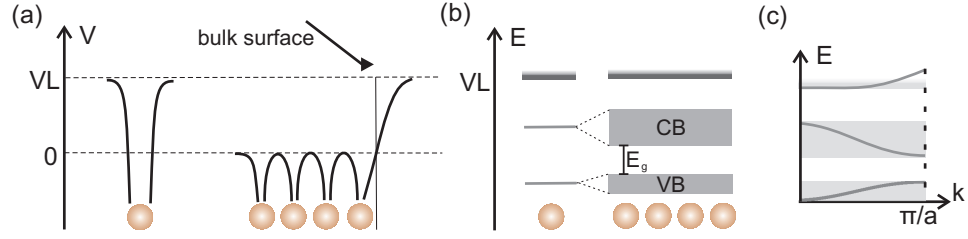


Figure 4.4: Single atom vs. solid metallic crystal terminated by a surface. **(a)** Schematic potentials. At the surface, the periodic potential of the bulk decays exponentially into vacuum. **(b)** Energy diagrams. The single atomic energy levels split into bands. **(c)** Corresponding energy diagram for one unit cell.

surfaces used during the thesis. Detailed introductions into the physics of surfaces are given in [232–234].

Bulk Crystals

Similar to the formation of a molecule, a solid crystal arises due to interactions between initially free atoms. In Fig. 4.4 (a) the potentials of a single atom and that of a bulk crystal terminated by an ideal surface are illustrated. Inside the bulk it features a periodic curvature, which gives rise to a splitting of the discrete energy levels of the single atoms into energy band structures, separating energetically allowed from forbidden regions, which is depicted in Fig. 4.4 (b). On the other hand, at the surface, the potential exponentially decays into vacuum, whereas both curves ideally perfectly match each other at the surface borderline. Due to the periodicity, and because in solid state physics the bulk is usually assumed as infinitely large, the energy landscape is fully characterized by regarding one unit cell, mostly within the reciprocal space [see Fig.4.4 (c)].

The propagation of electrons inside the crystal is described by Bloch electron wave functions [175]. Each electron has to satisfy the one electron Schrödinger equation [see Sec. 1.1], whereas for the periodic potential it holds $V(r + R) = V(r)$, with R being the lattice vector. According to the Bloch theorem now the wave functions within the periodic potential are given by the product of a plane wave and a function $u \propto e^{ikR}$ featuring the periodicity of the lattice, meaning that

$$\Psi(r + R) = e^{ikR}\Psi(r), \quad (4.3)$$

k being the wave vector. The ground state of the N electrons is then constructed by successive filling of the energy levels up to the Fermi energy by taking into account, that due to the Pauli principle the Fermi-Dirac distribution becomes significant.

For insulators or semiconductors, the bands are either completely filled or completely empty. The highest occupied band, the valence band is sepa-

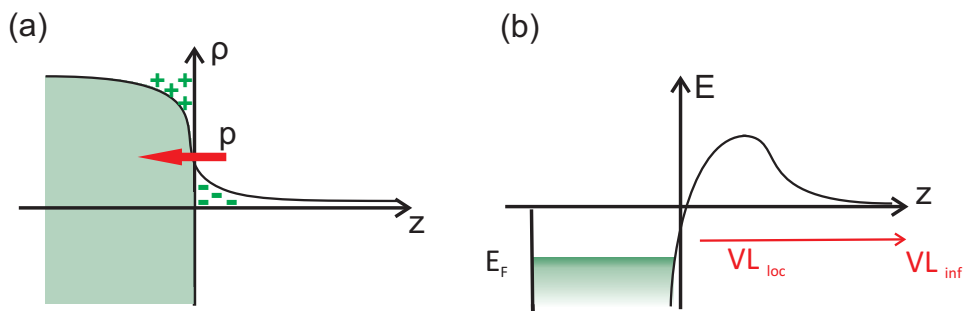


Figure 4.5: Formation of the surface dipole. (a) The electron density across a surface ‘spills’ out into vacuum leading to a net dipole moment. (b) Schematic energy diagram. Here, the local vacuum level (VL_{loc}) needs to be distinguished from the one at infinite separation from the surface (VL_{inf}).

rated from the following unoccupied one, the conduction band, by an energy gap. The reason for this gap lies in the respective bonding mechanisms and electron configurations. Its size determines whether the solid is a semiconductor or an insulator. Energy gaps as high as that no thermally activated electrons can overcome it, correspond to insulators. In contrast, for a metal a certain amount of bands is only partially filled, or the conduction band and valence band energetically overlap. Accordingly, for insulators and semiconductors, the Fermi energy, separating occupied states from empty ones is located within the energy gap, while for a metal it lies within the conduction band. This fact is the reason for the high electric and thermal conductivity of metals, where electrons at the Fermi level can pick up infinitesimal small amounts of energy enabling them to gain kinetic energy in an electric field.

Surface and Surface Dipole

A central assumption in the description of bulk solids is given by the approximation of infinite size. But, what are the consequences of a surface, which abruptly interrupts its periodicity?

The ideal surface in Fig. 4.4, actually oversimplifies the situation. There, it is assumed that the periodic potential is cut at the surface without any modifications in its close proximity. But actually, the modified binding situation for the surface atoms given by the sharp interrupt at the surface has indeed consequences for the surface structure. For instance, electronic surface states located in the energetically forbidden region of bulk states might be present. They are described by Bloch waves with complex wave vectors within the crystal followed by an exponential decay starting at the surface. Historically, Schottky- and Tamm- surface states are distinguished [233]: for the former a nearly free electron gas treatment is applied while the latter are calculated within the tight binding model as linear combinations of the atomic orbitals. One famous example is given by the Shottky type surface

state on the Cu(111) surface described in relation to Fig. 1.3 and Sec. 3.3. A second characteristic is directly related to the fact, that the electronic charge distribution at the surface is ‘spilling’ out into vacuum with an exponential decay length, which is illustrated in Fig. 4.5 (a). This negative electron charge is then neutralized within the first atomic rows of the bulk, where a slight positive charged region remains. Even though for metals this region only concerns the very first bulk layers, the charge redistribution causes a so called surface dipole layer region around the surface. The effective dipole moment will then point from the out- to the inside of the crystal, and its strength depends on the regarded crystal facet. Accordingly, the work function, defined as the energy needed to bring an electron out of the solid into vacuum, is increased, which is shown in the schematic energy diagram of a real surface in Fig. 4.5 (b).

Local Work Function

The work function actually generally features a local character, and is sensitive towards different crystal orientations, and lateral inhomogeneities across the surface. For instance, for Cu the different work functions for different common surface orientations range from 4.59 eV for the [100]- direction to 4.94 eV for the [111]-direction [176]. With its definition as the energy difference between the Fermi- and vacuum levels, the local character of the work function necessarily goes back to the position of the vacuum level, because the Fermi level is a pure bulk property. By regarding the electron at a position at rest just outside of the surface, it is still affected by the surface potential. The electron now stays at the so called local vacuum level (VL_{loc}), which approximates towards the absolute vacuum level (VL_{abs}) at infinite separation from the surface, indicated in Fig. 4.5 (b).

Accordingly, one has to regard the local work function Φ_{loc} [235,236], whose exact definition comprises bulk- and surface dependent terms:

$$\Phi_{\text{local}} = -\mu - \frac{ep}{\epsilon_0}. \quad (4.4)$$

Here, μ is the chemical potential, e the elementary charge, p the surface dipole, and ϵ the dielectric constant. The chemical potential is related to the chemical bonding and exchange correlations of the electrons within the solid, while second one refers to the formation of the local surface dipole. All local work function changes are of electrostatic origin, and are accessible by KPFM or local bias spectroscopy [see Sec. 1.3.2]. Several studies about work function changes for different facets across one surface [95], at steps or kinks (Smucholski effect) [237], and defects or adsorbates [184,238] have been reported.

4.3 Adsorption

Adsorption [232,233] concerns the accumulation of atoms/molecules (adsorbates) from the fluid or gas phase on a solid surface. Once a particle is condensed on the surface it might either re-evaporate (desorb) or diffuse along it, which in turn can yield in adsorption at a specific site. All of these processes require certain activation energies to be overcome. The corresponding interface interactions are the same as those involved into chemical bonding with the only difference, that one of the binding partners is a macroscopic medium whose 2D surface is exposed to the microscopic atoms/molecules. Depending on the nature of the forces two different processes are distinguished, physisorption and chemisorption.

Physisorption

Physisorption is mediated by vdW forces and only weakly perturbs the electronic structure of the adsorbate. Similar to the case of the AFM tip and surface, the variation of forces with distance differs from that between two single species which is due to the different dimensionalities [see Sec. 1.2.1]. For the case of a non-reactive physisorbed atom/molecule and a solid surface, the vdW interaction potential can be modeled via the oscillation of a valence electron executing a 1D harmonic motion. The according time-dependent (non-retarded) interaction in this case is then reduced to an image-charge attraction between the oscillating valence electrons and nuclei with their image charges, resulting in a $V \propto z^{-3}$ relation [232].

A typical physisorption potential modeled by a Lennard-Jones potential is depicted in Fig. 4.6 (a). It is characterized by a low binding energy (10 meV to 100 meV for noble atoms on metallic surfaces) and large equilibrium separation (0.3 nm to 1 nm). Accordingly, the atoms/molecules are located at relatively large distances from the surface and are usually highly mobile parallel to it. Typically, physisorption only occurs if stronger chemisorption interactions are not present. Furthermore, experimentally the high diffusion rates related to the weak interaction potentials mostly require low temperature investigations in order to stabilize the adsorbates on the surface.

Chemisorption

In contrast, chemisorption is related to the formation of either new chemical bonds between the adsorbate and the solid surface, for which essentially the same rules as for chemical bonds apply, and/or by charge transfer between adsorbate and molecule. Actually, the borderline between physisorption and chemisorption is not clearly defined. Charge transfer does not only correspond to chemisorptive processes, but can also very weakly be present under physisorption [239]. However, the formation of new local directed bonds between adsorbate and surface is clearly attributed to chemisorption.

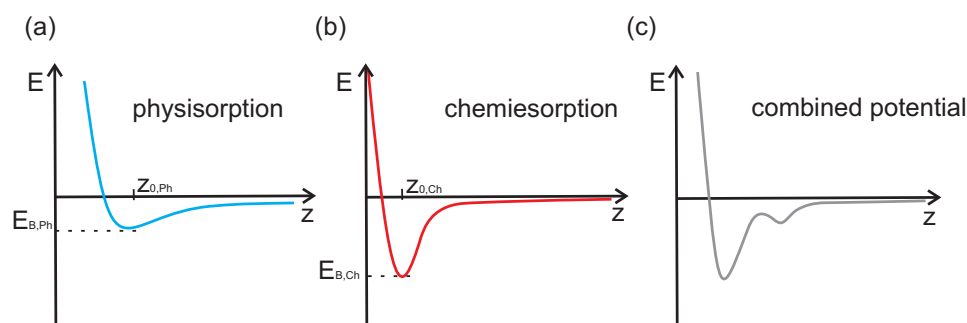


Figure 4.6: Physisorption vs. Chemisorption. (a) A typical potential curve of a physisorption process, modeled by a Lennard-Jones potential. (b) The chemisorption process differs from physisorption in a smaller equilibrium separation z_0 and higher binding energy E_B . It is traditionally modeled by a Morse potential. (c) Combination of physisorption and chemisorption.

The strongest interactions can be expected for overlapping occupied and unoccupied orbitals, i. e. electron transfer from the surface into the LUMO or electron donation from the HOMO into empty substrate states. Chemisorption potentials are traditionally modeled by Morse potentials. A typical curve is depicted in Fig. 4.6 (b). The main difference to physisorption is given by a much shorter equilibrium separation (0.1 nm to 0.3 nm) and higher binding energies up to a couple of eV.

Combined Adsorption Potential

Typically, an adsorption process requires to look at a combined physisorption and chemisorption potential, like depicted in Fig. 4.6 (c). The present example describes combined physisorption and chemisorption while more or less sustaining the adsorbate chemical structure. In other cases, an adsorption barrier might be present such that a minimum energy is required for adsorption, or also activation barriers between the physisorption and chemisorption wells. Furthermore, a chemisorptive process might even be accompanied by the dissociation of the adsorbate upon adsorption.

Adsorption Geometry

The adsorption geometry of a molecule on a surface is a characteristic observable reflecting the interaction forces at the interface. However, in contrast to single atomic adsorbates, its prediction is rather subtle, because of their extended sizes [240]. The schematic drawing in Fig. 4.7 illustrates the issue. A main point is, that in contrast to a single atomic adsorbate, molecules cover several substrate atoms, and so the corrugation potential is averaged over the whole area as well. Consequently the adsorption landscape becomes much more complex. Nevertheless, molecules prefer certain configurations

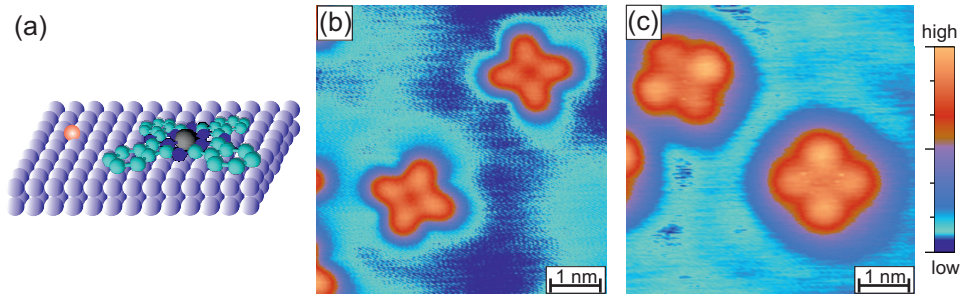


Figure 4.7: Different adsorption conformation of CuPc. **(a)** Chemical structure of CuPc and illustration of the differences for the adsorption of large aromatic molecules in contrast to single atoms. **(b,c)** CuPc on the structural very similar Ag(111) **(b)** and Cu(111) **(c)** surfaces. Still, the contrast is very different, which can be traced down to huge differences in the adsorption energies on the two surfaces. Parameters: **(b)** $U_{\text{bias}} = 100 \text{ mV}$, $I_t = 20 \text{ pA}$; **(c)** $U_{\text{bias}} = -250 \text{ mV}$, $I_t = 30 \text{ pA}$.

above the substrate, which is related to the site dependence of the molecule-surface interaction across the molecular structure. This leads to a second characteristic: because molecules possess several internal degrees of freedom, i. e. vibrational, conformational, and orientational degrees, conformational changes may likely occur, and depending on its mechanical properties (e. g. flexibility, elasticity) and the specific interaction with the underlying substrate a molecule can adapt several different geometries [241]. For instance, more flexible side groups of the molecule might be bended up- or downwards upon adsorption.

This specific process can not be traced down to a simple rule, not even for the same structure on different surfaces. The adsorption will be different and even small modifications can yield in considerably different adsorption geometries. To give an example, the adsorption of a Cu phthalocyanine on different noble metal surfaces results in different conformations, as shown in Fig. 4.7 for the Cu(111)- and Ag(111)- surface. Even though both surfaces feature the same symmetry, the observed contrast on Ag(111) has fourfold symmetry, while that on Cu(111) is reduced to twofold. Furthermore, the molecular contrast on the Cu(111) surface is less sharp, indicating a stronger hybridization. Both effects originate from the differences in the molecule surface interactions, which are much stronger on Cu(111) [242]. The fact, that different benzo-pyrrole rings are aligned above different local adsorption sites causes differences in the local molecule-surface interactions for the different rings, and consequently on Cu(111) two out of four rings appear less pronounced. A second example, which will be subject to the next chapter concerns a free-base core porphyrin molecule. Strongly polar cyanophenyl side groups provoke a conformational change upon adsorption on Cu(111).

4.4 Mechanical Properties

Whether conformational changes in the molecular structure upon adsorption occur is also strongly dependent on the molecular flexibility, which can be investigated via the elasticity module defined by

$$E = \frac{\sigma}{\epsilon}. \quad (4.5)$$

Here, $\epsilon = \frac{\Delta l}{l}$ is the strain, while $\sigma = \frac{F}{A}$ refers to the stress upon deformation. However, for complex geometries, the expression for the stress differs from this simple definition, because the strain is then orientation dependent and becomes a tensor.

Since the stress is related to the applied force F per unit area A , the molecular elasticity can be investigated by studying the molecule's response to mechanical forces, and thus by means of AFM. The stress is then related to a stiffness, $k = -F/z$ which can be estimated via z dependent spectroscopy curves of the frequency shift. Recently, multidimensional combined z dependent spectroscopy data $I_t(x, y, z)/\Delta f(x, y, z)$ were analyzed concerning the atomic-scale mechanical properties of C_{60} molecules on Cu(111) [96]. Different slopes of vertical $F_{ts}(z)$ -curves in the repulsive regime at different sites, for instance C atoms and hollow sites, could be directly attributed to site dependent variations in the elastic atomic-scale stiffness between tip and molecule. In the small amplitude limit ($A < 100$ pm) the stiffness and frequency shift can be connected via the force gradient [see Sec. 1.3.2]

$$k_{ts} = -\frac{2k\Delta f}{f_0}. \quad (4.6)$$

Here, k is the stiffness of the tip-molecule junction, which includes the response to mechanical forces, and k the stiffness of the tuning fork.

The elastic properties of adsorbed molecules are crucial for the complete field of molecular growth on surfaces. The adsorption energy and -conformation govern for instance the diffusion barriers [21], and hence also the types of available self-assemblies. Depending on the strength of intermolecular and molecular surface interactions, molecules either grow in a layer-by-layer- (Frank-van-der-Merwe), mixed- (Stranski Krastanov), or island growth mode (Vollmer-Weber). In the first [last] case the molecule-surface interaction is stronger [weaker] than the molecule-molecule interaction, while for the mixed- mode the difference between the two interactions depends on which layer of the assembly is considered.

A further important impact for the growth behavior with respect to the elastic properties concerns the coverage of molecules. In close packed layers, the molecule might be bent differently compared to low coverage configurations in order to accommodate stress induced by the different unit cell packaging. Accordingly, different assemblies may exhibit different elastic

properties [243], which is subject to molecular flexible electronics, proposing for instance flexible displays [244, 245].

4.5 Interface Electronic Structure

The performance of any organic based (opto-) electronic device depends on the electronic structure at the interface governing the charge carrier injection barriers. For a detailed understanding about the mutual influence of the adsorbate and surface, one has to take a closer look towards the interface energy alignment. The following discussion will be restricted to metal-organic interfaces and the double barrier tunneling junctions relevant for the adsorption of molecules on thin insulating films on metals.

4.5.1 Metal-Organic Interface

The central question for a metal-organic interface concerns the energetic positions of the molecular frontier orbitals HOMO and LUMO with respect to the metal work function. Several experimental studies about molecules on metal surfaces pointed out, that the simple Schottky-Mott rule of vacuum alignment [see below] at the interface does not hold true in this case anymore [246]. The reason lies in the formation of an interface dipole shifting the relative positions of the vacuum levels [246, 247], which is illustrated in Fig. 4.8 (a).

Upon adsorption, the molecule moves into the surface potential of the solid. By attempting for a common $V_{L_{loc}}$ with respect to the distance dependent surface potential the energy levels will (partially) align. A complete alignment corresponds to the Schottky-Mott limit, and is indicated by the broken lines in Fig. 4.8 (a). But usually, this does not correspond to the whole story. Upon adsorption, an interface dipole forms, which is related to microscopic charge rearrangements. This causes an abrupt shift of the surface potential for the vacuum level at the interface, in the present example downwards. It affects the local work function of the metal Φ_m , as well as the relative position of the molecular levels with respect to $E_{F,m}$. If it is directed towards the molecule [surface], Φ_m tends to increase [decrease]. An increase [decrease] of Φ_m in turn will lead to an improvement of the hole [electron] injection barriers between the molecule and metal. That is, why the interface electronic structure is so important for the performance of organic based devices. By choosing appropriate metals and molecules or covering metal electrodes by thin organic layers, the device performance can be directly tuned [248–250]. The interface dipole can have various physical origins [251, 252]. Depending on the specific molecule-surface interactions, several different processes have to be considered, which are illustrated in Fig. 4.8 (b-f), and explained in the following.

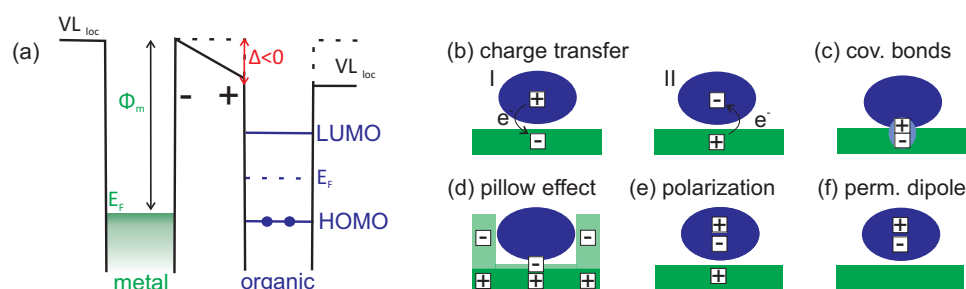


Figure 4.8: Interface dipole originating from the adsorption of a molecule on a surface. (a) Schematic energy diagram of the interface, including an interface dipole Δ . (b)-(f) Possible physical origins. For details see the main text.

Chemical Interface Interactions

In the context of chemical interactions between molecules and conductive surfaces, it is often distinguished between charge transfer phenomena [see Fig. 4.8 (b)] and the formation of new covalent bonds [see Fig. 4.8 (c)]. While for the first case the interaction can be still treated within a perturbation approach, the second one necessitates to consider even stronger interactions. However, similar as for the distinction between physis- and chemisorption, the borderline is not perfectly sharp.

A charge transfer yields a partial equilibration of the chemical potentials (Fermi levels) of metal surface and molecule. For a metal it holds $\mu_m = -\Phi_m$, while for a molecule one can refer to the mid-gap position $\mu_{mol} \approx \frac{IP+EA}{2}$, in accordance to the definition of the absolute Mulliken electronegativity [253]¹. If now $\mu_m < [>]\mu_{mol}$, charge transfer from [into] the molecule can be expected. The corresponding interface dipole moment contribution Δ_{CT} is then negative [positive] [254]. The energetic alignment in turn is accompanied with a modification of the electronic structures of both. The metallic states broaden the molecular levels and shift their relative positions with respect to the Fermi level of the metal. Accordingly, the gap may become partially filled, while for the metal the surface dipole region is affected. The strength and direction completely depends on the system regarded.

In case of directed bond formation, surface and molecule can not be regarded as weakly interacting subsystems anymore. Such a process can not be traced down to a common simple rule, as the bond formation is strongly dependent on the concrete geometries. However, such strong interactions were not observed for any molecule investigated in this thesis.

¹While this definition is sufficient for the following considerations, it should be at least noted that a more precise definition can be found in [252], which is based on the so called neutrality level

Pillow Effect

The pillow or push-back- effect, illustrated in Fig. 4.8 (d) is triggered by the simple presence of the molecule close to the surface [246]. The molecule compresses the metal wave function at the surface and thus reduces the spilling out and consequently also the local surface potential or work function. The origin goes back to repulsive exchange (Pauli-) interactions [255].

It is not limited to metal, and occurs no matter whether the interactions at the interface are triggered by physi- or chemisorption. Also, it will generally lead to a decrease of the local metal work function up to $\Delta_{\text{pillow}} \approx 0.4 \text{ eV to } 0.6 \text{ eV}$ [256].

Polarization

Polarization is in principle the counterpart of the pillow effect, and arises from the influence of the surface potential on the electronic structure of the molecule. One has to distinguish between originally unpolar- [see Fig. 4.8 (e)], and polar molecules [see Fig. 4.8 (f)], as well as between molecules which are unpolar, but undergo conformational changes upon adsorption so, that dipole moments are induced.

In **unpolar molecules**, the electrical field mediated by the surface potential leads to an induced dipole moment p_{def} , which is connected to the deformation polarization α_{def} via

$$\vec{p}_{\text{def}} = e\vec{x} = \alpha_{\text{def}}\vec{E} = \frac{1}{\epsilon_0} \sum_i \frac{e_i^2}{m_i\omega_i^2}, \quad (4.7)$$

where \vec{x} denotes the displacement of the charges from their equilibrium positions due to the electric field \vec{E} , and e_i the charge, m_i the mass and ω_i the vibration frequency of each molecule i ^{II}.

In contrast, the orientation of N **polar molecules** with permanent dipole moment $p_{\text{mol}}^{\vec{}}$ is subject to an orientation polarization, which is connected to the total dipole moment $\vec{p}_{\text{pol}} = N\vec{p}_{\text{mol}}$. This alignment competes with the thermal equal distribution, which however is small at low temperature. Similar to the case of charge transfer no general trends for the consequences of the interface structure can be drawn, because the effect strongly depends on the special system.

Finally, multipoles can also be induced upon adsorption. Conformational changes lead to different bending of certain functional groups, and hence modified orbital overlaps which in turn might influence the electronic interface structure [257]. Induced dipoles even vary within single molecules, due to the site specific interactions, which will be discussed in Chap. 6.

^{II}Note, that furthermore one might distinguish between the polarization of the electron cloud, and the polarization of the ion cores.

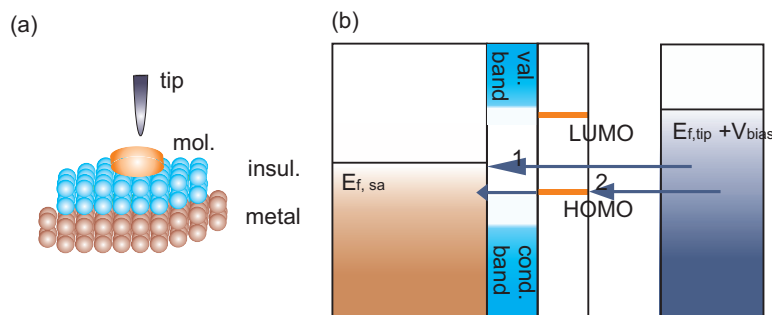


Figure 4.9: Scheme (a) and energy diagram (b) of a DBTJ. The electrons can either tunnel through the two barriers directly (1) or be localized on the molecule before passing the second barrier (2).

Total Interface Dipole

The total interface dipole is given by the sum of the above listed mechanisms:

$$\Delta = \Delta_{\text{CT}} + \Delta_{\text{pillow}} + \Delta_{\text{pol}}, \quad (4.8)$$

whereas Δ_{CT} refers to chemical interactions, Δ_{pillow} to the pillow effect, and Δ_{pol} to polarization. While the pillow effect always leads to a decrease of the local metal work function, the other two contribution can feature both directions.

Charge being transferred across the interface will always stay in the first few layers because of significant screening by its image charge potential [256], which scales with the amount of charge. In case of strong screening, the Fermi level of the interface will be pinned across the interface, and the pillow effect will be screened as well. On the other hand if it is small, the pillow effect becomes more significant [252]. This is particularly the case for physisorptive systems.

4.5.2 Thin Insulating Films on Metals

The deposition of a thin insulating sodium chloride (NaCl) film of two to three MLs leads to an effective lowering of the work function of the combined system. In case of 2MLs on Cu(111), it accounts to 4 eV [258]. This lowering is due to a mutual polarization, and is related to mechanisms leading to charge redistributions at the interface. In contrast to a metal surface, where mostly strong interactions are present, and the life time ($\partial t \partial E \geq \frac{\hbar}{2}$) of molecular resonances is in the range of $\tau \approx 1$ fs, on a thin film it increases to $\tau \approx 10$ ps [28]. Accordingly, thin insulating layers serve for a sufficient electronic decoupling [18, 28, 145], while STM operation remains possible.

An adsorbate on a thin insulating film on a metal corresponds to a double barrier tunneling junction (DBTJ), which is schematically depicted in

Fig. 4.9 (b). Tunneling electrons have to overcome two barriers, the vacuum barrier and that given by the insulator. Depending on the applied bias voltage the electrons either tunnel through both barriers and the adsorbate directly (1), or they are localized on the molecule before passing the second barrier (2, *resonant tunneling*). While the first case corresponds to ‘topographic imaging’ of the molecular structure for the second case further effects can dominate which were intensely studied by STM and AFM [145]. For instance, resonant inelastic tunneling (IET) [111] becomes very efficient due to the long life times of the resonances. Furthermore, it is possible to determine and control the charge state of adsorbates [see also Sec. 1.3.3]. Also, surfaces of constant LDOS of the molecular frontier orbitals [28, 259] can be visualized by tuning the bias voltages to resonance peaks within 1D STS spectra [see Sec. 6.3]. Finally, the coulomb barrier might be investigated, which becomes visible as small shifts between the energies measured by STS for a molecule on a thin insulating film, and that theoretically expected [143, 260, 261]. Finally, for NaCl/Cu(111), an interface state can be monitored, which is related to the Cu(111) surface state, surviving the deposition on the thin film.

Chapter 5

Mechanical Properties of Single Molecules

The concrete geometry of a molecule on a surface, as discussed in Sec. 4.3 is determined by the nature and strength of the molecule-surface interactions in combination with the molecule's flexibility, governing the complete mechanical behavior of the molecule on the surface [see Sec. 4.4]. In this concern, the local character of SPM based investigation tools offers a powerful technique to investigate and quantify the elastic properties of single molecules on a surface [96]. Several studies about molecular motion have been presented, particularly also concerning rolling motion for which the molecular elasticity is particularly important [262–267]. The present chapter deals with the mechanical properties of single porphyrin molecules investigated by means of combined 3D tuning fork based $\Delta f/I_t(x, y, z)$ spectroscopy. On that basis, a controlled manipulation process was established via the directed rotation of single molecules. Results are published in [157].

5.1 Adsorption Geometry

In order to obtain single molecules on the Cu(111) surface, the H₂TBCPP compound was deposited onto a cool substrate ($T \approx -190$ K) like described in Sec. 3.1. By looking at the STM image in Fig. 5.1 (a) one finds that the individually adsorbed molecules are oriented along the [110]- or an equivalent symmetry direction of the Cu(111) surface. The contrast of each molecule is dominated by two brighter and two darker spots, which correspond to the di-tert-butylphenyl, and dicyanophenyl groups, respectively. This shape is known as the so called saddle-conformation which results from a conformational change upon adsorption [268], schematically illustrated in Fig. 5.1 (b). The two dicyanophenyl-groups are slightly rotated out of the plane through the molecular center, so that one CN group remains closer towards the substrate compared to the other. Furthermore, the two whole dicyanophenyl

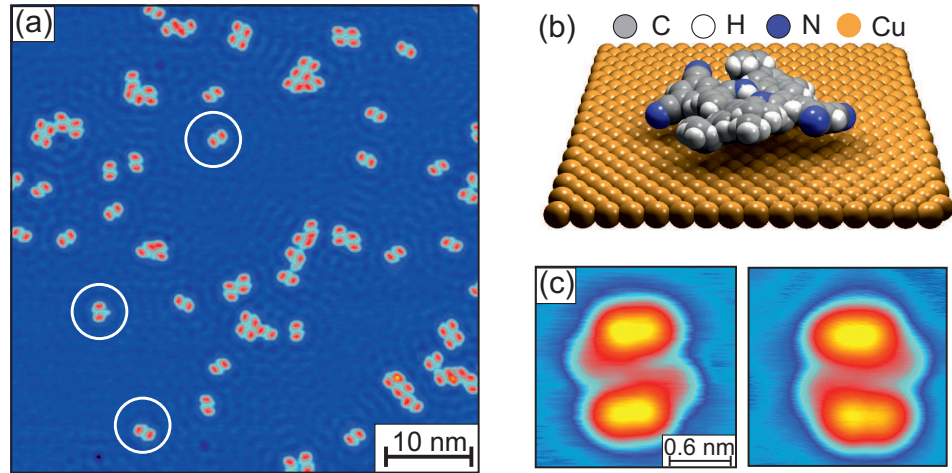


Figure 5.1: H₂TBCPP molecule on Cu(111). (a) Constant current overview image showing individually adsorbed porphyrin molecules oriented along three directions of the substrate, exemplarily marked by the white circles. (b) Scheme of the saddle-conformation, from [157]. (c) High resolution of two enantiomers. **Parameters:** (a) $U_{\text{bias}}=50$ mV, $I_t = 20$ pA ; (c1) $U_{\text{bias}}=5$ mV, $I_t = 20$ pA; (c2) $U_{\text{bias}}=5$ mV, $I_t = 20$ pA.

groups are turned towards the butylphenyl groups by either clockwise or anticlockwise rotation. Steric hindrance between the adjacent legs finally leads to a bending of the pyrrole units up- and respectively downwards by 20° to 30°. Accordingly, the C_{2v} symmetry of the porphyrin molecules in the gas phase becomes reduced to C_2 , and depending on the direction to where the two CN groups turn, two enantiomers are available for each orientation direction, exemplarily shown in Fig. 5.1 (c).

The conformational change upon adsorption is probably essentially driven by the two polar di-cyanophenyl groups. This is supported by two facts: First, the saddle conformation is mainly caused by a rotation of these functional groups upon adsorption, and secondly, similar free-base porphyrins, only functionalized with di-tert-butylphenyl groups, do not adopt the saddle-conformation [269].

5.2 Elastic Deformation

To gain more insight into the elastic properties of this molecule-surface system in the saddle conformation, 3D combined $I_t/\Delta f$ spectroscopy measurements above single porphyrins were performed at a microscope temperature of 4.8 K. The applied bias voltage during the measurement was kept in the micro volt range, and the oscillation amplitude was set to ≈ 40 pm to 60 pm. In this range, the frequency shift can still directly be approximated by the force gradient [see Eq. 1.23]. For the data collection, the grid mode like

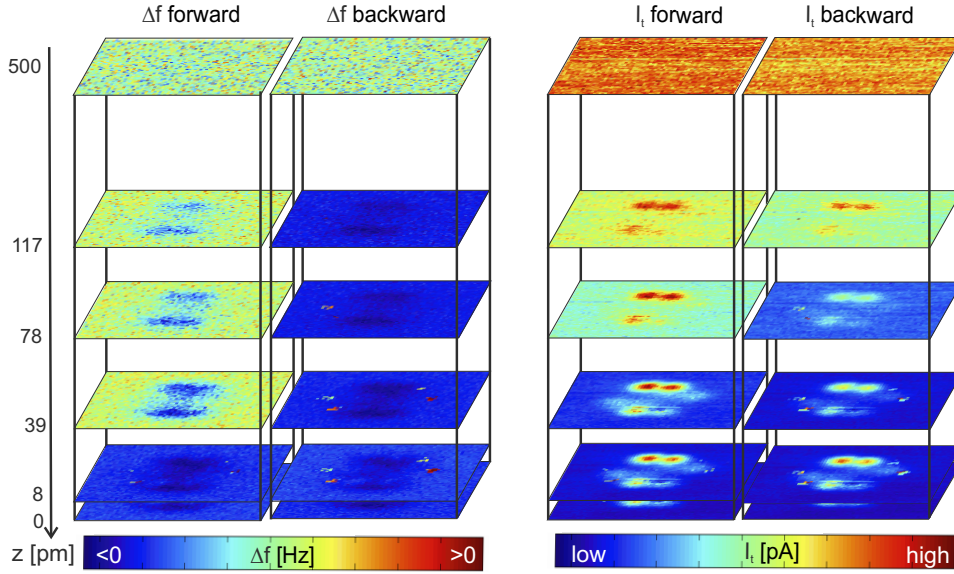


Figure 5.2: 3D combined spectroscopy of a single porphyrin on Cu(111). The data cuboids for the forward- and backward scan of $\Delta f(x, y, z)$ and respectively $I_t(x, y, z)$ are shown. $z=0$ refers to the closest recorded tip-sample separation. Parameters: 3×3 nm with 68×68 points, $A_{\text{osc}} = 50$ pm, $f_0 = 25.4$ kHz, $Q=31190$.

explained in Chap. 2 was utilized, and for each grid point, the approach and retraction curves were recorded.

The resulting data cuboids with a size of $3.2 \times 3.2 \times 0.5$ nm³ consist of $68 \times 68 \times 128$ data points. For a first rough analysis, the approach (forward) and retraction (backward) data curves of frequency shift $\Delta f(x, y, z)$ and tunneling current $I_t(x, y, z)$ data were transformed to constant height images at different z . A selection is shown in Fig. 5.2. The image at closest recorded distance is defined as $z = 0$. The colored contrast in each constant height image was optimized separately, so that the scale bare shown below only tells about trends, but not about quantitative numbers.

In the frequency shift channel the molecule generally appears at more negative Δf compared to the substrate. The fact that no atomic resolution within the molecule was obtained indicates that the distance regime at which the data set was recorded is still dominated by attractive interactions. Notably, there are four distinct points at the periphery of the molecule that indeed feature positive frequency shift. While for the forward scan direction only the very last few layers are concerned, for the backward scan direction a distance regime of $z \approx 100$ pm is covered. The same phenomena is visible in the tunneling current channel, manifesting in abrupt jumps to higher currents. Besides, the general appearance of the molecule close to the surface closely resembles that of typical constant current image, like that shown in Fig. 5.1 (d).

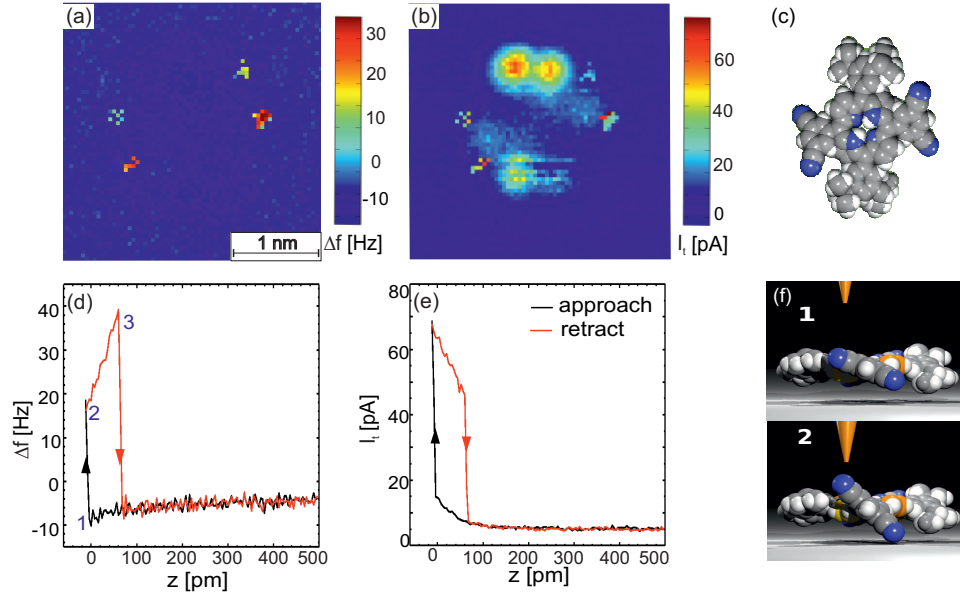


Figure 5.3: Lifting process of the cyanophenyl groups. (a) Closest recorded $\Delta f = \text{const}$ and (b) $I_t = \text{const}$ maps of the 3D spectroscopy data set. (c) Model of the molecule featuring the same orientation. (d) The $\Delta f(z)$ and (e) $I_t(z)$ -curves at the CN locations feature a hysteresis related to a lifting process. (f) Schematic drawing of the lifting process [157].

In order to shed more light on the observed $\Delta f/I_t$ - jumps, the closest recorded layers of the backward scan direction data are depicted in Figs. 5.3 (a) and (b), together with a schematic drawing of a porphyrin adopting the same orientation in Fig. 5.3 (c). By comparing the distinct locations one can see that the four features correspond to the four CN-groups.

To now explain the abrupt jumps to positive frequency shift and higher tunneling current at the CN locations as well as the hysteresis a closer look towards the corresponding $\Delta f(z)/I_t(z)$ - curves is necessary, which are shown in Fig. 5.3 (d) and 5.3 (e), respectively. Both curves feature a hysteresis loop close to $z = 0$ between the forward and backward scan with abrupt jumps in I_t and Δf , while further away from the surface they match each other, which indicates that the hysteresis loops do not correspond to any tip change. The overall shape of the $\Delta f(z)$ curves furthermore verifies the assumption that the recorded distance regime is not dominated by repulsive interactions, which correspond to frequency shifts close or even beyond the lower turning point [see Sec. 1.3.2].

For a detailed analysis, three characteristic points within the curve shapes being important for the discussion are marked by numbers. Starting far away from the surface, both I_t and Δf show a typical z - dependent behavior

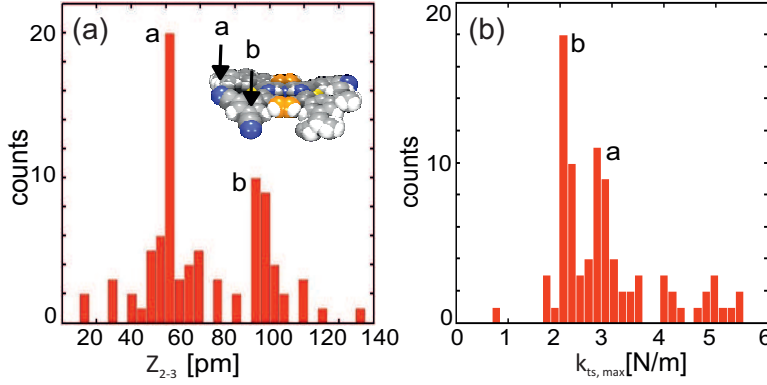


Figure 5.4: Statistical analysis of the lifting process for (a) z_{2-3} (a), and (b) $k_{\text{max,ts}}$ [157].

until position 1. Here, sudden jumps of I_t by ≈ 50 pA, and Δf by ≈ 30 Hz occur, which can be attributed to the formation of a junction between the Cu terminated tip [see Sec. 3.2] and the N atom of the targeted CN- group. Upon retraction, the bond formation is strong enough to lift the CN- group (region 2-3), which is schematically illustrated in Fig. 5.3 (f) in the lower image. Within this region the tunneling current slightly decreases, because the CN- group is disconnected from the surface and lifted up [20]. At the same time, the frequency shift increases in a discontinuous manner, suggesting a strong tip-molecule interaction [270]. The jump back at position 3 ($z \approx 100$ pm) exactly to the initial curve shape means, that the molecule recovers its initial state in the saddle conformation. This was also verified by subsequent STM images of the molecule.

Since force extractions can only be carried out in continuous regions of the entire curve, only the vertical force F_{ver} required to form the bond between the Cu tip apex and the N atom of the CN- group can be calculated. To do so, a site-dependent long-range curve, recorded together with the data set was connected to the site-dependent Δf -curve (range: 10 nm), like described in Chap. 2. Then, the integration was carried out up to point 1, accounting to $F_{\text{bond}} = -180$ pN. The corresponding stiffness of the tip-molecule junction was estimated via Eq. 4.6 and accounts to $k_{ts} \approx 1.5$ N m $^{-1}$ [see Sec. 4.4]. Hence, the bond arises due to a site-dependent force, which leads to the coordination interaction. The observed positive values of Δf are not related to the repulsive interaction regime, but to an attractive short-range interaction. It can be assumed that the abrupt jump of Δf to positive values results from drastic interaction potential modifications once the CN- group is attached.

The vertical lifting process happens independently of the targeted N atoms and is always reversible, meaning that the lifted side groups switch back to the original adsorption geometry. This was confirmed by a statistical anal-

ysis, which is shown in Fig. 5.4. For each event, the length of the hysteresis loop z_{2-3} , and the maximum Δf were extracted. This was then used to calculate the maximum tip-molecule stiffness $k_{ts, \max}$ shown in Fig. 5.4 (b). Both histograms, the one for the distribution of z_{2-3} in Fig. 5.4 (a) and that for $k_{ts, \max}$ in Fig. 5.4 (b) feature two pronounced peaks, marked by a and b. These peaks correspond to two different lifting processes. For lifts of CN- groups of type a, which initially have been closer towards the surface, z_{2-3} is longer, while the calculated $k_{ts, \max}$ is smaller (a: $z_{2-3} \approx 50$ pm, $k_{ts, \max} \approx 2.9$ N m⁻¹). The opposite applies for lifting groups of type b (b: $z_{2-3} \approx 90$ pm, $k_{ts, \max} \approx 2$ N m⁻¹).

By functionalizing the tip with a molecule, the analysis of the elastic properties of the molecule can even be extended [271]. If scanning the surface with such decorated tip, typical friction patterns are observed. They originate from the chemical reactivity between Cu and a CN group at the tip-molecule and molecule-surface site, and by the intrinsic stiffness of the molecule. Accordingly, the magnitude of the observed contrast is distance dependent, which in turn is related to the fact that the molecular tip features more degrees of freedom because the molecule can deform upon tip approach. Such measurements reveal the molecule-surface interactions, and can provide a better understanding of the impact of the structure and chemical reactivity of single molecules on nano-scale frictional properties, particularly concerning molecular machines.

5.3 Directed Rotations

If the tip is approached slightly further compared to the separations that induce a lifting of the di-cyanophenyl groups, the bond between the Cu tip apex and the N atom of the CN group can become sufficiently strong to induce a rotation of the molecule by 60°, like depicted in Fig. 5.5 . Experimentally, it was found, that already a further approach of ≈ 20 pm is sufficient. However, the exact lateral position of the tip is of utmost importance for the quality of the bond. If it is shifted laterally compared to the location of the CN- group, the bond might already not be strong enough anymore.

Hence, for a high reproducibility an accurate control of the tip-molecule junction is needed. To achieve so, an area of 100×100 pm² was defined above the location of an N atom of a CN group, which is depicted in Fig. 5.5 (a). Subsequently, about 1 to 30 $\Delta f(z)/I_t(z)$ - curves were recorded within such an area, until the lifting resulted in a rotation. In order to minimize lateral shifts due to drift or creep, atom tracking above one of the di- tert-butylphenyl groups was activated between each subsequent curves, similar to the case of recording multidimensional spectroscopy data.

The rotation direction depends on the targeted CN- group, which is illus-

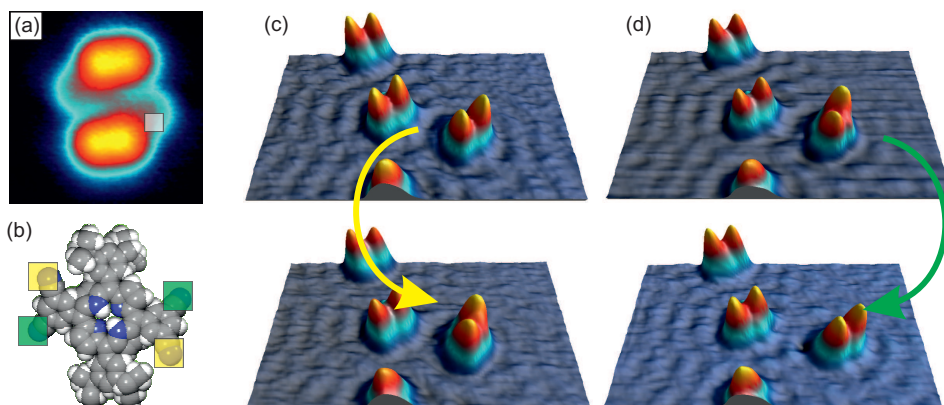


Figure 5.5: Directed rotation of single porphyrin molecules, from [157]. **(a)** Defining a small area to exactly match the CN- group, marked by the white square. **(b)** Rotations induced above CN-groups marked in yellow lead to a clockwise movement, while rotations induced above CN groups marked in green result in counterclockwise movements. **(c and d)** Examples of a clockwise and counterclockwise rotation.

trated in Fig. 5.5 (b). For the two CN- groups marked by a yellow square, a clockwise rotation is induced, while for the two groups of type b marked in green the rotation proceeds in the anticlockwise direction. This is exemplarily shown in Fig. 5.5 (c) and (d), respectively. The same rules apply for all adsorption directions and enantiomers, which was again confirmed by a statistical analysis, for which 65 molecules were manipulated. A rotation was readily induced for 47 cases corresponding to a success rate of 75%. Here, the molecules fully recovered the saddle conformation afterwards. Only for a few events the manipulation resulted in an unknown conformation ($\approx 20\%$), or unexpected tip terminations by the molecule were observed (5%).

More insights into the manipulation process can be gained by looking at Figs. 5.6 (a) and (b), depicting a typical $\Delta f(z)$ - curve and the simultaneously recorded dissipated energy $E_{\text{diss}}(z)$ corresponding to a clockwise rotation event. Important points of the curve shapes are marked by roman numbers, in order to not evoke confusion with the discussion of the pure lifting process. Neither for $\Delta f(z)$ nor for E_{diss} significant features within the approach curves are visible. In fact, both are very similar to those corresponding to a pure lifting process. The main difference towards pure lifting concerns the retraction curves. Here, the hysteresis between I and III proceeds over a much larger z - range with $z_{\text{I-III}} \approx 200$ pm. Between points I and II, roughly corresponding to the z range of a lifting process, also the curvatures still remain very similar. No features appear in the dissipation curve, and Δf increases in a discontinuous manner. This changes in the area between points II and III, accentuated in gray. This is, where the rotation is

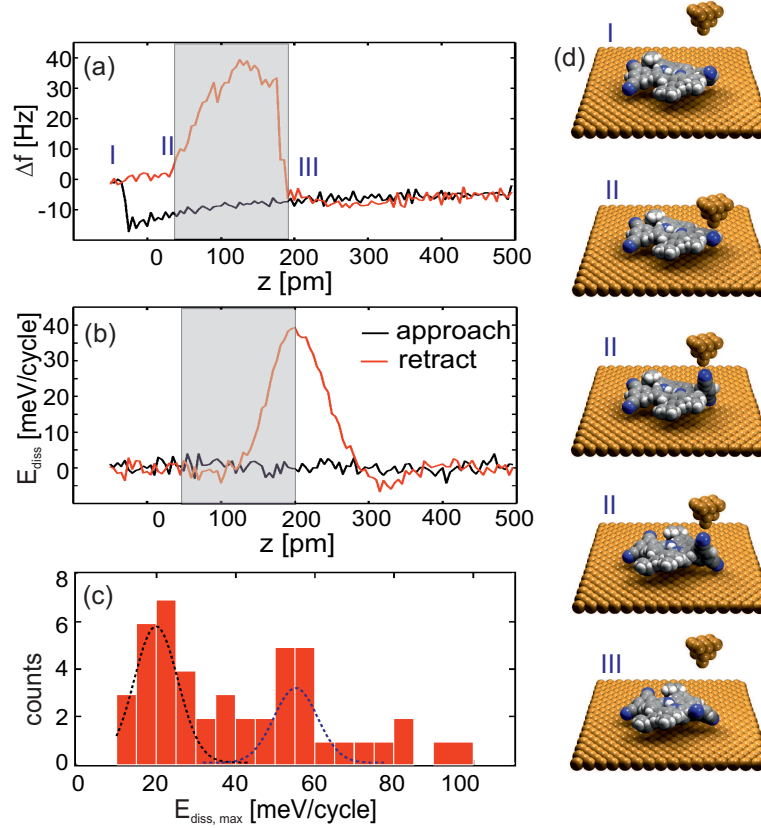


Figure 5.6: Mechanism behind the directed rotation. (a) $\Delta f(z)$ - and (b) $E_{\text{diss}}(z)$ -curves corresponding to a rotation process. (c) Statistical analysis of the dissipation of 47 rotations. (d) Schematic illustration of process behind an entire rotation. In step I the tip is approached towards the surface. Step II corresponds to the lifting process discussed before, which finally results in a rotation III, from [157].

finally induced. The gradient of Δf becomes larger, leading to a faster still discontinuous increase of Δf , until in point III a jump back to the initial curve shape is recorded. At the same time, the dissipation exhibits a pronounced peak, until it also recovers to the background dissipation in III. This peak in the backward dissipation signal is one of the main characteristics of a successful rotation process. Since the variation in the recorded tunneling current during the whole process remains rather small (in the present case below ≈ 40 pA at a bias of $U_{\text{bias}} = 300 \mu\text{V}$), it can be concluded, that the manipulation is not current induced like in previous cases [24, 265], but rather by the forces which lead to the lifting.

The mechanism behind a rotation is schematically illustrated in Fig. 5.6 (d). In analogy to the lifting process, a tip-apex-molecule junction is formed upon approach at recorded smallest tip-sample separations (first two images). Upon retraction, first the di-cyanophenyl group is lifted up, also in analogy

to the pure lifting (region I-II, third image). Because the bond is stronger in the present case, the side group does not recover its initial geometry at point II, but becomes further lifted upwards (region II-III, image 4). Upon this further lift, the second CN- group is partly decoordinated from the surface and laterally moved to a neighboring equivalent adsorption site. The movement in turn gives rise to an unstable molecule-surface junction causing stochastic changes of the tip-sample interaction [270,272]. This explains the further gradual increase of Δf in region II-III, as well as the distinct peak in the dissipation signal in the same region.

A statistical analysis of the dissipation signal of all 47 successful manipulation experiments, shown in the histogram in Fig. 5.6 (c) reveals two peaks at ≈ 20 meV/cycle and respectively ≈ 55 meV/cycle. These two peaks again correspond to the two different lifting processes of the CN- groups of type a and b. However, a more thoroughgoing analysis of the dissipation signal remains complicated, because it is influenced by the oscillation amplitude, which can either decrease or increase the mechanical stability of the created tip-molecule junction.

5.4 Summary

Even though only covering the attractive tip-sample interaction regime, 3D combined spectroscopy measurements of $I_t(z)$ and $\Delta f(z)$ enabled for a chemical recognition of specific functional groups and their exact location above the surface. Furthermore, atomic scale elastic properties could be addressed, and a partial lifting process of the dicyanophenyl groups revealed. The latter relies on the interaction between the Cu terminated tip and the functional groups leading to the formation of a tip-molecule junction. Even the small differences in the tip-molecule stiffness between two adjacent CN legs within one functional group, where one of the two groups remains closer towards the substrate compared to the other, became visible. For the two distinct lifting processes, two different tip-molecule stiffnesses and hysteresis loop lengths could be detected, which is matching theoretical expectations. s between two adjacent CN legs within one functional group, where one of the two groups remains closer towards the substrate compared to the other, became visible. For the two distinct lifting processes, two different tip-molecule stiffnesses and hysteresis loop lengths could be detected, which is matching theoretical expectations. If the molecule initially remains closer towards the surface, the hysteresis length should become higher, while the accompanied tip-sample stiffness should become smaller.

Finally, a new manipulation protocol to induce directed rotations was demonstrated. In contrast to previous results the mechanism is purely dependent on the pulling force between tip and molecule, and fully elastic. The results emphasize the capability of SPM based spectroscopy measurements to clarify

and quantify atomic-scale elastic properties even in combination with manipulation processes on surfaces. This is particularly useful for mechanically driven manipulation processes, like for instance concerning force induced chemical reactions at the atomic scale [273].

Chapter 6

Electronic Properties of Single Molecules

The electronic properties of single molecular adsorbates play a decisive role in many fundamental processes as for instance in catalysis [274], organic photovoltaics [275], and particularly also in molecular electronics. As it was intensively discussed in Chap. 4, the performance of organic based devices is strongly dominated by the electronic structure at interfaces, for instance between the molecules and metal electrodes [143, 246, 276]. The partial energy alignment and eventually occurring charge transfer significantly modify the electronic structure of both the molecule and substrate. In organic multilayer configurations, this affects the intermolecular charge transfer within the layer as well.

STM and AFM offer unique tools to visualize characteristic properties of adsorbed molecules on the sub-nanometer scale, such as the local adsorption geometry or the electronic structure of the frontier orbitals [STS] [28]. In contrast to STM probing the LDOS at the Fermi level, AFM based local bias spectroscopy is sensitive towards the total electron density. Thus, by recording local bias spectroscopy data sets and generating LCPD maps, the local electrostatic potential variations become accessible, which can be connected towards charge (re-) distributions at the molecule-substrate interface. Several recent reports about metal-molecule contacts focused on the bond formation between molecules and metal atoms [134, 143, 277]. Furthermore, the charge state of single adsorbates was determined, and molecular switches based on charge state control were suggested [22, 31, 199, 200, 278]. In these studies however, the molecules were decoupled from the underlying metallic surface by thin insulating layers, so that the intrinsic electronic structure of the molecules was only weakly perturbed by the presence of the substrate. Accordingly, comparative density functional theory (DFT) calculations can be carried out for the adsorbates in gas phase. However, if the molecules are adsorbed on a semiconductor or metal where the molecule-surface in-

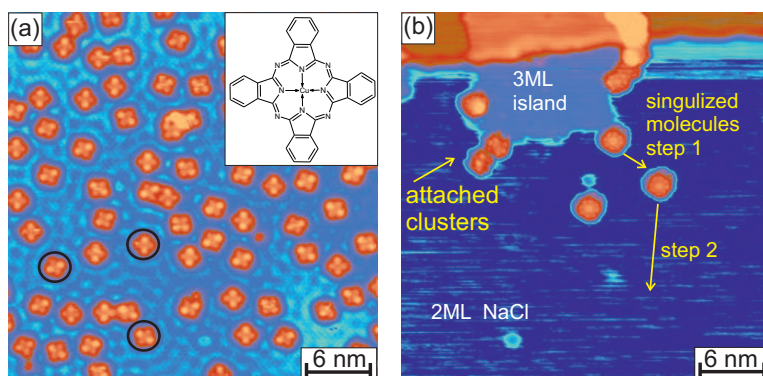


Figure 6.1: CuPc and sample morphology of CuPc on Cu(111) and NaCl(2ML)/Cu(111). **(a)** Individual CuPcs on Cu(111) aligned along three orientation, marked by circles. Inset: Chemical structure of CuPc. **(b)** CuPc on NaCl(2ML)/Cu(111). The molecules initially cluster at steps/kinks between second and third ML so that a two step post deposition manipulation method needed to be established (see main text). **Parameters:** (a): $U_{\text{bias}} = -200$ mV, $I_t = 30$ pA, (b): $U_{\text{bias}} = -1.7$ V, $I_t = 10$ pA.

teractions become much stronger, this situation drastically changes. The formation of new chemical bonds and/or charge transfer between adsorbate and surface can induce stronger changes in the molecular arrangement, and hence charge redistribution. Accessing these on the single-molecular level could considerably improve the understanding about the metal-organic interface and hence lead to improved devices.

The present chapter is concerned with the electronic properties of single CuPc molecules on a metallic Cu(111) substrate, either directly, or on top of a decoupling overlayer, namely a NaCl(001) bilayer. A comparison of these strongly and weakly interacting substrates reveals structural distortions induced by the adsorption. Furthermore, while the molecule's electronic structure on the thin insulating film is known to be only weakly perturbed [28], on Cu(111) it becomes strongly modified due to the strong adsorption interactions, meaning that electrons are transferred from the metal to the molecules. In fact, it is well known that metal PC's frequently capture charge from noble metal surfaces [242, 279]. In case of CuPc on Cu(111), the overall charge transfer from the substrate to the molecule accounts to about two electrons [201, 280]. Comparing LCPD maps reveals the (re-) distribution of charge in these two systems. All experimental data were supported by density functional theory (DFT) calculations which have been performed and provided by Ali Sadeghi from the group of Prof. Goedecker at the University of Basel. For a deeper insight into the calculations the reader is referred to [64].

6.1 Sample Morphology

Figure 6.1 (a) shows, that the CuPc molecules already initially individually adsorb on the Cu(111) surface adopting a flat lying orientation along the symmetry directions of the Cu(111) substrate, which are marked by circles. On the other hand, the much higher mobility of molecules on NaCl(2ML)/Cu(111) [see Fig. 6.1 (b)] complicates the adsorption process. As a consequence of performing the deposition while cooling the manipulator, as it was described in Chap. 3, no single molecules on free NaCl terraces could be found [see also Sec. 3.4.4]. Due to their high mobility on this substrate, they rather attach to steps or kinks between second and third ML like at the left edge of the third monolayer NaCl island in the upper corner in Fig. 6.1 (b), or completely diffuse towards the Cu(111) substrate, so that a post-deposition manipulation procedure needed to be established in order to obtain single molecules on the NaCl bilayer.

In **step 1** the molecules are detached from the clusters. For this purpose, the tip is scanned across the step edge where the clusters are attached. Meanwhile, the p-gain is repeatedly slightly exaggerated for small time periods (≈ 1 s) in order to loosen single molecules from the clusters. Note, that the feedback saturation can also easily lead to a local destruction of the thin film third ML island, so that the respective adjustments need to be carefully chosen. In any case, decoupled molecules remain very close to the cluster and/or step [right side of the 3rd ML island].

For this reason, in **step 2** they are laterally manipulated towards the free terraces. To do so, the tip is positioned above a single loosened molecule. Then, the feedback is switched off and the tip is approached to a certain threshold distance (typically ≈ 200 pA to 300 pA at ≈ 1 V to 1.5 V). From this position, it is scanned laterally, whereas the molecule follows its movement [see Sec. 1.3.3]. There is a quite high probability to pick up the molecules during the manipulation process, which can be notably reduced by functionalizing the tip with a molecule on purpose before [134]. In contrast to previous manipulation experiments on thin films [22, 143], no IET process was initiated.

6.2 Adsorption Geometry

As was discussed in Sec. 4.3 the local adsorption geometry is a distinct indicator of the present molecule-surface interaction. Estimated from the DFT calculations the interaction energy per molecule for CuPc on NaCl(2ML)/Cu(111) accounts to ≈ 2 eV/molecule, while on Cu(111) it is considerably higher, namely 6.58 eV/molecule^I. Due to the smooth border-

^IDepending on the utilized functional the calculated adsorption energies might differ from each other, as for instance for CuPc on Cu(111), where other authors reported about

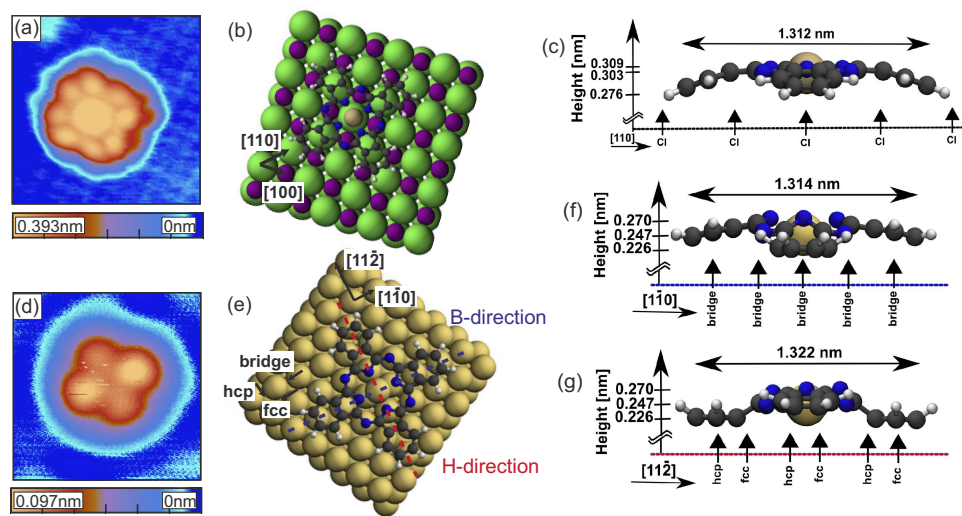


Figure 6.2: Adsorption geometry of individual CuPc on (a-c) NaCl(2ML)/Cu(111), and (d-f) Cu(111). (a,d) Constant current STM images, (b,e) top views and (c,f) Atomic positions integrated into a 2D horizontal side view along the molecular axes through opposing pairs of benzo-pyrrole lobes, emphasizing the non planar configurations. **Parameters:** (a): $U_{\text{bias}} = -1.7$ V, $I_t = 4$ pA, (d): $U_{\text{bias}} = -200$ mV, $I_t = 30$ pA.

line between chemisorption and physisorption [see Sec. 4.3] the categorization of a certain adsorption process is not always doubtless. However, in agreement to [201, 242] the adsorption of CuPc on Cu(111) might be described as a chemisorptive process, while the adsorption of aromatic molecules on NaCl(2ML)/Cu(111) is commonly addressed as physisorption [28, 145, 259]. In Fig. 6.2 (a) an STM image of a single CuPc molecule adsorbed on NaCl(2ML)/Cu(111) is shown. The contrast is dominated by the LUMO resonance, which will be discussed in the next section. First of all note that the fourfold symmetry of the molecule in gas phase is preserved, which is a first indicator for rather weak molecule-surface interactions. The DFT calculated adsorption geometry in the lowest energy configuration, shown in Fig. 6.2 (b), reveals that in the energetically most favorable conformation the central Cu atom is placed above a Cl^- ion. Due to the coinciding fourfold symmetry of the NaCl layers and the molecule, all four benzo-pyrrole rings are located at equal adsorption sites. The separation between the surface and a parallel plane through the central Cu atom accounts to ≈ 3.0 Å, still in the range for physisorption. Atomistic positions plotted perpendicular to an axis along the molecule through two opposing benzo-pyrrole rings, and integrated into a 2D horizontal side view, are shown in Fig. 6.2 (c). They

4.21 eV and 5.08 eV depending on the functional [280]. Also other computed properties like the energy levels are strongly functional dependent [281].

reveal, that all four rings are bent towards the substrate by almost 0.3 \AA . The appearance of CuPc molecules adsorbed on the Cu(111) strongly differs from the first case: one pair of opposing benzo-pyrrole rings appears brighter than the other, so that the symmetry of the molecule in the STM in Fig. 6.2 (d) becomes reduced to twofold D_{h2} symmetry. Such symmetry reductions, frequently observed for metal Pc's [189, 193, 282, 283], are due to the different symmetries of the molecule and substrate in combination with strong molecule-surface interactions [see Sec. 4.3]. In our case, the sixfold- and fourfold symmetries of the Cu(111) surface layer and CuPc, respectively, are only compatible with a twofold symmetry of the combined system.

The DFT calculated adsorption geometry shown in Fig. 6.2 (e) reveals that the central Cu atom in the lowest energy configuration in this case is placed on a bridge position of the substrate, which is in accordance to [201]. The axes along which the benzopyrrole rings proceed are again aligned with symmetry axes of the substrate, i.e. the $\langle 1\bar{1}0 \rangle$ and $\langle 1\bar{1}2 \rangle$ or equivalent directions. The two rings aligned along the the $[1\bar{1}0]$ direction are located above bridge sites of the surface, which is denoted as *B-direction*. Accordingly, the perpendicular direction $[1\bar{1}2]$, along which the other two rings lie above hollow sites, is denoted as *H-direction*.

Two side views, generated in the same way as for the NaCl case along the H- and B- direction are presented in Fig. 6.2 (f). Note, that the central Cu atom is located significantly below the surrounding N atoms at a distance of 2.5 \AA from the topmost surface layer. Moreover, peripheral H atoms are raised above the benzol rings. The two rings along the B-direction mostly stay in the horizontal plane through the central Cu atom, while those along the H-direction are bent considerably more. Accordingly, this result also shows that the two brighter maxima in Fig. 6.2 (b) correspond to the benzopyrrole wings along the B-direction. Finally, one other notable asymmetry is given by the fact, that the two local adsorption sites of the benzo-pyrrole rings above substrate hollow-sites differ from each other. One is an hcp-, and the other an fcc-hollow site.

6.3 Electronic Structure

The most important orbitals for STS measurements are given by the frontier orbitals, as they are closest to the Fermi level. For CuPc in gas phase, the HOMO and LUMO are given by the a_{1u} and by the degenerate e_g orbitals, respectively, and are shown in Fig. 6.3 (a). Both degenerate e_g orbitals together, each located around one pair of opposing benzo-pyrrole rings, as well as the a_{1u} orbital, exhibit fourfold symmetry. Because CuPc features an odd number of electrons, another important orbital concerns a singly occupied molecular orbital (SOMO), given by the $b_{1g_{up}}$ [200, 281], which is more strongly localized around the molecular center. However, this orbital

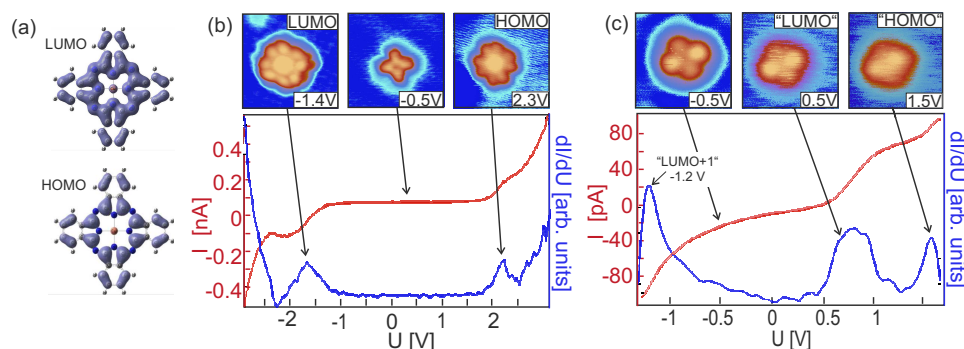


Figure 6.3: Electronic structure of CuPc investigated by STS. **(a)** DFT calculated LUMO and HOMO for the free molecule. **(b,c)** STS spectra recorded above the central Cu atom of CuPc on Cu(111) (b) and NaCl(2ML)/Cu(111) (c). Typical STM images at the bias voltages, corresponding to the resonances, and one within the interval between HOMO and LUMO are shown above. **Parameters:** (b): LUMO: $U_{\text{bias}} = -1.7$ V, $I_t = 4$ pA, GAP: $U_{\text{bias}} = -500$ mV, $I_t = 20$ pA, HOMO: $U_{\text{bias}} = 2.3$ V, $I_t = 20$ pA; (c) ‘LUMO’: $U_{\text{bias}} = 500$ mV, $I_t = 20$ pA, ‘HOMO’: $U_{\text{bias}} = 1.5$ V, $I_t = 20$ pA.

was not resolved in the STS measurements shown here.

STS spectra were recorded above the central Cu atom of the molecule on both substrates, advancing as described in Sec. 1.3.2. The spectrum for CuPc on NaCl(2ML)/Cu(111) shown in Sec. 6.3 (b). Two molecular resonances derived from respective orbitals are clearly visible and can be attributed towards the HOMO (≈ 2.3 V) and the LUMO (≈ -1.4 V), which is in good agreement with [200]. Typical STM images, recorded at the bias voltages corresponding to the resonances are shown above the spectra. The fact, that the LUMO dominated image maintains the fourfold symmetry of the molecule in gas phase indicates, the degeneration is not lifted upon adsorption. This in turn suggests that the electronic structure becomes only weakly perturbed here, as generally expected for organic molecules on thin insulating films. Furthermore, an image corresponding to a bias voltage between the two resonances, so that the contrast is dominated by the charge distribution close to the Fermi-level, is shown. In the latter, the molecular core features a charge depletion area (small dark dot in the middle).

The actual situation changes if CuPc is adsorbed on Cu(111), which is shown in Fig. 6.3 (c). Despite the short life times of molecular resonances on metal surfaces, three peaks are visible. The occurring charge transfer furthermore complicates the terminology of HOMO and LUMO, as in this case the combined system needs to be regarded. Nevertheless, in good agreement with previous photo electron spectroscopy (PES) [242], and SPM studies based on Scanning Noise Spectroscopy (SNS) [201], three resonances are detected. In the following, the assignment of molecular orbitals to these resonances will be based on that for the free molecule. The first resonance at 1.5 V can be

associated with the new ‘HOMO’. Compared to the spectrum on NaCl, it is shifted towards lower energy by ≈ 0.8 V, again verifying that the ionization energy and hence the binding energy is higher on Cu(111).

The second much broader peak at this bias polarity at 0.5 V to 0.7 V corresponds to the ‘LUMO’. The fact, that it is shifted across the Fermi level tells, that this orbital becomes (partially) filled upon adsorption. In this manner the degeneration of the original LUMO orbitals breaks down, and a quadrupole moment is induced [242] as a consequence of the asymmetric adsorption geometry. It is known, that the overall charge transfer from Cu(111) to CuPc accounts to ≈ 2 electrons [201]. The last resonance, also appearing at negative bias polarity, corresponds to a bias voltage of ≈ -1.2 V. It corresponds to the former ‘LUMO+1’.

Again, STM images recorded at the respective bias voltages are shown above the spectra in Fig. 6.3. The image corresponding to the ‘HOMO’ resonance appears more or less as structureless protrusion, which is in agreement with [284]. The images recorded at a bias voltage between the resonances attributed to ‘HOMO’ and ‘LUMO’, as well as the one corresponding to the F- ‘LUMO’ appear with twofold symmetry, and with a depression at the location of the central Cu atom, but in this case less pronounced compared to CuPc on NaCl(2ML)/Cu(111).

6.4 Local bias spectroscopy measurements

The strong molecule-substrate interactions of CuPc on Cu(111) and the resulting charge transfer suggest, that the local electrostatic potential variation and distribution of charge inside the molecules are affected as well. This is analyzed by means of 3D local bias spectroscopy measurements [see Sec. 1.3.2] mapping the LCPD as a function of the lateral position above the surface at constant height. The obtained sub-nanometer scale LCPD maps can be directly connected towards the local dipole moments induced by the local electric field between tip and molecule/surface [see Sec. 1.2.1], and thus should give thorough information about the adsorption interactions.

Experiment

In Fig. 6.4 (a) the LCPD map of CuPc on NaCl(2ML)/Cu(111) is depicted. Similar to the STM data, the fourfold symmetry of CuPc in the gas phase is preserved. The contrast above the molecule is shifted to lower LCPD values compared to the substrate, and the overall maximal shift

$$\Delta U_{\text{LCPD}}^{\text{NaCl,max}} = (U_{\text{LCPD}}^{\text{NaCl}} - U_{\text{LCPD}}^{\text{CuPc}})_{\text{max}} \approx 80 \text{ mV}.$$

On the other hand, the maximum contrast modulation between the benzo pyrrole rings and center within the molecule

$$\Delta U_{\text{LCPD}}^{\text{NaCl,mol}} = U_{\text{LCPD}}^{\text{max}} - U_{\text{LCPD}}^{\text{min}} \approx 60 \text{ mV},$$

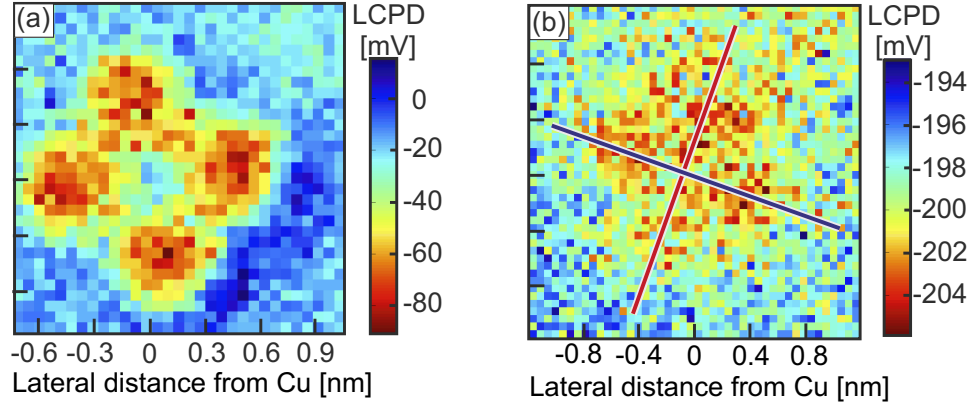


Figure 6.4: LCPD maps of CuPc on (a) NaCl(2ML)/Cu(111), and (b), extracted from 3D local bias spectroscopy measurements. For (b) the red and blue line indicate the H- and B- direction, to guide the eye. While the LCPD map measured for CuPc on NaCl(2ML)/Cu(111), the fourfold symmetry is again preserved, on the Cu(111) one finds, that not even twofold symmetry is visible. While the rings along the B-direction feature similar contrast, one of the H-direction rings appears brighter than the other. **Parameters:** (a) $1.8 \times 1.8 \text{ nm}^2$ with 32×32 points, recorded 80 pm below set point $U_{\text{bias}} = -500 \text{ mV}$ / $I_t = 20 \text{ pA}$, $A_{\text{osc}} = 70 \text{ pm}$, bias interval: -400 mV to 400 mV by 128 points. (b) $2.4 \times 2.4 \text{ nm}^2$ with 43×43 points, recorded 20 pm above set point $U_{\text{bias}} = -150 \text{ mV}$ / $I_t = 30 \text{ pA}$, $A_{\text{osc}} = 70 \text{ pm}$, interval: $U_{\text{bias}} = -300 \text{ mV}$ to 500 mV by 128 points;

with a pronounced peak above the central Cu atom, which appears at more positive LCPD than the benzo-pyrrole rings. This is in analogy to the contrast of the constant current STM images recorded at a bias voltage within the gap region, like depicted with the STS spectra in Fig. 6.3.

On the other hand, when CuPc is adsorbed on Cu(111), a completely different LCPD map is found, shown in Fig. 6.4 (b). For the present data set, the overall LCPD shift between molecule and substrate is smaller than for CuPc on NaCl(2ML)/Cu(111), i.e. $\Delta U_{\text{LCPD}}^{\text{Cu,max}} \approx 10 \text{ mV}$. It should be noted, that the tip could not be approached closer towards the surface for this measurement, which is due to the fact that the old sensor type was used. Here, the tunneling current was limited to max. $\pm 100 \text{ pA}$ in order to avoid cross talk between the two signals. Still, small signal in the dissipation signal was measured for CuPc on Cu(111), which will be discussed in appendix B.

Again, the benzo-pyrrole rings appear at more negative values compared to the substrate, while the central Cu atom features more positive U_{LCPD} , but less pronounced as for the NaCl case. Hence, also the overall contrast modulation within the molecule of $\Delta U_{\text{LCPD}}^{\text{Cu,mol}} = 2 \text{ mV}$ to 3 mV is found to be much smaller than for the NaCl case. Moreover and more importantly, the LCPD map neither preserves a clear four-fold nor two-fold symmetry. While the two rings along the B-direction feature similar contrast (red line), one

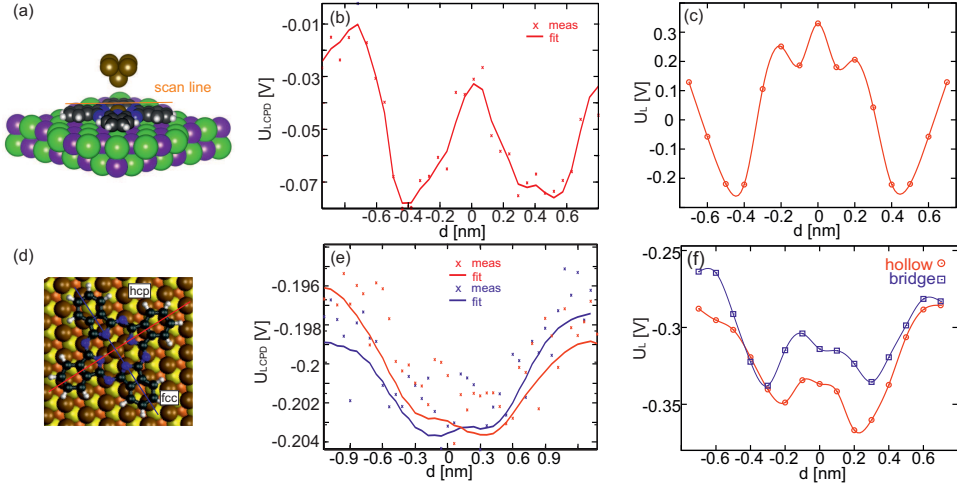


Figure 6.5: Comparison of the LCPD maps with DFT calculations via two dimensional cuts along the direction of opposing benzo-pyrrole lobes for NaCl (a-c) and Cu(111) (d-f). a,d Definition of the scan directions for the line plots. b,e Experimental LCPD lines extracted from the data shown in Fig. 6.4. (c,f) DFT calculated difference U_L between the LCPD and the macroscopic CPD, see Methods. d refers to the lateral distance from the central Cu atom.

of the rings along the H-direction features brighter contrast than the other (blue line).

Because the maximum tunneling current for both measurements was in the range of $\approx \pm 100$ pA, it can be concluded that the tip-sample distance for the recording of data on the thin insulating layer was slightly smaller than on the metal surface, which makes quantitative comparison of the obtained values difficult. Furthermore, different tips were used for the two experiments, which influences the absolute measured numbers as well. Yet, a comparison of the overall curvature is possible and already reveals many details about the present interactions.

Comparison with Theory

In order to support the experimental observations, *ab initio* calculations of U_{LCPD} were carried out, following the multiscale approach described in [62]. The deviation of the LCPD from its macroscopic counterpart, the CPD, i.e. $U_L = U_{\text{LCPD}} - U_{\text{CPD}}$, was calculated as a function of the lateral distance from the central Cu atom for lines across pairs of opposing benzo-pyrrole rings [see Fig. 6.5 (a) and (d)]. This quantity can be compared to the measured U_{LCPD} , keeping in mind that the latter should still contain long-range force contributions. Due to the fourfold symmetry of CuPc on NaCl(2ML)/Cu(111), one direction only needs to be regarded, while for the Cu(111) the calculations were carried out for the B- and H-direction.

The chosen line for CuPc on NaCl(2ML)/Cu(111) in Fig. 6.5 (a) proceeds along the [110]- direction through the two rings. The U_{LCPD} extracted along this line as well as the corresponding calculated U_L are qualitatively compared in Fig. 6.5 (b) and (c). The overall curvatures are in good agreement: both curves feature a strong decrease of U_{LCPD}/U_L at the locations of the benzo- pyrrole rings, while the central Cu atom appears pronounced and at much more positive values. However, the overall shift of $\Delta U_{LCPD}^{NaCl,max} \approx 80$ mV is much smaller than that calculated of $U_L^{NaCl,max} \approx 500$ mV, which is due to the averaging effect during the measurement. Furthermore, L features two smaller spots just beside the central Cu atom, which are not observed in the experimental data. It is not clear whether some not excited electron distribution around the center is responsible for these peaks in the calculated U_L . However, one has to know, that the tip-molecule distance applied for the calculations was set to 2 Å, while typical distances during SPM experiments are usually larger (≈ 5 Å to 10 Å). Yet, the overall curvatures of U_L and U_{LCPD} are in good agreement. Line plots of U_{LCPD} and $U_L(x)$ along the bridge- (red line) and hollow- (blue) site directions for CuPc on Cu(111) are shown in Fig. 6.5 (e) and (f). Again, the calculated $U_L^{Cu,max}$ is notably higher than the experimentally accessed values, but the curvatures of the measured U_{LCPD} and calculated U_L are very similar. The benzo-pyrrole rings appear at more negative U_L than the center, but the modulation between core and rings is smaller than for CuPc on NaCl(2ML)/Cu(111). Most notably, however, is that the difference between the two lobes across the hollow sites is reproduced by the calculations.

Discussion

For both substrates, Cu(111), and NaCl(2ML)/Cu(111), U_{LCPD} and U_L above the molecule shift to more negative values compared to the substrates. The reason for this observation lies in their mutual influence being in close proximity towards each other as was discussed in Sec. 4.5. On NaCl(2ML)/Cu(111) the negative shift might be explained by the occurrence of the ‘pillow’-effect, which could be partially canceled by the charge transfer on the Cu(111) substrate, where the total shift is much smaller.

Another similarity between the two systems concerns the fact that the central Cu atom appears at more positive U_{LCPD}/U_L compared to the surrounding benzo-pyrrole rings, even if this is much less pronounced on the Cu(111) surface. A phenomenological explanation goes back to the arrangement of the molecular orbitals of CuPc. In accordance to the STM data, featuring a charge depletion area at the molecular center, and an accumulation area at the rings^{II}. If the bias voltage is applied to the tip as it is in this thesis,

^{II}The fact the LUMO image in Fig. 6.3 (a) does not show such darker spot at the core is due to a further contribution of the SOMO orbital, which appears with a strong protrusion at the molecular center [285]

a more negative U_{LCPD} corresponds to a more negative charge, which is the case for the benzo-pyrrole rings. The reason, why this feature is less pronounced on Cu(111) might be due to the fact, that here, the central Cu atom is placed $\approx 0.2 \text{ \AA}$ below the surrounding N and C atoms around the core, while for NaCl it remains only $\approx 0.06 \text{ \AA}$ below the respective plane. Lastly, the differences within the U_{LCPD}/U_L contrast for CuPc on Cu(111) concerning the two lobes aligned along H-direction (red line), will be considered. Again, for an explanation the specific adsorption geometry plays a decisive role, which was presented in Sec. 6.2. It should be remembered, that one benzo-pyrrole ring adsorbs above a fcc- while the other one is located above an hcp- hollow site. This asymmetry seems to be reflected in the U_{LCPD}/U_L contrast. The hcp site is characterized by featuring an atom in the second substrate monolayer, while for the the fcc site, there is a hole. This in turn seems to give rise to different molecule-substrate interactions at the two positions, and hence to different induced dipole moments, and different U_{LCPD}/U_L contrasts.

6.5 Switching the Adsorption Conformation

Since the bias spectroscopy measurements, and the I(U) signal were simultaneously recorded as well, it is worth to have a look at the second data cuboids. Constant height images for selected applied bias voltages for the two data sets are shown in Fig. 6.6. For both scan directions the contrast was adjusted individually for each image in order to maximize the extractable information.

While for the measurement above the NaCl(2ML)/Cu(111) shown in Fig. 6.6 (a), for all bias voltages nominally the same contrast was observed, within the data on Cu(111) shown in (b) a contrast transition is clearly visible for the forward and backward sweep directions. The images related to an applied bias voltage of -500 mV appear with the same contrast as the one shown of Fig. 6.2 (d), which will be referred to as contrast 1 in the following. On the other hand, for a bias voltage of -300 mV the contrast seems to be reversed, and the pair of opposing benzo-pyrrole rings which initially appeared brighter, now appears darker. This contrast is named contrast 2. The transition on Cu(111) does not appear at a certain threshold voltage, but rather smoothly evolves over the entire range of the swept bias voltages. While for the forward sweep from '+' to '-', contrast 2 dominates for the majority of images, the opposite sweep direction is dominated by contrast 1. Accordingly, the transition is also not symmetrical for the two sweep directions. Furthermore, the contrast at the hollow site located benzo-pyrrole rings remains always more noisy or fuzzy compared to that associated to the bridge positioned rings. Note also, that for the present discussion, no differences between the fcc-hollow-and hcp-hollow adsorption sites can be

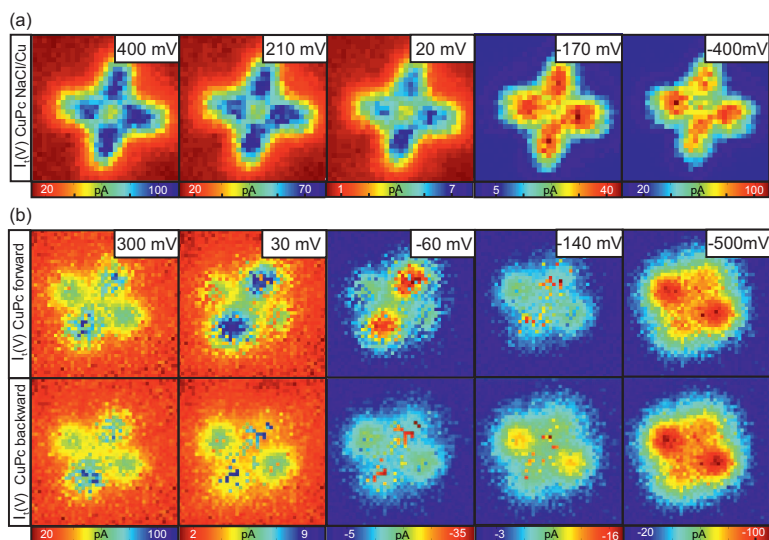


Figure 6.6: $I(U)$ maps simultaneously acquired with the local bias spectroscopy measurements for CuPc on (a) Cu(111) and on (b) NaCl(2ML)/Cu(111).

observed.

For a more thoroughgoing understanding of the contrast transition, 1D $I(U)$ - and numerically differentiated dI/dU - curves extracted above three characteristic positions are shown in Fig. 6.7. At the hollow site location (a) two phenomena can be observed: while for negative bias polarity the curves match each other, a hysteresis behavior between -150 mV and 110 mV can be observed, with two distinct jumps in the tunneling current of ≈ 10 pA in the for- and backward sweep at different bias voltages, and as distinct states in the corresponding dI/dU maps. This behavior is similar to charge state switching of single molecules on thin insulating films on metals [199, 275]. Surprisingly, in the present case, the molecules are adsorbed on a metal, where such charge state switching occurs on a much faster time scale. The second characteristic observation for $I(V)$ curves above benzo-pyrrole rings located above hollow sites concerns a telegraph noise starting at the onset of positive applied bias voltages > 0.2 V, similar to [283].

The $I(U)$ and dI/dU spectra above the molecular center shown in Fig. 6.7 (b) both feature the same characteristics, but notably smaller. The interval of the hysteresis reduces to ≈ -0.1 V to 0.1 V, and also the tunneling current jumps reduce to ≈ 5 pA. In contrast, for the curves above a bridge positioned benzopyrrole ring (c) both features disappear and the curvature resembles metallic behavior, typical for molecules that are strongly bound to metal substrates.

For an explanation of the contrast transition as well as of the observed hysteresis and telegraph, previous results on the same system need to be recalled. The adsorption conformation for CuPc on Cu(111) for higher coverages up to

6.5 Switching the Adsorption Conformation

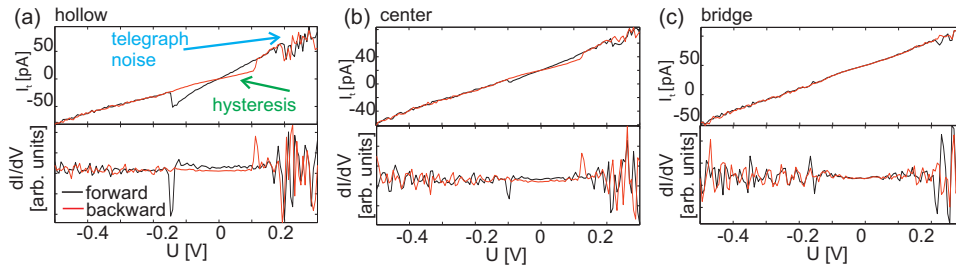


Figure 6.7: 1D $I(U)$ - and numerically differentiated dI/dU curves for CuPc on Cu(111) extracted from the 3D local bias spectroscopy measurement above a hollow site ring, a bridge site ring, and above the center. Particularly, the curves above the hollow site rings feature a hysteresis around zero bias and telegraph noise at negative bias voltage.

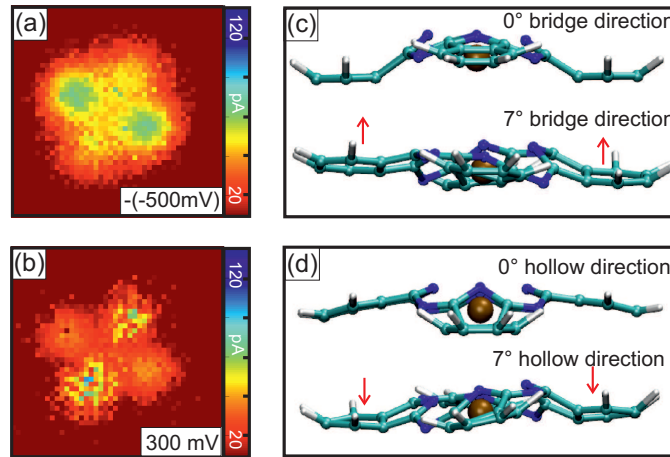


Figure 6.8: Frustrated rotation. (a,b) Images extracted from the data set shown in Fig. 6.6, but with identical color coding. (b,c) Side views of the DFT calculated adsorption geometries in the global minimum configuration and that turned by 7° . Again, the out of plane direction is rescaled by a factor of four.

1ML can differ from the global minimum configuration shown in Fig. 6.2 (d) by an angle of $\pm 7^\circ$ [197]. Such slight modifications within close packed monolayer assemblies can be understood in terms of the competing molecule-surface- and intermolecular interactions. In a recent study by Schaffert et al. it was furthermore shown that this configuration corresponds to a secondary minimum for the adsorption geometry. Indeed, induced by a one-electron inelastic tunneling process, already individual CuPc molecules on Cu(111) undergo a frustrated rotation between the global- 0°), and the secondary minimum configuration $\pm 7^\circ$ with a yield of $\approx 5 \times 10^{-7}$ events/electron at LT [201, 280]. As a consequence STM images of single CuPc molecules appear blurred, partially fuzzy, and with a telegraph noise mainly recorded at benzo-pyrrole rings positioned above hollow sites at the bias polarity for

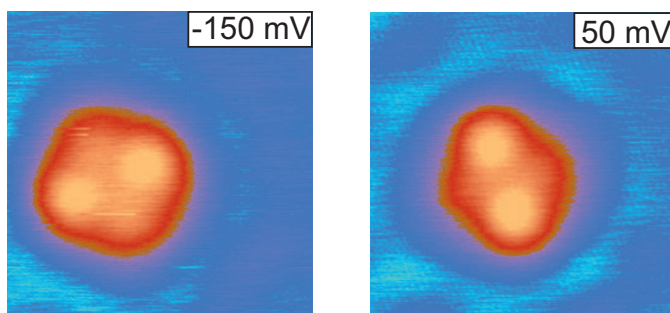


Figure 6.9: Within the bias range corresponding to the hysteresis behavior, the molecule can be switched between the two adsorption configuration induced by changes in the bias voltage. Parameters: left: $U_{\text{bias}} = -150 \text{ mV}$, $I_t = 20 \text{ pA}$, right: $U_{\text{bias}} = 50 \text{ mV}$, $I_t = 20 \text{ pA}$.

which electrons are injected into the molecules is a direct consequence of the frustrated rotations. The fact, that the hysteresis as well as the telegraph noise are mainly occurring above benzo pyrrole rings adsorbed above hollow site positions. This is again in agreement with [280], and related to the asymmetric adsorption configuration, with stronger molecule-surface interactions for the benzo-pyrrole rings adsorbed above hollow site positions. As a consequence the response of injected electrons is stronger for these rings. In this manner the telegraph noise observed here can be unambiguously attributed to frustrated rotations of single molecules as well. In order to understand the hysteresis and contrast transition, the two bias spectroscopy images at 300 mV , and -500 mV are plotted with exactly the same color coding in Fig. 6.8 (a) and (b). Compared to (a), which corresponds to the global minimum configuration, the benzo-pyrrole rings above bridge positions in image in (b) seem to bent towards the substrate, while the other two appear as if they become detached from it. To prove, whether this movement corresponds to a frustrated rotation by $\pm 7^\circ$, the respective DFT calculated top-view adsorption geometries in a side view for 0° , and exemplarily for -7° are shown in Fig. 6.8 (c) and (d). Again, the out of plane direction is rescaled by a factor of four. Indeed, upon rotation, the two benzo-pyrrole rings above bridge positions move closer towards the substrate (c) and slightly tilt out of plane. The rings above hollow site positions become tilted as well, but detach from the surface (d). In this manner, the two contrasts in STM images at different bias polarity as well as in the bias spectroscopy measurement can be clearly attributed to the contrasts of the global and secondary minimum configurations.

The hysteresis now corresponds to a bistable range where the two adsorption configurations can be switched on purpose, as illustrated in Fig. 6.9. For this, the same molecule was scanned with two different bias voltages within the bistable range. Another possibility is to inject electrons into benzo-

pyrrole rings above hollow sites. It was shown, that the switching can be induced at these sites most efficiently which is due to the fact, that they stay more closely at the surface [280]. The fact, that the switching can be induced in controllable manner gives rise to a switching probability based on a conformational change, and induced by an (single-electron) inelastic process.

6.6 Summary

The present chapter was concerned with the electronic properties of single CuPc molecules on two different substrates featuring weak [NaCl(2ML)/Cu(111)] and respectively strong [Cu(111)] molecule-surface interactions. Already a comparison of the characteristic adsorption geometries and STS spectra revealed the influence of the strong interactions on the Cu(111) surface. The observed symmetry reduction from fourfold to twofold is accompanied by a charge transfer of two electrons from the metal into the original LUMO of the molecule. The analysis of LCPD maps, and comparison with DFT calculations, furthermore allowed to thoroughly address the local electrostatic potential variations induced by the adsorption interactions as well as the redistribution of charge. For both surfaces the molecule appears at more negative values compared to the substrate which can be related to typical interface effects like the ‘pillow effect’. But, the charge transfer on Cu(111) strongly affects the electronic structure. Probably mostly outstanding is the very high sensitivity of the measured signals towards small asymmetries in the local molecule-surface interactions, like the differences between the two benzo-pyrrole rings adsorbed on a hcp- and fcc hollow site, that are related to an asymmetry within the substrate subsurface layer.

Furthermore, the simultaneously recorded current maps were investigated. A contrast transition between the contrasts of the two opposing pairs of benzo-pyrrole rings on Cu(111) could be unambiguously related towards a frustrated rotation between the global minimum (0°) and two equal secondary minima at $\pm 7^\circ$. The fact, that this switching in the adsorption geometry is bias voltage controlled establishes a controllable switching property based on the adsorption conformational change.

The results clearly demonstrate the potential of three dimensional bias spectroscopy measurements in order to reveal charge transfer processes at the single molecular level. It is envisioned, that even light induced charge transfer processes might become accessible by this technique, which could strongly help for a detailed understanding about transport mechanisms in organic based heterojunction solar cells. This will be subject to appendix A.

Conclusion

„Actio et Reactio.”

SIR ISAAC NEWTON

In physics, forces are the basic mean by which materials and their properties are characterized. Presently, in the framework of the standard model of physics all phenomena can be traced down to four basic interactions, gravitation, electromagnetic forces, as well as weak-, and strong interaction. Moreover, approaches beyond this model attempt to extend it into a unified field theory, or ‘theory of everything’ subsuming all physical phenomena under one theory.

In a similar manner, on the tiny scale of molecules on surfaces, all phenomena studied within this thesis can be ascribed to the adsorption interactions at the interface, which are all of electromagnetic origin. Even the experimental tools utilized, STM and AFM go back to interactions between a tip and surface in close proximity towards each other, because the tunneling current is a consequence of the overlap of the wave functions of tip and sample, while the frequency shift is directly connected towards the interaction forces.

The performance of spectroscopic operation modes allowing for the probing of vertical and lateral interaction forces, potential energy landscapes, local work function variations, or the visualization molecular frontier orbitals was thoroughly investigated. The influence of the finite oscillation amplitude as far as the frequency shift is concerned, was ruled out, and the two main data acquisition operation modes were compared with respect to possible measurement artifacts in Chap. 2. Continuing with experimental issues, challenges in relation to the handling of the utilized molecules were addressed, comparing two different deposition methods, and several tools which help to control the process [Chap. 3].

When it comes to the characteristics of condensed single molecules on surfaces, the major importance of the concrete local adsorption geometry as a main characteristic observable of the interaction landscape was verified in Chap. 4. By high-resolution topographic imaging, and local dynamic force spectroscopy in Chap. 5 the atomic scale elastic properties of single porphyrin molecules were revealed. Based on a lifting process, finally a directed rotational manipulation process was established, which was proven

to be fully force driven. Proceeding towards the electronic structure modification of molecules on adsorption by a combined STM-, AFM, and DFT study in Chap. 6, the influence of the strengths of interactions could be observed. If the molecules are physisorbed, the electronic structure becomes only weakly perturbed. On the other hand, charge transfer on metal surfaces can highly modify the appearance of the molecular orbitals. Mapped by 3D local bias spectroscopy measurements, the electrostatic potential variations and (re-) distribution of charge within the molecules as a consequence of the adsorption interactions were analyzed by comparing extracted LCPD maps, and supporting DFT calculations, following the multiscale approach [62], in which the LCPD is directly connected towards induced local dipole moments. Mostly outstanding is probably, that even asymmetries in the local adsorption interaction potential concerning the second substrate layer could be made visible, and that the tunneling channel gave deep insight into the inelastic tunneling induced switching of the adsorption geometry.

The presented results, show that SPM methods serve as unique investigation tools concerning fundamental questions related to molecules on surfaces. Future studies might allow to quantify molecular conductance, the basic interactions at the molecule-substrate interface, and the characteristic properties of the structures themselves. Due to the high obtainable resolution, chemical reactions might be carried out on a surface in real time, and finally, by the introduction of light, optically induced charge transfers within single molecules might become accessible, and quantifiable. This last topic will be targeted in appendix A dealing with light assisted local bias spectroscopy measurements.

Bibliography

- [1] G. E. Moore. Cramming more components into integrated circuits. *Electronics*, 38(8):114–117, 1965.
- [2] W. Lu and C. M. Lieber. Nanoelectronics from the bottom up. *Nat Mater*, 6(11):841–850, 2007.
- [3] R. P. Feynman. There’s plenty of room at the bottom. *Engineering and Science*, 23(5):22–36, 1960.
- [4] C A Mirkin and M A Ratner. Molecular electronics. *Annual Review of Physical Chemistry*, 43(1):719–754, 1992.
- [5] J. R. Heath. Molecular electronics. *Annual Review of Materials Research*, 39(1):1–23, 2009.
- [6] N. Weibel, S. Grunder, and M. Mayor. Functional molecules in electronic circuits. *Org. Biomol. Chem.*, 5:2343–2353, 2007.
- [7] B. Mann and H. Kuhn. Tunneling through fatty acid salt monolayers. *Journ. Appl. Phys.*, 42(11):4398–4405, 1971.
- [8] A. Aviram and M. A. Ratner. Molecular rectifiers. *Chem. Phys. Lett.*, 29(2):277–283, 1974.
- [9] N. J. Tao. Electron transport in molecular junctions. *Nat Nano*, 1(3):173–181, 2006.
- [10] F. Chen, J. Hihath, Z. Huang, X. Li, and N.J. Tao. Measurement of single-molecule conductance. *Annual Review of Physical Chemistry*, 58(1):535–564, 2007.
- [11] G. Binnig, H. Rohrer, Ch Gerber, and E. Weibel. Tunneling through a controllable vacuum gap. *Appl. Phys. Lett.*, 40(2):178–180, 1982.
- [12] G. Binnig, C. F. Quate, and Ch. Atomic Force Microscope. *Phys. Rev. Lett.*, 56(9):930–933, 1986.
- [13] G. Binnig, H. Rohrer, Ch Gerber, and E. Weibel. 7×7 reconstruction on si(111) resolved in real space. *Phys. Rev. Lett.*, 50:120–123, 1983.

- [14] F. J. Giessibl. Atomic Resolution of the Silicon (111)-(7 × 7) Surface by Atomic Force Microscopy. *Science*, 267(5194):68–71, 1995.
- [15] R. Wiesendanger. *Scanning Probe Microscopy and Spectroscopy - Methods and Applications*. Cambridge University Press, 1994.
- [16] Roland Bennewitz Ernst Meyer, Hans Josef Hug. *Scanning Probe Microscopy - The Lab on a Tip*. Springer Berlin Heidelberg, 2004.
- [17] C. Weiss, C. Wagner, R. Temirov, and F. S. Tautz. Direct imaging of intermolecular bonds in scanning tunneling microscopy. *JACS*, 132(34):11864–11865, 2010.
- [18] L. Gross, F. Mohn, N. Moll, P. Liljeroth, and G. Meyer. The Chemical Structure of a Molecule Resolved by Atomic Force Microscopy. *Science*, 325(5944):1110–1114, 2009.
- [19] Z.-C. Dong, X.-L. Guo, A. S. Trifonov, P. S. Dorozhkin, K. Miki, K. Kimura, S. Yokoyama, and S. Mashiko. Vibrationally resolved fluorescence from organic molecules near metal surfaces in a scanning tunneling microscope. *Phys. Rev. Lett.*, 92:086801, 2004.
- [20] Leif Lafferentz, Francisco Ample, Hao Yu, Stefan Hecht, Christian Joachim, and Leonhard Grill. Conductance of a single conjugated polymer as a continuous function of its length. *Science*, 323(5918):1193–1197, 2009.
- [21] M. Ternes, C. P. Lutz, C. F. Hirjibehedin, F. J. Giessibl, and A. J. Heinrich. The Force Needed to Move an Atom on a Surface. *Science*, 319(5866):1066–1069, 2008.
- [22] P. Liljeroth, J. Repp, and G. Meyer. Current-Induced Hydrogen Tautomerization and Conductance Switching of Naphthalocyanine Molecules. *Science*, 317(5842):1203–1206, 2007.
- [23] T. Leoni, O. Guillermet, H. Walch, V. Langlais, A. Scheuermann, J. Bonvoisin, and S. Gauthier. Controlling the Charge State of a Single Redox Molecular Switch. *Phys. Rev. Lett.*, 106:216103, 2011.
- [24] H. L. Tierney, C. J. Murphy, A. D. Jewell, A. E. Baber, E. V. Iski, H. Y. Khodaverdian, A. F. McGuire, N. Klebanov, and E. C. H. Sykes. Experimental demonstration of a single-molecule electric motor. *Nat Nano*, 6(10):625–629, 2011.
- [25] F. J. Giessibl. Atomic resolution on si(111)-(7 × 7) by noncontact atomic force microscopy with a force sensor based on a quartz tuning fork. *Appl. Phys. Lett.*, 76(11):1470–1472, 2000.

- [26] K. Kadish, R. Guilard, and K. M. Smith, editors. *The porphyrin handbook*. Academic Press, 1999.
- [27] H. J. W. Zandvliet and A. van Houselt. Scanning Tunneling Spectroscopy. *Annual Review of Analytical Chemistry*, 2(1):37–55, 2009.
- [28] J. Repp, G. Meyer, S. M. Stojkoviifmmode acutecelse éfi, A. Gourdon, and C. Joachim. Molecules on Insulating Films: Scanning-Tunneling Microscopy Imaging of Individual Molecular Orbitals. *Phys. Rev. Lett.*, 94:026803, 2005.
- [29] H. Hölscher, S. M. Langkat, A. Schwarz, and R. Wiesendanger. Measurement of three-dimensional force fields with atomic resolution using dynamic force spectroscopy. *Appl. Phys. Lett.*, 81(23):4428–4430, 2002.
- [30] B. J. Albers, T. C. Schwendemann, M. Z. Baykara, N. Pilet, M. Liebmann, E. I. Altman, and U. D. Schwarz. Three-dimensional imaging of short-range chemical forces with picometre resolution. *Nat Nano*, 4(5):307–310, 2009.
- [31] L. Gross, F. Mohn, P. Liljeroth, J. Repp, F. J. Giessibl, and G. Meyer. Measuring the Charge State of an Adatom with Noncontact Atomic Force Microscopy. *Science*, 324(5933):1428–1431, 2009.
- [32] F. Mohn, B. Schuler, L. Gross, and G. Meyer. Different tips for high-resolution atomic force microscopy and scanning tunneling microscopy of single molecules. *Appl. Phys. Lett.*, 102(7):073109, 2013.
- [33] S.-W. Hla. Scanning tunneling microscopy single atom/molecule manipulation and its application to nanoscience and technology. *Journ. Vac. Sci. & Techn. B*, 23(4):1351–1360, 2005.
- [34] O. Custance, R. Perez, and S. Morita. Atomic force microscopy as a tool for atom manipulation. *Nat Nano*, 4(12):803–810, 2009.
- [35] R. Wiesendanger, H. J. Güntherodt, G. Güntherodt, R. J. Gambino, and R. Ruf. Observation of vacuum tunneling of spin-polarized electrons with the scanning tunneling microscope. *Phys. Rev. Lett.*, 65:247–250, 1990.
- [36] U. Kaiser, A. Schwarz, and R. Wiesendanger. Magnetic exchange force microscopy with atomic resolution. *Nature*, 446(7135):522–525, 2007.
- [37] Phoenix Mars Mission. <http://www.mars-afm.ch/>. AFM on mars mission, 2007.
- [38] F. J. Giessibl. High-speed force sensor for force microscopy and profilometry utilizing a quartz tuning fork. *Appl. Phys. Lett.*, 73(26):3956–3958, 1998.

- [39] F. J. Giessibl. Advances in atomic force microscopy. *Rev. Mod. Phys.*, 75(3):949–983, 2003.
- [40] N. B. McKeown. *Phthalocyanine Materials - Synthesis, Structure and Function*. Cambridge University Press, 1998.
- [41] F. Schwabel. *Quantenmechanik*. Springer Berlin Heidelberg, 2007.
- [42] J. Bardeen. Tunnelling from a Many-Particle Point of View. *Phys. Rev. Lett.*, 6(2):57–59, 1961.
- [43] S. Blügel. Theorie der rastertunnelmikroskopie. Scriptum, http://www.fz-juelich.de/SharedDocs/Downloads/PGI/PGI-1/DE/stm_pdf.
- [44] C. J. Chen. *Introduction to Scanning Tunneling Microscopy*. Oxford University Press, Oxford, New York, 1993.
- [45] A. Baratoff. Theory of scanning tunneling microscopy methods and approximations. *Physica B+C*, 127:143–150, 1984.
- [46] C. J. Chen. Theory of scanning tunneling spectroscopy. *Journ. Vac. Sci. & Techn. A*, 6(2):319–322, 1988.
- [47] C. J. Chen. Origin of atomic resolution on metal surfaces in scanning tunneling microscopy. *Phys. Rev. Lett.*, 65:448–451, 1990.
- [48] J. Tersoff and D. R. Hamann. Theory and Application for the Scanning Tunneling Microscope. *Phys. Rev. Lett.*, 50(25):1998–2001, 1983.
- [49] J. Tersoff and D. R. Hamann. Theory of the scanning tunneling microscope. *Phys. Rev. B*, 31(2):805–813, 1985.
- [50] R. García and R. Pérez. Dynamic atomic force microscopy methods. *Surf. Sci. Rep.*, 47:197–301, 2002.
- [51] S. Morita, R. Wiesendanger, and E Meyer. *Noncontact Atomic Force Microscopy*. NanoScience and Technology. Springer, 2002.
- [52] T. R. Albrecht, P. Grütter, D. Horne, and D. Rugar. Frequency modulation detection using high-Q cantilevers for enhanced force microscope sensitivity. *Journ. Appl. Phys.*, 69(2):668–673, 1991.
- [53] L. N. Kantorovich, A. S. Foster, A. L. Shluger, and A. M. Stoneham. Role of image forces in non-contact scanning force microscope images of ionic surfaces. *Surf. Sci.*, 445:283–299, 2000.

- [54] S. Hudlet, M. Saint Jean, C. Guthmann, and J. Berger. Evaluation of the capacitive force between an atomic force microscopy tip and a metallic surface. *The European Physical Journal B - Condensed Matter and Complex Systems*, 2(1):5–10, 1998.
- [55] G. H. Enevoldsen, T. Glatzel, M. C. Christensen, J. V. Lauritsen, and F. Besenbacher. Atomic scale kelvin probe force microscopy studies of the surface potential variations on the $\text{tio}_2(110)$ surface. *Phys. Rev. Lett.*, 100:236104, 2008.
- [56] F. Bocquet, L. Nony, C. Loppacher, and T. Glatzel. Analytical approach to the local contact potential difference on (001) ionic surfaces: Implications for Kelvin probe force microscopy. *Phys. Rev. B*, 78:035410, 2008.
- [57] S. Sadewasser, P. Jelinek, C.-K. Fang, O. Custance, Y. Yamada, Y. Sugimoto, M. Abe, and S. Morita. New Insights on Atomic-Resolution Frequency-Modulation Kelvin-Probe Force-Microscopy Imaging of Semiconductors. *Phys. Rev. Lett.*, 103:266103, 2009.
- [58] S. Kawai, T. Glatzel, H.-J. Hug, and E. Meyer. Atomic contact potential variations of $\text{Si}(111)\text{-}7\times 7$ analyzed by Kelvin probe force microscopy. *Nanotechnology*, 21(24):245704+, 2010.
- [59] T. Glatzel. Measuring atomic-scale variations of the electrostatic force. In *Kelvin Probe Force Microscopy*. Springer Berlin Heidelberg, 2011.
- [60] F. Bocquet, L. Nony, and C. Loppacher. Polarization effects in non-contact atomic force microscopy: A key to model the tip-sample interaction above charged adatoms. *Phys. Rev. B*, 83:035411, 2011.
- [61] S A Burke, J M LeDue, Y Miyahara, J M Topple, S Fostner, and P Grütter. Determination of the local contact potential difference of ptdca on nacl: a comparison of techniques. *Nanotechnology*, 20(26):264012, 2009.
- [62] A. Sadeghi, A. Baratoff, S. A. Ghasemi, S. Goedecker, T. Glatzel, S. Kawai, and E. Meyer. Multiscale approach for simulations of kelvin probe force microscopy with atomic resolution. *Phys. Rev. B*, 86:075407, 2012.
- [63] A. Sadeghi, A. Baratoff, and S. Goedecker. Electrostatic interactions with dielectric samples in scanning probe microscopies. *Phys. Rev. B*, 88:035436, 2013.

- [64] A. Sadeghi. *Multiscale Approach for Simulations of Kelvin Probe Force Microscopy with Atomic Resolution*. PhD thesis, University of Basel, 2013.
- [65] J. N. Israelachvili. *Intrermolecular and Surface Forces, 3rd edition*. Elsevier, 2011.
- [66] H. C. Hamaker. The London - van der Waals attraction between spherical particles. *Physica*, 4(10):1058–1072, 1937.
- [67] J. E. Jones. On the Determination of Molecular Fields. II. From the Equation of State of a Gas. *Proceedings of the Royal Society of London. Series A, Containing Papers of a Mathematical and Physical Character*, 106(738):738, 1924.
- [68] P. M. Morse. Diatomic Molecules According to the Wave Mechanics. II. Vibrational Levels. *Phys. Rev.*, 34:57–64, 1929.
- [69] R. Pérez, M. C. Payne, I. Stich, and K. Terakura. Role of Covalent Tip-Surface Interactions in Noncontact Atomic Force Microscopy on Reactive Surfaces. *Phys. Rev. Lett.*, 78:678–681, 1997.
- [70] F. J. Giessibl. Theory for an electrostatic imaging mechanism allowing atomic resolution of ionic crystals by atomic force microscopy. *Phys. Rev. B*, 45:13815–13818, 1992.
- [71] S. Rast, C. Wattering, U. Gysin, and E. Meyer. Dynamics of damped cantilevers. *Rev. Sci. Ins.*, 71(7):2772–2775, 2000.
- [72] F. J. Giessibl and M. Tortonese. Self-oscillating mode for frequency modulation noncontact atomic force microscopy. *Appl. Phys. Lett.*, 70(19):2529–2531, 1997.
- [73] F. J. Giessibl and H. Bielefeldt. Physical interpretation of frequency-modulation atomic force microscopy. *Phys. Rev. B*, 61:9968–9971, 2000.
- [74] B. Anczykowski. How to measure energy dissipation in dynamic mode atomic force microscopy. *Appl. Surf. Sci.*, 140(3-4):376–382, 1999.
- [75] M. Bammerlin, R. Lüthi, E. Meyer, A. Baratoff, R. J. Lü, M. Guggisberg, Ch. Gerber, L. Howald, and H.-J. Güntherodt. True atomic resolution on the surface of an insulator via ultrahigh vacuum dynamic force microscopy. *Probe Microscopy*, 1:3, 1997.
- [76] M. Gauthier, L. N. Kantorovich, and M. Tsukada. Theorie of energy dissipation into surface vibrations. In E. Meyer S. Morita, R. Wiesendanger, editor, *Noncontact Atomic Force Microscopy*, chapter 19, pages 371–394. Springer Berlin Heidelberg, 2002.

- [77] H. J. Hug and Baratoff A. Measurement of dissipation induced by tip-sample interactions. In E. Meyer S. Morita, R. Wiesendanger, editor, *Noncontact Atomic Force Microscopy*, volume 1, chapter 20, pages 395–431. Springer Berlin Heidelberg, 2002.
- [78] A. Labuda, Y. Miyahara, L. Cockins, and P. H. Grütter. Decoupling conservative and dissipative forces in frequency modulation atomic force microscopy. *Phys. Rev. B*, 84:125433, 2011.
- [79] W. Denk and D. W. Pohl. Local electrical dissipation imaged by scanning force microscopy. *Appl. Phys. Lett.*, 59(17):2171–2173, 1991.
- [80] B. Gotsmann, C. Seidel, B. Anczykowski, and H. Fuchs. Conservative and dissipative tip-sample interaction forces probed with dynamic AFM. *Phys. Rev. B*, 60:11051–11061, 1999.
- [81] B. Gotsmann and H. Fuchs. The measurement of hysteretic forces by dynamic AFM. *Applied Physics A*, 72(1):S55–S58, 2001.
- [82] U. Dürig. Atomic-scale metal adhesion. In H. J. Güntherodt, D. Anselmetti, and E. Meyer, editors, *Forces in Scanning Probe Methods*, volume 286. NATO ASI Series, 1995.
- [83] N. Sasaki and M. Tsukada. Effect of microscopic nonconservative process on noncontact atomic force microscopy. *Jpn. J. Appl. Phys.*, 39:L1334–L1337, 2000.
- [84] P. Günther, Fischer, and K. Dransfeld. Scanning near-field acoustic microscopy. *Applied Physics B*, 48(1):89–92, 1989.
- [85] F. J. Giessibl. Principles and applications of the qplus sensor. In S. Morita, F. Giessibl, and R. Wiesendanger, editors, *Noncontact Atomic Force Microscopy*, volume 2, chapter 6, pages 121–142. Springer Berlin Heidelberg, 2009.
- [86] J. Rychen, T. Ihn, P. Studerus, A. Herrmann, K. Ensslin, H. J. Hug, P. J. A. van Schendel, and H. J. Güntherodt. Operation characteristics of piezoelectric quartz tuning forks in high magnetic fields at liquid helium temperatures. *Rev. Sci. Ins.*, 71(4):1695–1697, 2000.
- [87] Stefan Torbrügge, Oliver Schaff, and Jörg Rychen. Application of the kolibrisensor to combined atomic-resolution scanning tunneling microscopy and noncontact atomic-force microscopy imaging. In *PAPERS FROM THE 12th INTERNATIONAL CONFERENCE ON NONCONTACT ATOMIC FORCE MICROSCOPY*, volume 28(3), pages C4E12–C4E20. AVS, 2010.

- [88] E. N. Voloshina, Yu. S. Dedkov, S. Torbrügge, A. Thissen, and M. Fonin. Graphene on rh(111): Scanning tunneling and atomic force microscopies studies. *Appl. Phys. Lett.*, 100(24):241606, 2012.
- [89] S. Kawai, S. ichi Kitamura, D. Kobayashi, S. Meguro, and H. Kawakatsu. An ultrasmall amplitude operation of dynamic force microscopy with second flexural mode. *Appl. Phys. Lett.*, 86(19):193107, 2005.
- [90] S. Kawai and H. Kawakatsu. Atomically resolved dynamic force microscopy operating at 4.7 MHz. *Appl. Phys. Lett.*, 88(13):133103, 2006.
- [91] S. Kawai, F. Rose, T. Ishii, and H. Kawakatsu. Atomically resolved observation of the quenched Si(111) surface with small amplitude dynamic force microscopy. *Journ. Appl. Phys.*, 99(10):104312, 2006.
- [92] S. Kawai, T. Glatzel, S. Koch, B. Such, A. Baratoff, and E. Meyer. Systematic Achievement of Improved Atomic-Scale Contrast via Bimodal Dynamic Force Microscopy. *Phys. Rev. Lett.*, 103:220801, 2009.
- [93] S. Kawai, T. Glatzel, S. Koch, B. Such, A. Baratoff, and E. Meyer. Time-averaged cantilever deflection in dynamic force spectroscopy. *Phys. Rev. B*, 80:085422, 2009.
- [94] Y. Sugimoto, P. Pou, M. Abe, P. Jelinek, R. Perez, S. Morita, and O. Custance. Chemical identification of individual surface atoms by atomic force microscopy. *Nature*, 446(7131):64–67, 2007.
- [95] S. Kitamura and M. Iwatsuki. High-resolution imaging of contact potential difference with ultrahigh vacuum noncontact atomic force microscope. *Appl. Phys. Lett.*, 72(24):3154–3156, 1998.
- [96] R. Pawlak, S. Kawai, S. Fremy, T. Glatzel, and E. Meyer. Atomic-Scale Mechanical Properties of Orientated C60 Molecules Revealed by Noncontact Atomic Force Microscopy. *ACS Nano*, 5(8):6349–6354, 2011.
- [97] J. E. Sader and Y. Sugimoto. Accurate formula for conversion of tunneling current in dynamic atomic force spectroscopy. *Appl. Phys. Lett.*, 97(4):043502, 2010.
- [98] Y. Sugimoto, P. Jelinek, P. Pou, M. Abe, S. Morita, R. Perez, and O. Custance. Mechanism for Room-Temperature Single-Atom Lateral Manipulations on Semiconductors using Dynamic Force Microscopy. *Phys. Rev. Lett.*, 98:106104, 2007.
- [99] Y. Sugimoto, K. Miki, M. Abe, and S. Morita. Statistics of lateral atom manipulation by atomic force microscopy at room temperature. *Phys. Rev. B*, 78:205305, 2008.

BIBLIOGRAPHY

- [100] R. Pawlak, S. Kawai, S. Frey, T. Glatzel, and E. Meyer. High-resolution imaging of C₆₀ molecules using tuning-fork-based non-contact atomic force microscopy. *Journ. Phys.: Cond. Mat.*, 24(8):084005+, 2012.
- [101] F. E. Olsson, M. Persson, J. Repp, and G. Meyer. Scanning tunneling microscopy and spectroscopy of nacl overlayers on the stepped cu(311) surface: experimental and theoretical study. *Phys. Rev. B*, 71:075419, 2005.
- [102] N. D. Lang. Apparent barrier height in scanning tunneling microscopy. *Phys. Rev. B*, 37:10395–10398, 1988.
- [103] L. Olesen, M. Brandbyge, M. R. Sørensen, K. W. Jacobsen, E. Laegsgaard, I. Stensgaard, and F. Besenbacher. Apparent Barrier Height in Scanning Tunneling Microscopy Revisited. *Phys. Rev. Lett.*, 76:1485–1488, 1996.
- [104] T. König, G. H. Simon, H. P. Rust, and M. Heyde. Work Function Measurements of Thin Oxide Films on Metals: MgO on Ag(001). *J. Phys. Chem. C*, 113(26):11301–11305, 2009.
- [105] F. Mohn, L. Gross, N. Moll, and G. Meyer. Imaging the charge distribution within a single molecule. *Nat Nano*, 7(4):227–231, 2012.
- [106] R. M. Feenstra, Joseph A. Stroscio, and A. P. Fein. Tunneling spectroscopy of the Si(111)2 × 1 surface. *Surf. Sci.*, 181:295–306, 1987.
- [107] J. Klier and R. Berndt. Scanning tunneling spectroscopy of Na on Cu(111). *Phys. Rev. B*, 65:035412, 2001.
- [108] F. E. Olsson, S. Paavilainen, M. Persson, J. Repp, and G. Meyer. Multiple charge states of ag atoms on ultrathin nacl films. *Phys. Rev. Lett.*, 98:176803, 2007.
- [109] D. E. Barlow and K. W. Hipps. A Scanning Tunneling Microscopy and Spectroscopy Study of Vanadyl Phthalocyanine on Au(111): the Effect of Oxygen Binding and Orbital Mediated Tunneling on the Apparent Corrugation. *The Journal of Physical Chemistry B*, 104(25):5993–6000, 2000.
- [110] V. A. Ukraintsev. Data evaluation technique for electron-tunneling spectroscopy. *Phys. Rev. B*, 53:11176–11185, 1996.
- [111] B. C. Stipe, M. A. Rezaei, and W. Ho. Single-Molecule Vibrational Spectroscopy and Microscopy. *Science*, 280(5370):1732–1735, 1998.

- [112] L. J. Lauhon and W. Ho. Single-molecule vibrational spectroscopy and microscopy: Co on cu(001) and cu(110). *Phys. Rev. B*, 60:R8525–R8528, 1999.
- [113] M. A. Lantz, H. J. Hug, R. Hoffmann, P. J. A. van Schendel, P. Kappenberger, S. Martin, A. Baratoff, and H. J. Güntherodt. Quantitative Measurement of Short-Range Chemical Bonding Forces. *Science*, 291(5513):2580–2583, 2001.
- [114] R. Hoffmann, L. N. Kantorovich, A. Baratoff, H. J. Hug, and H. J. Güntherodt. Sublattice Identification in Scanning Force Microscopy on Alkali Halide Surfaces. *Phys. Rev. Lett.*, 92(14):146103+, 2004.
- [115] A. S. Foster, C. Barth, A. L. Shluger, and M. Reichling. Unambiguous Interpretation of Atomically Resolved Force Microscopy Images of an Insulator. *Phys. Rev. Lett.*, 86:2373–2376, 2001.
- [116] U. Dürig. Relations between interaction force and frequency shift in large-amplitude dynamic force microscopy. *Appl. Phys. Lett.*, 75(3):433–435, 1999.
- [117] B. Gotsmann, B. Anczykowski, C. Seidel, and H. Fuchs. Determination of tip-sample interaction forces from measured dynamic force spectroscopy curves. *Appl. Surf. Sci.*, 140:314–319, 1999.
- [118] H. Hölscher, W. Allers, U. D. Schwarz, A. Schwarz, and R. Wiesendanger. Determination of Tip-Sample Interaction Potentials by Dynamic Force Spectroscopy. *Phys. Rev. Lett.*, 83:4780–4783, 1999.
- [119] F. J. Giessibl. A direct method to calculate tip-sample forces from frequency shifts in frequency-modulation atomic force microscopy. *Appl. Phys. Lett.*, 78(1):123–125, 2001.
- [120] J. E. Sader and S. P. Jarvis. Accurate formulas for interaction force and energy in frequency modulation force spectroscopy. *Appl. Phys. Lett.*, 84(10):1801–1803, 2004.
- [121] S. Sadewasser and T. Glatzel, editors. *Kelvin Probe Force Microscopy - Measuring and Compensating Electrostatic Forces*. Springer Heidelberg, 2011.
- [122] T. König, T. Onig, G. H. Simon, H. P. Rust, G. Pacchioni, M. Heyde, and H. J. Freund. Measuring the Charge State of Point Defects on MgO/Ag(001). *JACS*, 131(48):17544–17545, 2009.
- [123] D. M. Eigler and E. K. Schweizer. Positioning single atoms with a scanning tunnelling microscope. *Nature*, 344(6266):524–526, 1990.

BIBLIOGRAPHY

- [124] I.-W. Lyo and P. Avouris. Field-induced nanometer- to atomic-scale manipulation of silicon surfaces with the stm. *Science*, 253(5016):173–176, 1991.
- [125] D. M. Eigler, C. P. Lutz, and W. E. Rudge. An atomic switch realized with the scanning tunnelling microscope. *Nature*, 352(6336):600–603, 1991.
- [126] M. F. Crommie, C. P. Lutz, and D. M. Eigler. Confinement of Electrons to Quantum Corrals on a Metal Surface. *Science*, 262(5131):218–220, 1993.
- [127] N. Nilius, T. M. Wallis, and W. Ho. Development of one-dimensional band structure in artificial gold chains. *Science*, 297(5588):1853–1856, 2002.
- [128] S.-W. Hla, L. Bartels, G. Meyer, and K.-H. Rieder. Inducing all steps of a chemical reaction with the scanning tunneling microscope tip: Towards single molecule engineering. *Phys. Rev. Lett.*, 85:2777–2780, 2000.
- [129] S.-W. Hla and K.-H. Rieder. Stm control of chemical reactions: Single-molecule synthesis. *Annual Review of Physical Chemistry*, 54(1):307–330, 2003.
- [130] L. Bartels, G. Meyer, and K.-H. Rieder. Controlled vertical manipulation of single co molecules with the scanning tunneling microscope: A route to chemical contrast. *Appl. Phys. Lett.*, 71(2):213–215, 1997.
- [131] T. A. Jung, R. R. Schlittler, J. K. Gimzewski, H. Tang, and C. Joachim. Controlled room-temperature positioning of individual molecules: Molecular flexure and motion. *Science*, 271(5246):181–184, 1996.
- [132] A. J. Heinrich, C. P. Lutz, J. A. Gupta, and D. M. Eigler. Molecule cascades. *Science*, 298(5597):1381–1387, 2002.
- [133] J. A. Stroscio, F. Tavazza, J. N. Crain, R. J. Celotta, and A. M. Chaka. Electronically induced atom motion in engineered cocun nanostructures. *Science*, 313(5789):948–951, 2006.
- [134] G. V. Nazin, X. H. Qiu, and W. Ho. Visualization and spectroscopy of a metal-molecule-metal bridge. *Science*, 302(5642):77–81, 2003.
- [135] L. Grill, K.-H. Rieder, F. Moresco, S. Stojkovic, A. Gourdon, and C. Joachim. Exploring the interatomic forces between tip and single molecules during stm manipulation. *Nano Lett.*, 6(12):2685–2689, 2006.

- [136] N. Oyabu, O. Custance, I. Yi, Y. Sugawara, and S. Morita. Mechanical vertical manipulation of selected single atoms by soft nanoindentation using near contact atomic force microscopy. *Phys. Rev. Lett.*, 90:176102, 2003.
- [137] N. Oyabu, Y. Sugimoto, M. Abe, O. Custance, and S. Morita. Lateral manipulation of single atoms at semiconductor surfaces using atomic force microscopy. *Nanotechnology*, 16(3):S112, 2005.
- [138] B. Such, T. Glatzel, S. Kawai, S. Koch, and E. Meyer. Three-dimensional force spectroscopy of kbr(001) by tuning fork-based cryogenic noncontact atomic force microscopy. *J. Vac. Sci. Technol. B*, 28(3):C4B1, 2010.
- [139] C. Loppacher, M. Guggisberg, O. Pfeiffer, E. Meyer, M. Bammerlin, R. Lüthi, R. Schlittler, J. K. Gimzewski, H. Tang, and C. Joachim. Direct determination of the energy required to operate a single molecule switch. *Phys. Rev. Lett.*, 90:066107, 2003.
- [140] J. Schütte, R. Bechstein, P. Rahe, H. Langhals, M. Rohlfing, and A. Kühnle. Single-molecule switching with non-contact atomic force microscopy. *Nanotechnology*, 22(24):245701, 2011.
- [141] Y. Sugimoto, M. Abe, S. Hirayama, N. Oyabu, O. Custance, and S. Morita. Atom inlays performed at room temperature using atomic force microscopy. *Nat Mater*, 4(2):156–159, 2005.
- [142] B. C. Stipe, M. A. Rezaei, W. Ho, S. Gao, M. Persson, and B. I. Lundqvist. Single-molecule dissociation by tunneling electrons. *Phys. Rev. Lett.*, 78:4410–4413, 1997.
- [143] J. Repp, G. Meyer, S. Paavilainen, F. E. Olsson, and M. Persson. Imaging Bond Formation Between a Gold Atom and Pentacene on an Insulating Surface. *Science*, 312(5777):1196–1199, 2006.
- [144] J. Repp and G. Meyer. Stm manipulation of single atoms and molecules on insulating films. In A. J. Mayne and G. Dujardin, editors, *Atom and Molecule Manipulation*, volume 2, chapter 2. Elsevier, 2011.
- [145] G. Meyer, L. Gross, F. Mohn, and J. Repp. Scanning Probe Microscopy of Atoms and Molecules on Insulating Films: From Imaging to Molecular Manipulation. *CHIMIA International Journal for Chemistry*, 66(1):10–15, 2012.
- [146] L. Bartels, G. Meyer, and K.-H. Rieder. Basic steps of lateral manipulation of single atoms and diatomic clusters with a scanning tunneling microscope tip. *Phys. Rev. Lett.*, 79:697–700, 1997.

- [147] Ingmar Swart, Tobias Sonnleitner, Judith Niedenführ, and Jascha Repp. Controlled lateral manipulation of molecules on insulating films by stm. *Nano Letters*, 12(2):1070–1074, 2012.
- [148] A. Schirmeisen, D. Weiner, and H. Fuchs. Single-Atom Contact Mechanics: From Atomic Scale Energy Barrier to Mechanical Relaxation Hysteresis. *Phys. Rev. Lett.*, 97(13):136101+, 2006.
- [149] M. Heyde, G. H. Simon, H. P. Rust, and H. J. Freund. Probing adsorption sites on thin oxide films by dynamic force microscopy. *Appl. Phys. Lett.*, 89(26):263107+, 2006.
- [150] M. Ashino, D. Obergfell, M. Haluska, S. Yang, A. N. Khlobystov, S. Roth, and R. Wiesendanger. Atomically resolved mechanical response of individual metallofullerene molecules confined inside carbon nanotubes. *Nat Nano*, 3(6):337–341, 2008.
- [151] T. Fukuma, Y. Ueda, S. Yoshioka, and H. Asakawa. Atomic-Scale Distribution of Water Molecules at the Mica-Water Interface Visualized by Three-Dimensional Scanning Force Microscopy. *Phys. Rev. Lett.*, 104(1):016101+, 2010.
- [152] K. Ruschmeier, A. Schirmeisen, and R. Hoffmann. Atomic-Scale Force-Vector Fields. *Phys. Rev. Lett.*, 101(15):156102+, 2008.
- [153] A. Schwarz, H. Hölscher, S. M. Langkat, and R. Wiesendanger. Three-dimensional force field spectroscopy. In *SCANNING TUNNELING MICROSCOPY/SPECTROSCOPY AND RELATED TECHNIQUES: 12th International Conference STM'03*, volume 696(1), pages 68–78. AIP, 2003.
- [154] S. Kawai, N. Sasaki, and H. Kawakatsu. Direct mapping of the lateral force gradient on si(111)7 × 7. *Phys. Rev. B*, 79:195412, 2009.
- [155] R. Hoffmann, D. Weiner, A. Schirmeisen, and A. S. Foster. Sublattice identification in noncontact atomic force microscopy of the NaCl(001) surface. *Phys. Rev. B*, 80(11):115426+, 2009.
- [156] L. Gross, F. Mohn, N. Moll, B. Schuler, A. Criado, E. Guitián, D. Peña, A. Gourdon, and G. Meyer. Bond-Order Discrimination by Atomic Force Microscopy. *Science*, 337(6100):1326–1329, 2012.
- [157] R. Pawlak, S. Frey, S. Kawai, T. Glatzel, H. Fang, L.-A. Fendt, F. Diederich, and E. Meyer. Directed Rotations of Single Porphyrin Molecules Controlled by Localized Force Spectroscopy. *ACS Nano*, 6(7):6318–6324, 2012.

- [158] S. Kawai and H. Kawakatsu. Surface-relaxation-induced giant corrugation on graphite (0001). *Phys. Rev. B*, 79:115440, 2009.
- [159] S. Fremy, S. Kawai, R. Pawlak, T. Glatzel, A. Baratoff, and E. Meyer. Three-dimensional dynamic force spectroscopy measurements on KBr(001): atomic deformations at small tip-sample separations. *Nanotechnology*, 23(5):055401+, 2012.
- [160] M. Z. Baykara, O. E. Dagdeviren, T. C. Schwendemann, H. Mönig, E. I. Altman, and U. D. Schwarz. Probing three-dimensional surface force fields with atomic resolution: Measurement strategies, limitations, and artifact reduction. *Beilstein Journal of Nanotechnology*, 3:637–650, 2012.
- [161] B. J. Albers, T. C. Schwendemann, M. Z. Baykara, N. Pilet, M. Liebmann, E. I. Altman, and U. D. Schwarz. Data acquisition and analysis procedures for high-resolution atomic force microscopy in three dimensions. *Nanotechnology*, 20(26):264002+, 2009.
- [162] M. Z. Baykara, T. C. Schwendemann, E. I. Altman, and U. D. Schwarz. Three-Dimensional Atomic Force Microscopy: Taking Surface Imaging to the Next Level. *Adv. Mat.*, 22(26-27):2838–2853, 2010.
- [163] S. Kawai, T. Glatzel, S. Koch, A. Baratoff, and E. Meyer. Interaction-induced atomic displacements revealed by drift-corrected dynamic force spectroscopy. *Phys. Rev. B*, 83:035421+, 2011.
- [164] D. W. Pohl and R. Möller. “Tracking” tunneling microscopy. *Rev. Sci. Ins.*, 59(6):840–842, 1988.
- [165] M. Abe, Y. Sugimoto, O. Custance, and S. Morita. Atom tracking for reproducible force spectroscopy at room temperature with non-contact atomic force microscopy. *Nanotechnology*, 16(12):3029–3034, 2005.
- [166] M. Abe, Y. Sugimoto, T. Namikawa, N. Morita, K. and Oyabu, and S. Morita. Drift-compensated data acquisition performed at room temperature with frequency modulation atomic force microscopy. *Appl. Phys. Lett.*, 90(20):203103+, 2007.
- [167] N. Oyabu, P. Pou, Y. Sugimoto, P. Jelinek, M. Abe, S. Morita, R. Pérez, and O. Custance. Single Atomic Contact Adhesion and Dissipation in Dynamic Force Microscopy. *Phys. Rev. Lett.*, 96(10):106101+, 2006.
- [168] R. Bennewitz, A. S. Foster, L. N. Kantorovich, M. Bammerlin, Ch Lopacher, S. Schär, M. Guggisberg, E. Meyer, and A. L. Shluger. Atomically resolved edges and kinks of NaCl islands on Cu(111): Experiment and theory. *Phys. Rev. B*, 62:2074–2084, 2000.

- [169] S. Maier, Yi Sang, T. Filleter, M. Grant, R. Bennewitz, E. Gnecco, and E. Meyer. Fluctuations and jump dynamics in atomic friction experiments. *Phys. Rev. B*, 72:245418, 2005.
- [170] I. Horcas, R. Fernández, J. M. Gómez-Rodríguez, J. Colchero, J. Gómez-Herrero, and A. M. Baro. WSXM: A software for scanning probe microscopy and a tool for nanotechnology. *Rev. Sci. Ins.*, 78(1):013705, 2007.
- [171] J. Berger, M. Švec, M. Müller, M. Ledinský, A. Fejfar, P. Jelínek, and Z. Majzik. Characterization of the mechanical properties of qplus sensors. *Beilstein Journal of Nanotechnology*, 4:1–9, 2013.
- [172] Z. Majzik, M. Setvín, A. Bettac, A. Feltz, V. Cháb, and P. Jelínek. Simultaneous current, force and dissipation measurements on the Si(111) 7×7 surface with an optimized qPlus AFM/STM technique. *Beilstein Journal of Nanotechnology*, 3:249–259, 2012.
- [173] A. J. Weymouth, T. Wutscher, J. Welker, T. Hofmann, and F. J. Giessibl. Phantom Force Induced by Tunneling Current: A Characterization on Si(111). *Phys. Rev. Lett.*, 106:226801, 2011.
- [174] T. Wutscher, A. J. Weymouth, and F. J. Giessibl. Localization of the phantom force induced by the tunneling current. *Phys. Rev. B*, 85:195426, 2012.
- [175] Neil W. Ashcroft and David N. Mermin. *Festkörperphysik*, volume 2. Oldenbourg, 3., verbesserte auflage. edition, 2005.
- [176] J. Hölzl and F. K. Schulte. *Springer Tracts in Modern Physics*. Springer Berlin Heidelberg New York, 1979.
- [177] G. Hörmandinger. Imaging of the Cu(111) surface state in scanning tunneling microscopy. *Phys. Rev. B*, 49:13897–13905, 1994.
- [178] W. Shockley. On the Surface States Associated with a Periodic Potential. *Phys. Rev.*, 56:317–323, 1939.
- [179] M Chelvayohan and C H B Mee. Work function measurements on (110), (100) and (111) surfaces of silver. *Journ. Phys.: Cond. Mat.*, 15(10):2305, 1982.
- [180] C. Jia, S.-X. Liu, C. Tanner, C. Leiggener, A. Neels, L. Sanguinet, E. Levillain, S. Leutwyler, A. Hauser, and S. Decurtins. An Experimental and Computational Study on Intramolecular Charge Transfer: A Tetrathiafulvalene-Fused Dipyridophenazine Molecule. *Chem. Eur. Jour.*, 13(13):3804–3812, 2007.

- [181] M. Jurow, A. E. Schuckman, J. D. Batteas, and C. M. Drain. Porphyrins as molecular electronic components of functional devices. *Coordination Chemistry Reviews*, 254:2297 – 2310, 2010.
- [182] L Zimmerli, S Maier, Th Glatzel, E Gnecco, O Pfeiffer, F Diederich, L Fendt, and E Meyer. Formation of molecular wires on nanostructured kbr. *Journ. Phys.: Cond. Mat.*, 61(1):1357, 2007.
- [183] S. Maier, L.-A. Fendt, L. Zimmerli, T. Glatzel, O. Pfeiffer, F. Diederich, and E. Meyer. Nanoscale Engineering of Molecular Porphyrin Wires on Insulating Surfaces. *Small*, 4(8):1115–1118, 2008.
- [184] T Glatzel, L. Zimmerli, S. Koch, S. Kawai, and E. Meyer. Molecular assemblies grown between metallic contacts on insulating surfaces. *Appl. Phys. Lett.*, 94(6):063303, 2009.
- [185] L. Gross, R. R. Schlittler, G. Meyer, L.-A. Fendt, F. Diederich, Th. Glatzel, S. Kawai, S. Koch, and E. Meyer. Contacting self-ordered molecular wires by nanostencil lithography. In *Journal of Vacuum Science & Technology B / Volume 28 / Issue 3*, volume 28(3), pages C4D34–C4D39. AVS, 2010.
- [186] P. Gregory. Industrial applications of phthalocyanines. *Journal of Porphyrins and Phthalocyanines*, 04(04):432–437, 2000.
- [187] C. J. Brabec, N. S. Sariciftci, and J. C. Hummelen. Plastic solar cells. *Adv. Funct. Mat.*, 11(1):15–26, 2001.
- [188] N. Koch. Organic electronic devices and their functional interfaces. *ChemPhysChem*, 8(10):1438–1455, 2007.
- [189] Y. Wang, K. Wu, J. Kröger, and R. Berndt. Review article: Structures of phthalocyanine molecules on surfaces studied by stm. *AIP Advances*, 2(4):041402, 2012.
- [190] J.K. Gimzewski, E. Stoll, and R.R. Schlittler. Scanning tunneling microscopy of individual molecules of copper phthalocyanine adsorbed on polycrystalline silver surfaces. *Surf. Sci.*, 181:267 – 277, 1987.
- [191] P. H. Lippel, R. J. Wilson, M. D. Miller, Ch. Wöll, and S. Chiang. High-resolution imaging of copper-phthalocyanine by scanning-tunneling microscopy. *Phys. Rev. Lett.*, 62:171–174, 1989.
- [192] J.-Y. Grand, T. Kunstmann, D. Hoffmann, A. Haas, M. Dietsche, J. Seifritz, and R. Möller. Epitaxial growth of copper phthalocyanine monolayers on ag(111). *Surf. Sci.*, 366(3):403 – 414, 1996.

- [193] C. Bobisch, Th. Wagner, A. Bannani, and R. Möller. Ordered binary monolayer composed of two organic molecules: Copper-phthalocyanine and 3,4,9,10-perylene-tetra-carboxylic- dianhydride on cu(111). *The Journal of Chemical Physics*, 119(18):9804–9808, 2003.
- [194] T. Fukuma, K. Kobayashi, H. Yamada, and Matsushige K. Non-contact atomic force microscopy study of copper-phthalocyanines: Submolecular-scale contrasts in topography and energy dissipation. *Journ. Appl. Phys.*, 95(9):4742–4746, 2004.
- [195] A. Tekiel, M. Goryl, and M. Szymonski. Copper phthalocyanine molecules on an insb(001) c(8×2) surface studied by ultra-high-vacuum stm and non-contact afm. *Nanotechnology*, 18(47):475707, 2007.
- [196] K. Manandhar, T. Ellis, K.T. Park, T. Cai, Z. Song, and J. Hrbek. A scanning tunneling microscopy study on the effect of post-deposition annealing of copper phthalocyanine thin films. *Surf. Sci.*, 601(17):3623 – 3631, 2007.
- [197] D. G. de Oteyza, A. El-Sayed, J. M. Garcia-Lastra, E. Goiri, T. N. Krauss, A. Turak, E. Barrera, H. Dosch, J. Zegenhagen, A. Rubio, Y. Wakayama, and J. E. Ortega. Copper-phthalocyanine based metal–organic interfaces: The effect of fluorination, the substrate, and its symmetry. *The Journal of Chemical Physics*, 133(21):214703, 2010.
- [198] J. Ren, S. Meng, Y.-L Wang, X. C. Ma, Q. K. Xue, and E. Kaxiras. Properties of copper (fluoro-)phthalocyanine layers deposited on epitaxial graphene. *The Journal of Chemical Physics*, 134(19):194706, 2011.
- [199] I. Swart, T. Sonleitner, and J. Repp. Charge State Control of Molecules Reveals Modification of the Tunneling Barrier with Intramolecular Contrast. *Nano Lett.*, 11(4):1580–1584, 2011.
- [200] C. Uhlmann, I. Swart, and J. Repp. Controlling the orbital sequence in individual cu-phthalocyanine molecules. *Nano Lett.*, 13(2):777–780, 2013.
- [201] J. Schaffert, M. C. Cottin, A. Sonntag, H. Karacuban, C. A. Bobisch, N. Lorente, J.-P. Gauyacq, and R. Möller. Imaging the dynamics of individually adsorbed molecules. *Nat Mater*, 12(3):223–227, 2013.
- [202] Bao Z., A. J. Lovinger, and A. Dodabalapur. Organic field-effect transistors with high mobility based on copper phthalocyanine. *Appl. Phys. Lett.*, 69(20):3066–3068, 1996.
- [203] R. R. Lunt, J. B. Benziger, and S. R. Forrest. Growth of an ordered crystalline organic heterojunction. *Adv. Mat.*, 19(23):4229–4233, 2007.

- [204] J. Blochwitz, M. Pfeiffer, T. Fritz, and K. Leo. Low voltage organic light emitting diodes featuring doped phthalocyanine as hole transport material. *Appl. Phys. Lett.*, 73(6):729–731, 1998.
- [205] L. Zou, V. Savvate'ev, J. Booher, C.-H. Kim, and J. Shinar. Combinatorial fabrication and studies of intense efficient ultraviolet–violet organic light-emitting device arrays. *Appl. Phys. Lett.*, 79(14):2282–2284, 2001.
- [206] P. Peumans, A. Yakimov, and S. R. Forrest. Small molecular weight organic thin-film photodetectors and solar cells. *Journ. Appl. Phys.*, 93(7):3693–3723, 2003.
- [207] C. Zhang, S. W. Tong, C. Jiang, E. T. Kang, D. S. H. Chan, and Zhu C. Efficient multilayer organic solar cells using the optical interference peak. *Appl. Phys. Lett.*, 93(4):043307, 2008.
- [208] H. W. Kroto, J. R. Heath, S. C. O'Brien, R. F. Curl, and R. E. Smalley. C60: Buckminsterfullerene. *Nature*, 318:162–163, 1985.
- [209] M. Marschall, J. Reichert, A. Weber-Bargioni, K. Seufert, W. Auwärter, S. Klyatskaya, G. Zoppellaro, M. Ruben, and J. V. Barth. Random two-dimensional string networks based on divergent coordination assembly. *Nat Chem*, 2(2):131–137, 2010.
- [210] B. Such, T. Trevethan, T. Glatzel, S. Kawai, L. Zimmerli, E. Meyer, A. L. Shluger, C. H. M. Amijs, P. de Mendoza, and A. M. Echavarren. Functionalized Truxenes: Adsorption and Diffusion of Single Molecules on the KBr(001) Surface. *ACS Nano*, 4(6):3429–3439, 2010.
- [211] T. Trevethan, B. Such, T. Glatzel, S. Kawai, A. L. Shluger, E. Meyer, P. de Mendoza, and A. M. Echavarren. Organic Molecules Reconstruct Nanostructures on Ionic Surfaces. *Small*, 7(9):1264–1270, 2011.
- [212] A. Hinaut, A. Pujol, F. Chaumeton, D. Martrou, A. Gourdon, and S. Gauthier. An *nc – afm* and *kpfm* study of the adsorption of a triphenylene derivative on kbr(001). *Beilstein Journal of Nanotechnology*, 3:221–229, 2012.
- [213] T.-C. Tseng, C. Urban, Y. Wang, R. Otero, S. L. Tait, M. Alcamí, D. Écija, M. Trelka, J. Gallego, N. Lin, M. Konuma, U. Starke, A. Nefedov, Al. Langner, C. Wöll, M. Herranz, F. Martín, N. Martín, K. Kern, and R. Miranda. Charge-transfer-induced structural rearrangements at both sides of organic/metal interfaces. *Nat Chem*, 2(5):374–379, 2010.
- [214] T. Yokoyama, S. Yokoyama, T. Kamikado, Y. Okuno, and S. Mashiko. Selective assembly on a surface of supramolecular aggregates with controlled size and shape. *Nature*, 413(6856):619–621, 2001.

- [215] T. Zambelli, Y. Boutayeb, F. Gayral, J. Lagoute, N. K. Girdhar, A. Gourdon, S. Gauthier, Blanco, Chambron, V. Heitz, and Sauvage. Deposition of large organic molecules in ultra-high vacuum: a comparison between thermal sublimation and pulse injection. *International Journal of Nanoscience*, 03(03):331–341, 2004.
- [216] C. Hamann, R. Woltmann, I-P. Hong, N. Hauptmann, S. Karan, and R. Berndt. Ultrahigh vacuum deposition of organic molecules by electrospray ionization. *Rev. Sci. Ins.*, 82(3):033903, 2011.
- [217] S. Rauschenbach, F. L. Stadler, E. Lunedei, N. Malinowski, S. Koltsov, G. Costantini, and K. Kern. Electrospray Ion Beam Deposition of Clusters and Biomolecules. *Small*, 2(4):540–547, 2006.
- [218] C. J. Satterley, L. M. A. Perdigão, A. Saywell, G. Magnano, A. Rienzo, Louise C. M., V-. R. Dhanak, P. H. Beton, and J. N. O’Shea. Electrospray deposition of fullerenes in ultra-high vacuum: in-situ scanning tunneling microscopy and photoemission spectroscopy. *Nanotechnology*, 18(45):455304+, 2007.
- [219] J. B. Fenn, M. Mann, C. K. Meng, S. F. Wong, and C. M. Whitehouse. Electrospray ionization for mass spectrometry of large biomolecules. *Science (New York, N.Y.)*, 246(4926):64–71, 1989.
- [220] C. J. McNeal, R. D. Macfarlane, and E. L. Thurston. Thin film deposition by the electrospray method for californium-252 plasma desorption studies of involatile molecules. *Anal. Chem.*, 51(12):2036–2039, 1979.
- [221] N. Hauptmann, C. Hamann, H. Tang, and R. Berndt. Soft-Landing Electrospray Deposition of the Ruthenium Dye N3 on Au(111). *J. Phys. Chem. C*, 117(19):9734–9738, 2013.
- [222] N. Wintjes, J. Hornung, J. Lobo-Checa, T. Voigt, T. Samuely, C. Thilgen, M. Stöhr, F. Diederich, and T. A. Jung. Supramolecular Synthons on Surfaces: Controlling Dimensionality and Periodicity of Tetraarylporphyrin Assemblies by the Interplay of Cyano and Alkoxy Substituents. *Chem. Eur. Jour.*, 14(19):5794–5802, 2008.
- [223] S. et al. Fremy. On the chemical stability of a donor-acceptor molecule: influence of substrates and deposition conditions. in preparation, 2013.
- [224] J. Lobo-Checa, M. Matena, K. Muller, J. H. Dil, F. Meier, L. H. Gade, T. A. Jung, and M. Stöhr. Band Formation from Coupled Quantum Dots Formed by a Nanoporous Network on a Copper Surface. *Science*, 325(5938):300–303, 2009.

- [225] J. Rusanova, S. Decurtins, E. Rusanov, H. Stoeckli-Evans, S. Delahaye, and A. Hauser. Ruthenium(ii) complex of bis(2,2-bipyridine)(6,7-dicyanodipyrido[3,2-a:2,3-c]phenazine): synthesis, structure, electrochemical and luminescence studies. *Journ. Chem. Soc.: Dalton Trans.*, 0(23):4318–4320, 2002.
- [226] S. Ott and R. Faust. Substituted 1,10-phenanthroline-5,6-diamines and their extension to soluble, acetylenic pyrazinophenanthroline. *Synthesis*, 18:3135–3139, 2005.
- [227] H Karacuban, S Koch, M Fendrich, Th Wagner, and R Möller. Ptcd on cu(111) partially covered with nacl. *Nanotechnology*, 22(29):295305, 2011.
- [228] L. Howald, E. Meyer, R. Lüthi, H. Haefke, R. Overney, H. Rudin, and H. J. Güntherodt. Multifunctional probe microscope for facile operation in ultrahigh vacuum. *Appl. Phys. Lett.*, 63(1):117–119, 1993.
- [229] I. Fleming. *Molecular Orbitals and Organic Chemical Reactions*. John Wiley and Sons, 2010.
- [230] H. Haken and H. C. Wolf. *Molekülphysik und Quantenchemie*, volume 4. Springer Berlin Heidelberg New York, 2003.
- [231] H. Hoppe and N. S. Sariciftci. Organic solar cells: An overview. *Journal of Materials Research*, 19:1924–1945, 2004.
- [232] H. Ibach. *Physics of Surfaces and Interfaces*. Springer, 2006.
- [233] H. Lüth. *Solid Surfaces, Interfaces and Thin Films*. Springer, 5 edition, 2010.
- [234] M. Henzler and W. Göpel. *Oberflächenphysik des Festkörpers*. Teubner Stuttgart, 1991.
- [235] K. Wandelt. Surface characterization by photoemission of adsorbed xenon (pax). *Journ. Vac. Sci. & Techn. A*, 2(2):802–807, 1984.
- [236] K. Wandelt. The local work function: Concept and implications. *Appl. Surf. Sci.*, 111(0):1 – 10, 1997.
- [237] Th. Glatzel, S. Sadewasser, R. Shikler, Y. Rosenwaks, and M.Ch. Lux-Steiner. Kelvin probe force microscopy on iii-v semiconductors: the effect of surface defects on the local work function. *Mat. Sci. Engineer. B*, 102:138, 2003.
- [238] Th. Glatzel, L. Zimmerli, and E. Meyer. Molecular assemblies on insulating ultrathin films analyzed by nc-afm and kpfm. *Israel Journal of Chemistry*, 48(2):107–116, 2008.

BIBLIOGRAPHY

- [239] K. Bradley, J.-C. P. Gabriel, M. Briman, A. Star, and G. Grüner. Charge transfer from ammonia physisorbed on nanotubes. *Phys. Rev. Lett.*, 91:218301, 2003.
- [240] J. K. Gimzewski and C. Joachim. Nanoscale science of single molecules using local probes. *Science*, 283(5408):1683–1688, 1999.
- [241] T. A. Jung, R. R. Schlittler, and J. K. Gimzewski. Conformational identification of individual adsorbed molecules with the stm. *Nature*, 386(6626):696–698, 1997.
- [242] B. Stadtmüller, I. Kröger, F. Reinert, and C. Kumpf. Submonolayer growth of *cupc* on noble metal surfaces. *Phys. Rev. B*, 83:085416, 2011.
- [243] H. Cun, Y. Wang, S. Du, L. Zhang, L. Zhang, B. Yang, X. He, Y. Wang, X. Zhu, Q. Yuan, Y.-P. Zhao, M. Ouyang, W. A. Hofer, S. J. Pennycook, and H.-j. Gao. Tuning structural and mechanical properties of two-dimensional molecular crystals: The roles of carbon side chains. *Nano Lett.*, 12(3):1229–1234, 2012.
- [244] J. A. Rogers. Toward paperlike displays. *Science*, 291(5508):1502–1503, 2001.
- [245] S. Park, G. Wang, B. Cho, Y. Kim, S. Song, Y. Ji, M.-H. Yoon, and T. Lee. Flexible molecular-scale electronic devices. *Nat Nano*, 7(7):438–442, 2012.
- [246] H. Ishii, K. Sugiyama, E. Ito, and K. Seki. Energy level alignment and interfacial electronic structures at organic/metal and organic/organic interfaces. *Adv. Mat.*, 11(8):605–625, 1999.
- [247] A. Kahn, N. Koch, and W. Gao. Electronic structure and electrical properties of interfaces between metals and π -conjugated molecular films. *Journal of Polymer Science Part B: Polymer Physics*, 41(21):2529–2548, 2003.
- [248] B. de Boer, A. Hadipour, M. M. Mandoc, T. van Woudenberg, and P. W. M. Blom. Tuning of metal work functions with self-assembled monolayers. *Adv. Mat.*, 17(5):621–625, 2005.
- [249] L. Giordano, F. Cinquini, and G. Pacchioni. Tuning the surface metal work function by deposition of ultrathin oxide films: Density functional calculations. *Phys. Rev. B*, 73:045414, 2006.
- [250] P. C. Rusu, G. Giovannetti, and G. Brocks. Dipole formation at interfaces of alkanethiolate self-assembled monolayers and $ag(111)$. *The Journal of Physical Chemistry C*, 111(39):14448–14456, 2007.

- [251] X. Crispin, V. Geskin, A. Crispin, J. Cornil, R. Lazzaroni, W. R. Salaneck, and J.-L. Brédas. Characterization of the interface dipole at organic/ metal interfaces. *JACS*, 124(27):8131–8141, 2002.
- [252] H. Vázquez, Y. J. Dappe, J. Ortega, and F. Flores. Energy level alignment at metal/organic semiconductor interfaces: “pillow” effect, induced density of interface states, and charge neutrality level. *The Journal of Chemical Physics*, 126(14):144703, 2007.
- [253] R. S. Mulliken. A new electroaffinity scale; together with data on valence states and on valence ionization potentials and electron affinities. *The Journal of Chemical Physics*, 2(11):782–793, 1934.
- [254] A. Alkauskas, L. Ramoino, S. Schintke, M. von Arx, A. Baratoff, H.-J. Güntherodt, and T. A. Jung. Energy level alignment at metal-octaethylporphyrin interfaces. *The Journal of Physical Chemistry B*, 109(49):23558–23563, 2005.
- [255] P. S. Bagus, V. Staemmler, and C. Wöll. Exchangelike effects for closed-shell adsorbates: Interface dipole and work function. *Phys. Rev. Lett.*, 89:096104, 2002.
- [256] M. Knupfer and T. Schwieger. Chemisorption at interfaces between organic semiconductors and metals: role of the electron affinity. *Appl. Surf. Sci.*, 252(1):77 – 80, 2005.
- [257] O. T. Hofmann, D. A. Egger, and E. Zojer. Work-function modification beyond pinning: When do molecular dipoles count? *Nano Lett.*, 10(11):4369–4374, 2010.
- [258] R. Bennewitz, V. Barwich, M. Bammerlin, C. Loppacher, M. Guggisberg, A. Baratoff, E. Meyer, and H. J. Güntherodt. Ultrathin films of nacl on cu(111): a lead and dynamic force microscopy study. *Surf. Sci.*, 438:289–296, 1999.
- [259] J. Repp, P. Liljeroth, and G. Meyer. Coherent electron-nuclear coupling in oligothiophene molecular wires. *Nature Physics*, 6(12):975–979, 2010.
- [260] I. Giaever and H. R. Zeller. Superconductivity of Small Tin Particles Measured by Tunneling. *Phys. Rev. Lett.*, 20:1504–1507, 1968.
- [261] H. R. Zeller and I. Giaever. Tunneling, Zero-Bias Anomalies, and Small Superconductors. *Phys. Rev.*, 181:789–799, 1969.
- [262] N. Wintjes, D. Bonifazi, F. Cheng, A. Kiebele, M. Stöhr, T. Jung, H. Spillmann, and F. Diederich. A supramolecular multiposition rotary device. *Angewandte Chemie International Edition*, 46(22):4089–4092, 2007.

- [263] Y. Shirai, A. J. Osgood, Y. Zhao, Y. Yao, L. Saudan, H. Yang, C. Yu-Hung, L. B. Alemany, T. Sasaki, J.-F. Morin, J. M. Guerrero, K. F. Kelly, and J. M. Tour. Surface-rolling molecules. *JACS*, 128(14):4854–4864, 2006.
- [264] W. R. Browne and B. L. Feringa. Making molecular machines work. *Nat Nano*, 1(1):25–35, 2006.
- [265] T. Kudernac, N. Ruangsupapichat, M. Parschau, B. Macia, N. Katsonis, S. R. Harutyunyan, K.-H. Ernst, and B. L. Feringa. Electrically driven directional motion of a four-wheeled molecule on a metal surface. *Nature*, 479(7372):208–211, 2011.
- [266] Y. Shirai, A. J. Osgood, Y. Zhao, K. F. Kelly, and J. M. Tour. Directional control in thermally driven single-molecule nanocars. *Nano Lett.*, 5(11):2330–2334, 2005.
- [267] L. Savio, F. Moresco, L. Gross, A. Gourdon, C. Joachim, and K.-H. Rieder. Conformations and controlled manipulation of a long molecular wire on cu(111). *Surf. Sci.*, 585:38 – 46, 2005.
- [268] V. Iancu, A. Deshpande, and S.-W. Hla. Manipulating kondo temperature via single molecule switching. *Nano Lett.*, 6(4):820–823, 2006.
- [269] F. Moresco, G. Meyer, K. H. Rieder, J. Ping, H. Tang, and C. Joachim. Tbpp molecules on copper surfaces: a low temperature scanning tunneling microscope investigation. *Surf. Sci.*, 499(1):94 – 102, 2002.
- [270] N. Fournier, C. Wagner, C. Weiss, R. Temirov, and F. S. Tautz. Force-controlled lifting of molecular wires. *Phys. Rev. B*, 84:035435, 2011.
- [271] R. Pawlak, S. Kawai, T. Glatzel, S. Fremy, H. Fang, L.-A. Fendt, F. Diederich, E. Gnecco, Baratoff A., and E. Meyer. Atomic-scale friction sensed by single organic molecule. in preparation, 2013.
- [272] S. Kawai, F. F. Canova, T. Glatzel, A. S. Foster, and E. Meyer. Atomic-scale dissipation processes in dynamic force spectroscopy. *Phys. Rev. B*, 84:115415, 2011.
- [273] D. A. Davis, A. Hamilton, J. Yang, L. D. Cremer, D. Van Gough, S. L. Potisek, M. T. Ong, P. V. Braun, T. J. Martinez, S. R. White, J. S. Moore, and N. R. Sottos. Force-induced activation of covalent bonds in mechanoresponsive polymeric materials. *Nature*, 459(7243):68–72, 2009.
- [274] M. Haruta. Size- and support-dependency in the catalysis of gold. *Catalysis Today*, 36(1):153 – 166, 1997.

- [275] S. W. Wu, N. Ogawa, and W. Ho. Atomic-scale coupling of photons to single-molecule junctions. *Science*, 312(5778):1362–1365, 2006.
- [276] A. H. Flood, J. F. Stoddart, D. W. Steuerman, and J. R. Heath. Whence molecular electronics? *Science*, 306(5704):2055–2056, 2004.
- [277] F. Mohn, L. Gross, and G. Meyer. Measuring the short-range force field above a single molecule with atomic resolution. *Appl. Phys. Lett.*, 99(5):053106, 2011.
- [278] J. Repp, G. Meyer, F. E. Olsson, and M. Persson. Controlling the Charge State of Individual Gold Adatoms. *Science*, 305(5683):493–495, 2004.
- [279] A. Mugarza, R. Robles, C. Krull, R. Korytár, N. Lorente, and P. Gambardella. Electronic and magnetic properties of molecule-metal interfaces: Transition-metal phthalocyanines adsorbed on *ag*(100). *Phys. Rev. B*, 85:155437, 2012.
- [280] J. Schaffert, M. C. Cottin, A. Sonntag, C. A. Bobisch, R. Möller, J.-P. Gauyacq, and N. Lorente. Tunneling electron induced rotation of a copper phthalocyanine molecule on *cu*(111). *Phys. Rev. B*, 88:075410, 2013.
- [281] N. Marom, O. Hod, G. E. Scuseria, and L. Kronik. Electronic structure of copper phthalocyanine: A comparative density functional theory study. *The Journal of Chemical Physics*, 128(16):–, 2008.
- [282] X. H. Qiu, G. V. Nazin, and W. Ho. Vibronic states in single molecule electron transport. *Phys. Rev. Lett.*, 92:206102, 2004.
- [283] H. Karacuban, M. Lange, J. Schaffert, O. Weingart, Th. Wagner, and R. Möller. Substrate-induced symmetry reduction of *cupc* on *cu*(111): An *lt*-stm study. *Surf. Sci.*, 603(5):L39 – L43, 2009.
- [284] S.-H. Chang, S. Kuck, J. Brede, L. Lichtenstein, G. Hoffmann, and R. Wiesendanger. Symmetry reduction of metal phthalocyanines on metals. *Phys. Rev. B*, 78:233409, 2008.
- [285] Christoph Uhlmann. *Tieftemperatur-Rastertunnelmikroskopie an Phtalocyanine-Molekülen auf ultradünnen Isolatorfilmen: Ladungszustand, Jahn-Teller Effekt und ein momolekular Schalter*. PhD thesis, Universität Regensburg, 2013.
- [286] R. Berndt, R. Gaisch, J. K. Gimzewski, B. Reihl, R. R. Schlittler, W. D. Schneider, and M. Tschudy. Photon emission at molecular resolution induced by a scanning tunneling microscope. *Science*, 262(5138):1425–1427, 1993.

- [287] C. Chen, C. A. Bobisch, and W. Ho. Visualization of fermi's golden rule through imaging of light emission from atomic silver chains. *Science*, 325(5943):981–985, 2009.
- [288] Th.W. Matthes, Ch. Sommerhalter, A. Rettenberger, M. Böhmisch, J. Boneberg, M.Ch. Lux-Steiner, and P. Leiderer. Investigation of photoinduced tunneling current and local surface photovoltage by stm. *Appl. Surf. Sci.*, 123-124(0):187 – 191, 1998.
- [289] H. Mönig, Y. Smith, R. Caballero, C. A. Kaufmann, I. Lauermann, M. Ch. Lux-Steiner, and S. Sadewasser. Direct evidence for a reduced density of deep level defects at grain boundaries of Cu(In, Ga)_{se2} thin films. *Phys. Rev. Lett.*, 105:116802, 2010.
- [290] Changqing Ye, Mingzhu Li, Jia Luo, Linfeng Chen, Zhengming Tang, Jian Pei, Lei Jiang, Yanlin Song, and Daoben Zhu. Photo-induced amplification of readout contrast in nanoscale data storage. *J. Mater. Chem.*, 22:4299–4305, 2012.
- [291] J. R. Hahn and W. Ho. Vibrational mode specific bond dissociation in a single molecule. *The Journal of Chemical Physics*, 131(4):044706, 2009.
- [292] S. Tan, H. Feng, Y. Ji, Y. Wang, J. Zhao, A. Zhao, B. Wang, Y. Luo, J. Yang, and J. G. Hou. Observation of photocatalytic dissociation of water on terminal ti sites of tio₂(110)-1x1 surface. *JACS*, 134(24):9978–9985, 2012.
- [293] M. J. Comstock, N. Levy, A. Kirakosian, J. Cho, F. Lauterwasser, J. H. Harvey, D. A. Strubbe, J. M. J. Fréchet, D. Trauner, S. G. Louie, and M. F. Crommie. Reversible photomechanical switching of individual engineered molecules at a metallic surface. *Phys. Rev. Lett.*, 99:038301, 2007.
- [294] J. Cho, L. Berbil-Bautista, I. V. Pechenezhskiy, N. Levy, S. K. Meier, V. Srinivasan, Y. Kanai, J. C. Grossman, K. P. C. Vollhardt, and M. F. Crommie. Single-molecule-resolved structural changes induced by temperature and light in surface-bound organometallic molecules designed for energy storage. *ACS Nano*, 5(5):3701–3706, 2011.
- [295] Y. Aburaya, H. Nomura, Kageshima M., Y. Naitoh, Y. J. Li, and Y. Sugawara. Switching surface polarization of atomic force microscopy probe utilizing photoisomerization of photochromic molecules. *Journ. Appl. Phys.*, 109(6):064308, 2011.
- [296] C. Loppacher, U. Zerweck, S. Teich, E. Beyreuther, T. Otto, S. Grafström, and L. M. Eng. Fm demodulated kelvin probe force microscopy for surface photovoltage tracking. *Nanotechnology*, 16(3):S1, 2005.

- [297] F. Streicher, S. Sadewasser, and M. Ch. Lux-Steiner. Surface photovoltage spectroscopy in a kelvin probe force microscope under ultrahigh vacuum. *Rev. Sci. Ins.*, 80(1):013907, 2009.
- [298] M. Ikeda, N. Koide, L. Han, A. Sasahara, and H. Onishi. Work function on dye-adsorbed *tio2* surfaces measured by using a kelvin probe force microscope. *The Journal of Physical Chemistry C*, 112(17):6961–6967, 2008.
- [299] Alex Henning, Gino Günzburger, Res Jöhr, Y. Rosenwaks, B. Bozic-Weber, C. E. Housecroft, E. C. Constable, E. Meyer, and T. Glatzel. Kelvin probe force microscopy of nanocrystalline *tio2* photoelectrodes. *Beilstein Journal of Nanotechnology*, 4:418–428, 2013.
- [300] S. A. Burke, J. M. LeDue, J. M. Topple, S. Fostner, and P. Grütter. Relating the functional properties of an organic semiconductor to molecular structure by nc-afm. *Adv. Mat.*, 21(20):2029–2033, 2009.
- [301] R. Pawlak, T. Glatzel, V. Pichot, L. Schmidlin, S. Kawai, S. Fremy, and E. Spitzer, D. Meyer. Local detection of nitrogen-vacancy centers in a nanodiamond monolayer. submitted, 2013.
- [302] F. Yang and S. R. Forrest. Organic solar cells using transparent *sno-f* anodes. *Adv. Mat.*, 18(15):2018–2022, 2006.
- [303] L. Kronik and Y. Shapira. Surface photovoltage phenomena: theory, experiment, and applications. *Surf. Sci. Rep.*, 37:1 – 206, 1999.
- [304] H. J. Lewerenz and H. Jungblut. *Photovoltaic - Grundlagen und Anwendungen*. Springer Berlin, 1995.
- [305] R. R. Lunt, N. C. Giebink, A. A. Belak, J. B. Benziger, and S. R. Forrest. Exciton diffusion lengths of organic semiconductor thin films measured by spectrally resolved photoluminescence quenching. *Journ. Appl. Phys.*, 105(5):053711, 2009.
- [306] J. A. Larsson, S. D. Elliott, J. C. Greer, J. Repp, G. Meyer, and R. Allenspach. Orientation of individual c_{60} molecules adsorbed on cu(111): Low-temperature scanning tunneling microscopy and density functional calculations. *Phys. Rev. B*, 77:115434, 2008.

Appendix A

Outlook: Towards Optically Induced Charge Transfers

Several SPM based attempts have been demonstrated in order to investigate the coupling of photons to matter. Two main approaches are possible: detecting tip induced photon emission or studying the excited states of matter after absorption of photons. With respect to opto-electronic applications and their performance, the majority of questions is related to the mechanisms behind charge carrier generation and -transport. In organic molecules the absorption of photons leads to the generation of excitons by the transfer of electrons into energetically higher levels. Charge transfers (CT), leading to separated charges can then occur either on an intramolecular level within fused donor-acceptor (D-A) molecules, or intermolecular between a donating (D) and accepting (A) species. However, up to now no complete theory is available.

The ability to directly observe CTs on the single (or two molecular) level could highly improve the general understanding. Due to the weak nature of bonding the optical response of a molecular crystal is usually dominated by the optical response within each single molecule. Observing these phenomena might become possible by SPM techniques [184] mediated by their appealing local character, which exceeds that by other conventional optical methods by far. Yet, modifications by the interface electronic structure between the molecules and the underlying substrates need to be taken into account [see Sec. 4.5], which might cause significant differences compared to the absorption behavior of molecules in gas phase, solution, or within multilayer assemblies.

By means of STM, for instance, photon emission from the tunneling junction, induced by inelastic tunneling electrons [286], could be detected by introducing an optic spectrometry setup into the microscope. With a similar method, also Fermi's golden rule was visualized [287]. On the other hand, by introducing light into the STM, photo induced currents and surface photo

voltages (SPV) were investigated [288–290], and the coupling of photons to single molecules could be addressed by exciting electrons in the STM tip, which then tunneled into unoccupied energy levels of the molecules [275]. Other experiments in turn focused on photo catalytic reactions by photo induced excitations of vibrational modes [291,292], or on the conversion of light into mechanical motion by photo isomerization [293–295].

In the AFM community, mainly the second approach was traced: light induced SPVs were detected by means of KPFM [296, 297]. In this manner, it became possible to study light induced electron transport at molecule-substrate interfaces via changes of the local surface dipole moments [97,298,299], or differences in the optical response for slightly different arrangements of molecular islands [300]. Furthermore, by utilizing tuning fork sensors, a combined study of light assisted local bias spectroscopy and STS allowed to investigate sub-surface nitrogen-vacancy centers of nano diamonds [301].

The present investigations aim at observing intermolecular charge transfers between CuPc and C₆₀ molecules, a commonly adopted combination for heterojunction organic solar cells. To do so, a measurement procedure based on one-dimensional bias spectroscopy has been employed. However, before this procedure will be described, first, a few considerations about optical excitations will be presented in the next section. Finally, the basic working principle of heterojunction solar cells will be summarized, followed by a state-of-the-art on the detection of the optically induced charge transfer in this system together with propositions for improvements.

Optical Excitations

The interaction with electromagnetic fields is mediated by photons. To be absorbed, their energies need to match the energetic difference between certain excited- (n) states and the ground state (m). While for organic materials this leads to the generation of excitons, for metals or semi-conductors in principle plasmons need to be regarded, which are however not relevant for the present considerations, because all excitations have been carried out within the visible regime of light (400 nm to 800 nm).

Absorption Spectrum

Which transitions can be excited within a molecule, is determined by Fermi's golden rule. On basis of the time-dependent perturbation approach the probability for an optical transition is proportional to the matrix element of the transition dipole moment from state Ψ_n to Ψ_m :

$$W_{nm} \propto |\langle \Psi_n | \vec{e}_E \vec{p} | \Psi_m \rangle|, \quad (\text{A.1})$$

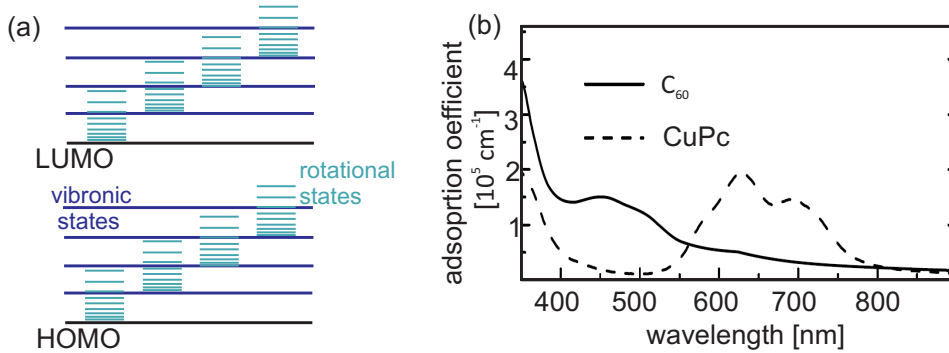


Figure A.1: Optical spectras (a) Scheme of an optical spectrum of a molecule, featuring electronic, vibronic, and rotational transitions. (b) Absorption coefficient as a function of the wave length for CuPc and C_{60} , figure from [302].

where e_E is the unit vector in field direction. The elements of the transition matrix strongly depend on the symmetry of the molecular states Ψ_n and Ψ_m , which results in a much more complicated situation compared to optical excitations of atoms. Those elements equal zero correspond to forbidden transitions, and the lowest energy transition to a HOMO-LUMO excitation of the molecule, which is the most important one for the present investigations. Conjugated molecules feature rather small band gaps of ≈ 2 eV [231], which makes them sensitive to light in the visible regime.

The total excitation energy $E = h\nu = E_n - E_m$ of an electron transition within a molecule is generally comprised by three different terms

$$E = E_{rot} + E_{vib} + E_{el}, \quad (\text{A.2})$$

corresponding to electron (el), vibrational (vib) and rotational (rot) excitation [230]. A typical spectrum is depicted in Fig. A.1 (a). Electrons that are excited from the ground state E_m to E_n can also enter any vibrational or rotational level associated with the specific electron excitation level. Electron transitions can be already excited with light in the visible or UV regime, while pure vibrational or rotational excitations require infrared or microwave light. Suitable wavelengths for excitation experiments are deduced from absorption spectras. For the two molecules CuPc and C_{60} spectra showing the absorption coefficient as a function of the wavelength on indium tin oxide (ITO) substrates are presented in Fig. A.1 (b), adopted from [302].

Surface Photo Voltage

The photovoltaic effect gives rise to a light induced change of the equilibrium potential distribution within a solid or molecule by charge transfer. If the illumination induced charge carrier generation is followed by a net charge redistribution close to the surface, the consequence is a surface photo voltage

(U_{SPV}), which is defined by

$$U_{SPV} = U_S^{\text{illu}} - U_S^{\text{dark}}. \quad (\text{A.3})$$

This effect is widely used in SPV spectroscopy to characterize semiconductors. A detailed overview is given for instance in [303]. The charge redistribution also gives rise to a change in the CPD and LCPD, and thus, in the local work function, which was intensely studied by the combination of KPFM and SPV spectroscopy for various systems, as mentioned in the introduction to this chapter. Due to the ultra-high resolution obtainable with local bias spectroscopy [see Chap. 6] it might be even possible to detect light induced charge redistribution within single molecules, or between a donor- and acceptor- molecule.

Experimental

Light Source

The samples were illuminated from the outside of the microscope through a UHV flange (quartz glass)[†] with an incident angle of $\approx 40^\circ$ with respect to the horizontal axis. It was tested, that the transmitted intensity for the investigated wavelength was about 99%. A combined BioLED light source from Mightex (BLS-XX04-U/S) was used and always operated in the continuous wave mode, with the maximum output intensity of 10 mW. Four different wave lengths are available, 590 nm, 530 nm, 470 nm, and 400 nm. Taking into account the present geometry, only a fraction $\approx 20\%$ of the incident light will illuminate the sample crystal (round shaped with radius $r = 0.5$ cm). With $E = \frac{hc}{\lambda} \times n_{\text{photon}}$ then the number of photons can be estimated to $\approx 10 \times 10^2 \text{ nm}^{-2}$, depending on the wave length used.

Local Bias Spectroscopy under Illumination

The bias spectroscopy measurement protocol used to investigate optically induced charge transfers is illustrated in Fig. A.2 (a). To rule out the charge transfer within a molecule on the surface, both spectra above the molecule (1) and above the surface (2) need to be recorded, and subtracted from each other. However, if the molecules are regarded on a metal surface, interface effects might become crucial [see Sec. 4.5], so that a simple subtraction is not valid anymore.

To be able to unambiguously attribute an observed SPV to an optical excitation, also the distance dependence of the LCPD [see Sec. 1.2.1], due to the long- and short- range electrostatic forces, needs to be taken into account. For this reason, for each spatial location and wave length several spectra are recorded at different tip-sample separations z within an interval

[†]The transmission reached 90% for wavelengths between $\lambda = 200 \text{ nm}$ to 1200 nm .

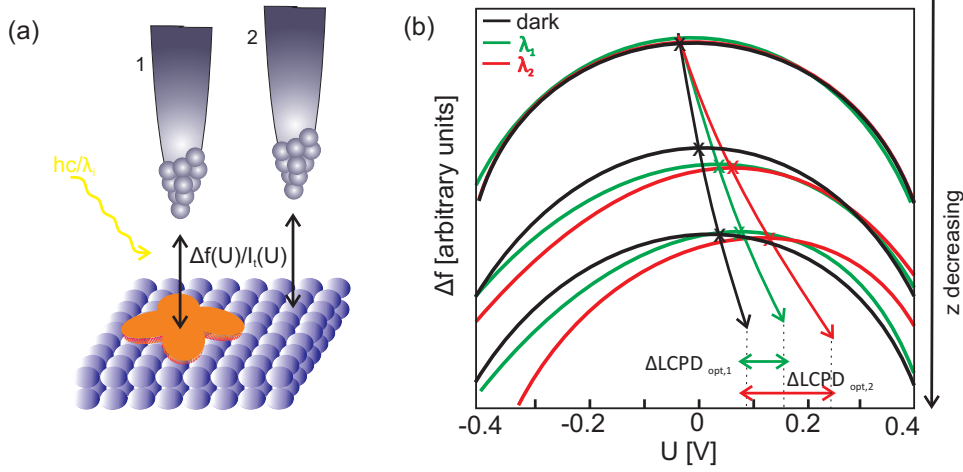


Figure A.2: Bias spectroscopy under illumination **(a)** Scheme of the procedure. 1D bias spectroscopy measurements are repeated at different tip-sample separations above the molecule and above the surface. **(b)** Illustration of the distance dependence of U_{LCPD} and the SPV, by plotting schematic $\Delta f(U)$ -curves at different heights above the molecule.

of $z = 0.5 \text{ nm}$ to 1 nm . With decreasing z the parabolas shift laterally and vertically which is schematically illustrated in Fig. A.2 (b). If optical excitations take place, $LCPD(z)$ will evolve differently for the recording in dark and under illumination with different wave lengths. For the present example, the spectra corresponding to an illumination with λ_1 (green), and λ_2 (red) shift towards the same direction, but more than if recording the curves in dark, while for large tip-sample distances, no light induced differences appear. Actually, the $U_{\text{CPD}}/U_{\text{LCPD}}$ under different illumination conditions must not necessarily shift in the same direction. If the bias is applied to the tip, a shift to a more negative LCPD corresponds to more negative charge. The best comparison of the various data at different wave lengths is obtained by plotting the LCPD as a function of the corresponding frequency shift, which is a measure for the tip-sample separation.

A last important issue concerns the fact, that the microscope temperature of 4.8 K starts to increase by 0.1 K to 0.2 K upon illumination in dependence of the utilized wave length. This causes considerable drift, which can be particularly problematic for the z direction. Anyhow, waiting for about 30-40 minutes between switching to a new wave length and recording the spectra, and by activating atom tracked tip-positioning between each two recorded curves, enables to rule out such drift related artifacts.

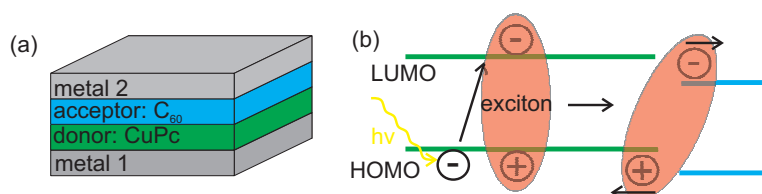


Figure A.3: Heterojunction organic solar cell (a) Scheme of the architecture of a heterojunction solar cell. (b) Corresponding energetic diagram, illustrating the generation of excitons, and their dissociation at the heterojunction.

Heterojunction Organic Solar Cells

Over the last decades, tremendous effort has been taken to develop organic solar cells mainly motivated by the perspectives of low cost large scale productions compared to the conventional inorganic cells [231, 304]. In an organic heterojunction solar cell [231], depicted in Fig. A.3 (a), two thin molecular layers are sandwiched between two metal electrodes, one being an electron donor, and the other an acceptor. A common combination is given by CuPc and C₆₀, which was also regarded here. Different geometries have been tested in order to fulfill several competing requirements for the optimization of the efficiencies. For instance, besides the bilayer cells like the one shown in Fig. A.3 (a), also bulk heterojunctions where the donor and acceptor layers become mixed, resulting in an increased D-A interface, were investigated [231].

Charge Carrier Generation and Separation

In Fig. A.3 (b) a scheme of the charge carrier generation and separation is illustrated by an energy diagram. The two molecular layers are represented by their HOMO and LUMO levels. Upon absorption of a photon within the optically active layer, an electron will be transferred from the HOMO to the LUMO (or even higher), generating a Frenkel type exciton (tightly bound) [206]. These excitons can then diffuse, whereas the diffusion lengths are typically only in the range of 0.4 nm to 15 nm [305]. At the heterojunction interface, an electrical field builds up similar to a pn-junction, which makes exciton dissociation energetically favorable if $IP_{\text{donor}} - EA_{\text{acceptor}} - U_{\text{Coulomb}} > 0$, resulting in a transition of the excited electron into the LUMO level of an acceptor molecule. Afterwards, the electrons and holes diffuse into opposite directions, which can be triggered by a concentration gradient and furthermore tuned by applying an external electric field.

Construction of a Two Molecule Solar Cell

The easiest configuration of a solar cell made by two molecules between two metal contacts accessible by SPM methods is to adsorb one of them on a

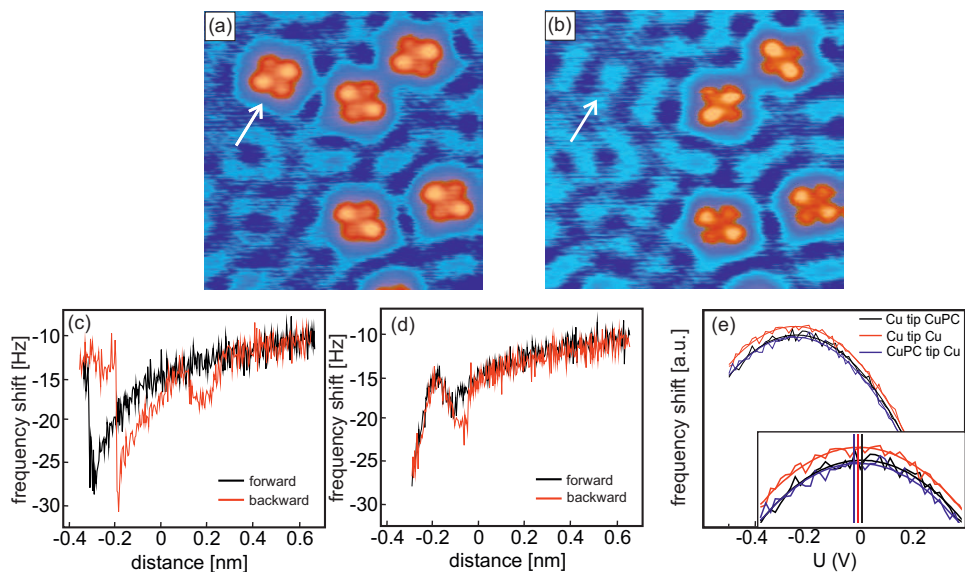


Figure A.4: Tip functionalization by CuPc. (a) STM constant current image before and (b) after picking up a CuPc molecule. The modified shape for the molecules in the upper right corner is related to a frustrated rotation, like discussed in Chap. 6. (c,d) Forward and backward scans of the corresponding $\Delta f(z)$ curves, before, and after picking up the molecule. The bias voltage was tuned to ≈ 0 V for these two curves. (e) $\Delta f(U)$ -curve with a Cu tip on Cu, a CuPC tip on Cu and a Cu tip on CuPc. **Parameters:** (a): $U_{\text{bias}} = -30$ mV, $I_t = 30$ pA, (b): $U_{\text{bias}} = -30$ mV, $I_t = 30$ pA.

metal surface, while the probing tip is functionalized with the other. Still, one has to keep in mind that measured U_{LCPD} shifts in this geometry can not directly be compared to macroscopic heterojunction cells. The fact, that charge transfer takes place at the metal-molecule interfaces will strongly contribute to the signals.

Observing, that CuPc molecules on Cu(111) easily jump towards the tip upon the recording of $\Delta f(z)$ curves, suggested to functionalize the tip with the latter. The process, illustrated in Fig. A.4, works as follows: After recording a reference STM image, like in Fig. A.4 (a), the tip is positioned above a certain CuPc molecule, usually above the molecular center, whereas it is as well possible to position it above one of the benzo-pyrrole rings. Subsequently, $\Delta f(z)/I_t(z)$ are recorded, while slowly approaching closer to the molecule for each curve. The functionalization is then indicated by a hysteresis loop in the backward scan, similar to the case of lifting atomic chains [20], which can be seen in Fig. A.4 (c). This is as well confirmed by recording an STM image above the same surface area in Fig. A.4 (b), where the molecule now is missing, and the contrast of the remaining molecules appears different. With the molecule on the tip, the general shape of $\Delta f(z)/I_t(z)$ -curves changes, and they always feature a double minimum, as can be seen in Fig. A.4 (d). The

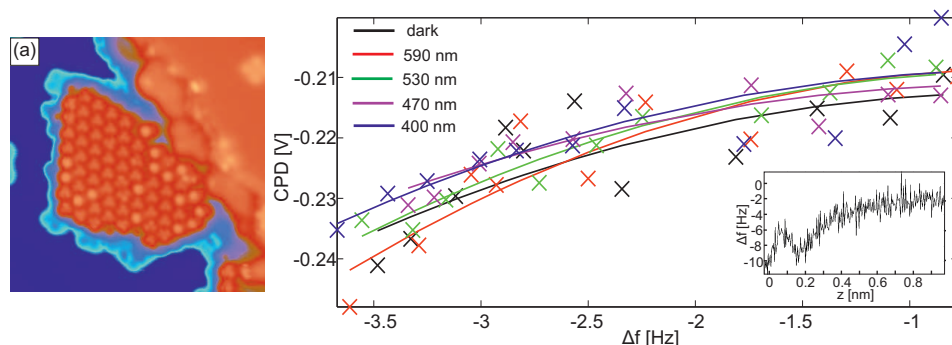


Figure A.5: Light assisted bias spectroscopy of a two molecule solar cell. (a) STM constant current of a small island of C₆₀ molecules on Cu(111). (b). 1D height dependent bias spectroscopy measurement. Shown is the extracted LCPD as a function of the frequency shift, which indicates the tip-sample distance. Inset: Corresponding $\Delta f(z)$ - curve, needed to connect the frequency shift towards the tip-sample distance. **Parameters:** (a): $U_{\text{bias}} = -1.0$ V, $I_t = 30$ pA.

reproducibility of this process is almost 100%, whereas the specific contrast of STM images with a functionalized tip remains individual, and strongly depends on how exactly the CuPc molecule attaches to the tip. The maximum tunneling current flowing during the picking up process accounts to ≈ 500 pA.

Besides the modified curvatures of the $\Delta f(z)/I_t(z)$ curves the tip functionalization also gives rise to a shift in the LCPD. For a further analysis of this shift, $\Delta f(U)/I(U)$ curves were recorded with a Cu tip on the bare Cu(111) surface, with a Cu tip above a CuPc molecule, and with a CuPc tip above the Cu(111) surface, which are exemplarily shown in Figs. A.4 (e), whereas the curves were adjusted in y-direction. As expected, compared to the LCPD measured with a Cu tip on the bare Cu(111) surface, the two other parabolas equally shift laterally in opposite directions which can be best seen in the inset.

Illumination of the Cell

C₆₀ on the Cu(111) surface is known to form two dimensional islands at submonolayer coverage with five possible orientations of the molecules, which start to grow from step edges [96, 157, 306], as shown in Fig. A.5 (a). The geometry adopted for the illumination experiment was given by tracking the previously CuPc functionalized tip above one C₆₀ molecule within the island during the entire measurement. In this manner, only spectra above the C₆₀ molecule have been recorded, without any references recorded with a CuPc- or Cu tip on Cu(111).

In total, ten $\Delta f(U)/I(U)$ - curves at different tip-sample distances have been recorded in dark, and for each of the four available wavelengths. The ex-

tracted LCPD plotted as a function of the corresponding frequency shift for each wavelength and for dark are shown in Fig. A.5 (b). The crosses refer to the raw data points, while the line is a polynomial $ax^2 + bx$ fit^{II}, in accordance to the quadratic dependence of the frequency shift on the bias voltage, and assuming the small amplitude approximation of the force gradient for the frequency shift.

With decreasing tip-sample distance, all curves shift to more negative LCPD. However, no clear light induced SPV could be detected. However, one might at least get the imagination that the different graphs start to split at closest recorded tip-sample distance, so that one might expect a U_{LCPD} shift at even closer distances. For the tunneling current channel, also no light induced photo current was detectable (not shown here).

Since the old tuning fork setup was used, the minimal tip-sample distance was limited to a tunneling current of ≈ 100 pA in order to minimize cross talk influences, as discussed in Sec. B. This is a major draw back for the SPV detection. The closest recorded tip-sample separation corresponding to -3.5 Hz is only dominated by long range interactions, which becomes apparent when looking at the $\Delta f(z)$ curve shown in the inset. By using the new tuning fork setup the tip could be positioned considerably closer towards the surface. On the other hand, even with the old tuning fork set-up LCPD shifts of CuPc on Cu(111) could be detected, so that the fact that the old setup was used can not hold as an explanation.

As evidenced from the LCPD maps shown in Fig. 6.4, the electrons are mainly found at the location of the benzo-pyrrole rings. For this reason, the exact attachment of the CuPc molecule at the tip might be crucial for the measurement, which remains an uncontrollable parameter. Thus, it might be advantageous to functionalize the tip with C_{60} instead, which features a much higher symmetry. Another advantage of a tip functionalization with the latter concerns, that the CuPc molecules already individually adsorb on the Cu(111) surface, so that a real two molecular solar cell could be constructed.

Additionally, the molecules might not become excited in this particular set-up. While it was proven that the obtained intensities of $\approx 10 \times 10^2 \text{ nm}^{-2}$ are sufficient to excite sub-surface nitrogen-vacancy centers of nano diamonds [301], they might not be high enough to excite single molecules anymore, because the small size of a single molecule is accompanied with reduced photon adsorption probabilities at a certain location within one single molecule. This probability can furthermore become reduced by the close proximity of the scanning tip, and probably the majority of photons is absorbed on the tip [275], or the molecule might experience local shadowing. One particularly important point concerns the geometry chosen for the two-molecule solar cell. The fact, that both molecules are adsorbed on a metal

^{II}Actually, a and b themselves are distance dependent, which is neglected here.

already leads to charge redistribution due to the organic-metal interfaces. For both molecules the charge transfer occurs from the metal to the molecule, so that the LUMOs become already partially occupied. Furthermore, the lifetimes of electrons in excited states for the CuPc on the metallic tip, and for the C₆₀ on the metal surface are very short, and decay on the same time scale. This generally affects the detection of excited states with difficulties, but could be drastically improved by depositing one of the molecules on a thin insulating film instead of directly putting it on the metal. In this manner, it still interacts with the metal electrode, as tunneling through the thin film is possible, but the life times of electrons in excited states increase by $\approx 10^3$. Furthermore, the influence of the surface on the molecule is drastically reduced on a thin film [see Sec. 3.3].

Outlook

By using the simplest possible geometry the goal of observing the intermolecular charge transfer between C₆₀ and CuPc could not yet be achieved in this experiment. However, several improvements have been suggested, that would highly increase the probability of observing such light induced CT. By functionalizing the tip with C₆₀ and positioning CuPc on a free terrace of NaCl(2ML)/Cu(111), for instance the geometry of the device will be notably improved. Secondly, one might think about using a light source with higher intensity, for instance a tunable laser, or even a light source incorporated into UHV. If the CuPc molecules are deposited on the thin film, it will be furthermore important to map the LCPD not only above the molecular center, but also above the lobes, as the lobes are the main location for the electrons as was evidenced by the charge distribution maps shown in the last chapter.

Appendix B

Dissipation with the old sensor

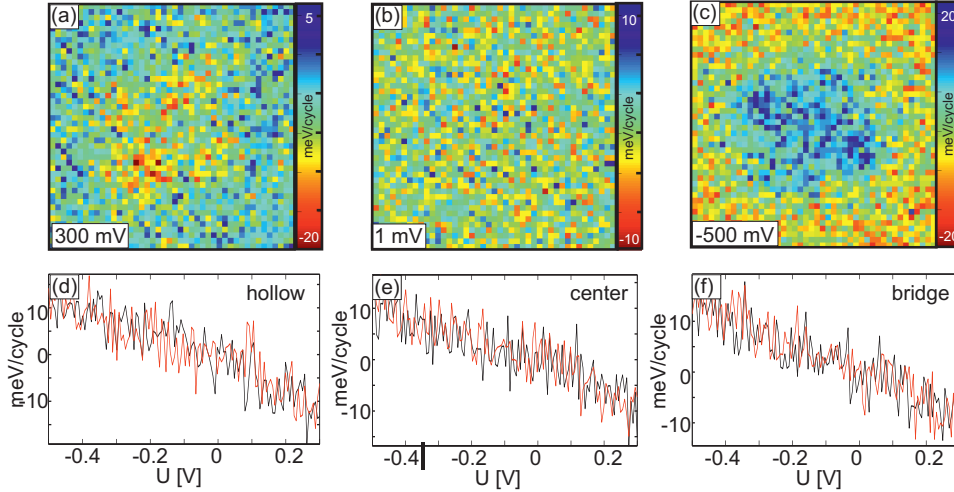


Figure B.1: Dissipation signal recorded for the bias spectroscopy data set of CuPc on Cu(111), discussed in Chap. 6. **(a-c)** Three excitation maps at -500 mV, 1 mV, and 300 mV. **(d-f)** 1D curves extracted above a benzo pyrrole ring above a hollow site, above a bridge site, and above the molecule's center. All three feature a linear dependence on the applied bias.

For the bias spectroscopy data of CuPc on Cu(111) presented in Chap. 6, it is mandatory to check the simultaneously recorded dissipation signal. While for the data recorded above CuPc on NaCl(2ML)/Cu(111), no dissipation was detected (not shown), the data recorded on the Cu(111) surface indeed features some non typical dissipation signal. This data set was still recorded with the tuning fork in the old setup, which likely can be influenced by cross talk related phenomena. In Fig. B.1(a-c) three images of the dissipated energy per oscillation cycle [see Sec. 1.2.4] for three applied bias voltages, -500 mV, 1 mV, and 300 mV, are shown. While at an applied bias voltage of 1 mV principally no contrast related to the morphology of

the molecule is observable in the excitation map, it becomes clearly visible for the other two images. Particularly, the image recorded at 300 mV features negative dissipation above the molecule. By extracting 1D excitation signal curves $E_{\text{diss}}(U)$ curves above three characteristic positions above the molecule, i. e. a benzo-pyrrole ring above a hollow site position, one above a bridge site, and the center, furthermore a linear dependence of the excitation on the applied bias becomes visible. These findings indicate that a slight cross talk was apparent during the recording of this data set. However, on the other hand, the influences do not seem to play a role within the frequency shift channel, and thus can be neglected for the discussion. This is supported by the fact that the signal remains below 20 mV, while the background dissipation features a statistic modulation of ± 10 mV, and secondly by the very good agreement of the LCPD maps with the supporting DFT calculations and that of the $I(U)$ contrasts with the theoretical and experimental observations in [201, 280].

Acknowledgments

Finally, I want to use the opportunity to thank a couple of people, without whom this thesis would not have been possible!

First of all my thanks go to Prof. Ernst Meyer for the opportunity to accomplish my thesis in his group! The possibility to attend various conferences and work shops strongly increased my scientific knowledge and broadened my horizon. With his deep knowledge, by always being open-minded to new ideas of his group members, and by giving them the space to develop their own ideas, he creates a very special and friendly atmosphere for scientific work!

Also, I want to thank my thesis supervisor Dr. Thilo Glatzel. With his long experience and expertise, he always took time for intense discussions, and suggested new ideas to proceed. Similarly, my thanks go to Dr. Shigeki Kawai, and Dr. Rémy Pawlak, who not only worked on the same machine, but intensely supported me during my whole work. I gained a lot by their skills which they never hesitated to share with me. I do not want to forget to thank Prof. Alexis Baratoff for numerous fruitful, and extremely helpful discussions. His thoroughgoing knowledge in the field is outstanding.

Of course, my thanks also go to all present and former group members, with whom I worked with, for the good and social working atmosphere! Apart from the colleagues, I have to mention all the staff members who are the ones making the scientific work at this university possible. There the great mechanical and electrical work shops, but also the secretary staff, and all others, who were always helpful whenever asked.

I want to thank Kasper Zimmermann for doing the ESI spectra, and the group of Prof. Rolf Möller in Duisburg who gave me the possibility to record QMS spectra, in particular Manfred Lange and Dennis van Vörden. Also, I want to thank Dr. Shi-Xia Liu and Prof. Silvio Decurtins for the TTF-dppz molecules and numerous intense discussions. Here, I also want to mention Dr. Thomas Jung, who contributed with several ideas. And of course my thanks go to Dr. Ali Sadeghi for performing the DFT calculations and providing me the images shown in Chap. 6.

Finally, my thanks go to my greatest supporter Sascha, who motivated, and encouraged me during my whole thesis, but also apart from that. Without him, it would have been much more difficult for me! Last but not least many

thanks also to my sister, and of course to my parents, who support me since I was born, and without whom I could not be at this point.

List of Figures

1.1	Scheme of a <i>qPlus</i> sensor	4
1.2	The tunneling current	5
1.3	Topographic and electronic effects in STM	6
1.4	Formalism after Bardeen and Tersoff-Hamann description	7
1.5	Interaction forces in AFM	10
1.6	Origin of the CPD	11
1.7	Resolution Considerations	14
1.8	Topographic operation with a tuning fork	20
1.9	Feedback operation with a tuning fork sensor	21
1.10	Spectroscopic operation with a tuning fork	23
1.11	Inelastic tunneling	25
1.12	Manipulation modes in SPM	28
2.1	Acquisition methods for 3D spectroscopy data sets	32
2.2	Drift and creep reduction and influence of the tip structure.	35
2.3	Frequency shift data recorded with the grid- and layer mode	37
2.4	Tip trajectories indicating the deformation	39
2.5	Force and potential energy extractions	40
2.6	1D curves of the grid-mode data	41
2.7	Influences of the oscillation amplitude.	42
3.1	UHV-LT-STM/AFM	46
3.2	<i>qPlus</i> force sensor	47
3.3	Utilized surfaces	48
3.4	Utilized surfaces	50
3.5	The sublimation testing unit	54
3.6	ESI spectra of TTF-dppz)(CN)	55
3.7	Sample morphology of TTF-dppz(CN) on Cu(111)	56
3.8	Ordered structures on Cu(111) after post- annealing	58
3.9	dppz	59
3.10	TTF-dppz on NaCl/Cu(111), and KBr(001)	60
4.1	Bond formation in molecules	66
4.2	Concepts for chemical bonding	67

4.3	Hückel theory and aromaticity	68
4.4	Bulk solid	70
4.5	Surface dipole	71
4.6	Physisorption vs. Chemisorption	74
4.7	Adsorption conformations	75
4.8	Interface dipole at the metal-molecule interface	78
4.9	Molecule on thin insulating films	80
5.1	Chemical structure and adsorption of H ₂ TBCPP	84
5.2	3D spectroscopy data cuboids	85
5.3	Lifting process of the cyanophenyl groups	86
5.4	Statistical analysis of the lifting process	87
5.5	Directed rotations of single porphyrins	89
5.6	Mechanism behind the directed rotation	90
6.1	Sample morphology after deposition of CuPc	94
6.2	Adsorption geometries on NaCl/Cu(111) and Cu(111)	96
6.3	Electronic orbital structure of CuPc	98
6.4	LCPD maps of CuPc on NaCl(2ML)/Cu(111) and Cu(111).	100
6.5	Comparison of the LCPD with DFT calculations	101
6.6	Simultaneously acquired I(U) data	104
6.7	Hysteresis and telegraph noise for CuPc on Cu(111)	105
6.8	Frustrated rotation of CuPc on Cu(111)	105
6.9	Switching probability of CuPc on Cu(111)	106
A.1	Optical spectras: scheme, CuPc, C ₆₀	139
A.2	Bias spectroscopy procedure under illumination	141
A.3	Working principle of heterojunction organic solar cells	142
A.4	Construction of a two molecule solar cell	143
A.5	Two molecule solar cell and its illumination	144
B.1	Dissipation for CuPc on Cu(111)	147

List of abbreviations and Variables

SPM	scanning probe microscopy
STM	scanning tunneling microscopy
AFM	atomic force microscopy
nc-AFM	non contact AFM
TF	tuning fork
U_{bias}	applied bias voltage
I_t	tunneling current
3D	three dimensional
DOS	density of states
LDOS	local density of states
vdW	van der Waals
F_{el}	electrostatic force
F_{vdW}	van der Waals force
F_{chem}	chemical interactions
F_{rep}	repulsive interactions
lr	long range
sr	short range
CPD	contact potential difference
E_F	fermi energy
Φ	work function
FM	frequency modulation
Δf	frequency shift
A_{osc}	oscillation amplitude
ϕ	phase

E_{diss}	dissipation energy
PLL	phase locked loop
WKB	semiclassical approximation named after G. Wentzel, H. A. Kramers and L. Brillouin
STS	scanning tunneling spectroscopy
DFS	dynamic force spectroscopy
nc-AFM	non-contact AFM
IET	inelastic tunneling
F_{ts}	tip-sample interaction force
F_{lat}	lateral force
LT	low temperature
UHV	ultra high vacuum
QMB	quartz crystal micro balance
QMS	quadrupole mass spectrometer
KBr	potassium bromide
NaCl	sodium chloride
CN	carbonitrile group
CT	charge transfer
MO	molecular orbital
Pc	phtalocyanine
CuPc	copper phtalocyanine
TTF-dppz	tetrathiavulvalene fused dipyridophenazine complex
LCPD	local contact potential difference
MO	molecular orbital
LCAO	linear combination of molecular orbitals
HOMO	highest occupied molecular orbital
LUMO	highest unoccupied molecular orbital
EA	electron affinity
IP	ionization potential
DBTJ	double barrier tunneling junction
IET	inelastic tunneling
DFT	density functional theory
VL	vacuum level
SPV	surface photovoltage

List of Publications and Presentations

Peer-reviewed Journal Publications

- **S. Fremy**, A. Schwarz, K. Lämmle, M. Prosenc and R. Wiesendanger. The monomer-to-dimer-transition and bimodal growth of Co-Salen on NaCl(001): a high resolution atomic force microscopy study, *Nanotechnology*, 20:405608, 2009.
- R. Pawlak, S. Kawai, **S. Fremy**, T. Glatzel and E. Meyer. Atomic-scale mechanical properties of orientated C60 molecules revealed by noncontact atomic force microscopy, *ACS Nano*, 5(8):6349-6354, 2011.
- R. Pawlak, **S. Fremy**, S. Kawai, T. Glatzel, H. Fang, L.-A. Fendt, F. Diederich, and E. Meyer. Directed rotations of single porphyrin molecules controlled by localized force spectroscopy, *ACS Nano*, 6:6318-6324, 2012.
- R. Pawlak, S. Kawai, **S. Fremy**, T. Glatzel and E. Meyer. High-resolution imaging of C60 molecules using tuning-fork-based non-contact atomic force microscopy, *J. Phys.: Cond. Matter*, 24:084005, 2012.
- **S. Fremy**, S. Kawai, R. Pawlak, Th. Glatzel, A. Baratoff and E. Meyer. Three-dimensional dynamic force spectroscopy measurements on KBr(001): atomic deformations at small tip-sample separations, *Nanotechnology*, 23:055401, 2012.
- **S. Fremy** et al. On the chemical stability of a donor-acceptor molecule: influence of substrates and deposition conditions, in preparation.
- **S. Fremy** et al. Substrate induced changes in the charge distribution and electrostatic potential of a single adsorbed molecule, in preparation.

- **S. Fremy** et al. Switching the adsorption geometry of single molecules, in preparation.

Oral Presentations

- B. Such, **S. Fremy**, S. Kawai et al., 3D force spectroscopy on KBr(001) by tuning fork based nc-AFM at low temperatures, DPG Frühjahrstagung 2010, 23/03/2010, Regensburg, Germany.
- **S. Fremy**, S. Kawai, R. Pawlak et al., 3D dynamic force spectroscopy on KBr(001) at low temperature with a tuning fork sensor, 13. International Conference on Non-Contact Atomic Force Microscopy, 03/08/2010, Kanazawa, Japan.
- **S. Fremy**, S. Kawai, R. Pawlak et al., 3D dynamic force spectroscopy on KBr(001) at low temperature with a tuning fork sensor, Seeing at the nanoscale VIII, 01/09/2010, Basel, Switzerland.
- **S. Fremy**, S. Kawai, R. Pawlak et al., 3D dynamic force spectroscopy on KBr(001) at low temperature with a tuning fork sensor, Invited Talk, 16/05/2011, Duisburg, Deutschland.
- **S. Fremy**, R. Pawlak, S. Kawai, et al., Investigating the Self Assembly of TTF-dppz with a tuning fork sensor at low temperature, DPG Frühjahrstagung 2012, 29/03/2012, Berlin, Germany.

Poster Presentations

- **S. Fremy**, S. Kawai, R. Pawlak et al., 3D dynamic force spectroscopy on KBr(001) at low temperature using a tuning fork sensor, 2nd International Workshop on Advances Atomic Force Microscopy Techniques, 28/02/2011, Karlsruhe, Germany.
- **S. Fremy**, R. Pawlak, S. Kawai et al., Investigating the Self Assembly of TTF-dppz with a tuning fork sensor at low temperature, Workshop on Molecular Electronics: From Organic Electronics to Single Molecules, 24/06/2011, Villigen, Switzerland.
- **S. Fremy**, R. Pawlak, S. Kawai et al., Investigating the Self Assembly of TTF-dppz with a tuning fork sensor at low temperature, Workshop on Molecular Electronics: From Organic Electronics to Single Molecules, 24/06/2011, Villigen, Switzerland.
- **S. Fremy**, R. Pawlak, S. Kawai et al., Investigating the Self Assembly of TTF-dppz with a tuning fork sensor at low temperature, 13. International Conference on Non-Contact Atomic Force Microscopy, 29/09/2011, Lindau, Germany.

LIST OF FIGURES

- **S. Fremy**, R. Pawlak, S. Kawai et al., Charge distribution and Scanning Tunneling Spectroscopy of CuPC analyzed by tuning-fork AFM/STM, Ecole Physique des HOUCHEs, Workshop-winter schoop artist: Adressing, Transport, and Storage of information by single atoms and molecules, 15/01/2013, Les Houches, France.
- **S. Fremy**, R. Pawlak, S. Kawai et al., Charge distribution and Scanning Tunneling Spectroscopy of CuPC analyzed by tuning-fork AFM/STM, Swiss Nanoconvention, 23/05/2013, Basel, Switzerland.

Curriculum Vitae

27. 01 1985	Born in Wittmund (Germany).
1991-1995	Primary school in Hamburg (Germany).
1995-2003	Secondary school, Albert-Schweitzer-Gymnasium in Hamburg, Germany.
2003-2009	Diploma Studies at the University of Hamburg. Diploma thesis in the group of Prof. Wiesendanger. Rasterkraftmikroskopie an Co-Salen Minor subjects: astronomy, mathematics, bio-physics, philosophy.
2009-2013	Ph.D. thesis in Physics, University of Basel in Basel. Group of Prof. Dr. Ernst Meyer Examination committee: Dr. Thilo Glatzel (thesis advisor) Prof. Dr. Martino Poggio (co-referee) Prof. Dr. Ernst Meyer (faculty representative) Dr. Bartosz Such (expert)